DEPARTMENT OF MECHANICAL
AND INDUSTRIAL ENGINEERING

CARLOS ALEXANDRE BANDARRINHA MONTEIRO
Bachelor of Science in Mechanical Engineering

NUMERICAL STUDY OF A DRAG REDUCTION SYSTEM FOR A FORMULA STUDENT CAR

INTEGRATED MASTERS DISSERTATION

MECHANICAL ENGINEERING

NOVA University Lisbon
November, 2021

DEPARTMENT OF MECHANICAL
AND INDUSTRIAL ENGINEERING

NUMERICAL STUDY OF A DRAG REDUCTION SYSTEM FOR A FORMULA STUDENT CAR

INTEGRATED MASTERS DISSERTATION

CARLOS ALEXANDRE BANDARRINHA MONTEIRO
Bachelor of Science in Mechanical Engineering

Adviser: Diana Filipa da Conceição Vieira
Invited Assistant Professor, NOVA University Lisbon
Co-adviser: Moisés Gonçalves de Brito
Invited Assistant Professor, NOVA University Lisbon

MECHANICAL ENGINEERING

NOVA University Lisbon
November, 2021

Numerical Study of a Drag Reduction System for a Formula Student Car

ACKNOWLEDGEMENTS

In the very first place I want to leave a very special thanks to my mother for believing in me and supporting me in all kinds of ways at all times. My father, my stepfather and the rest of my family that directly or indirectly helped me to make this come true. My close friends which always reminded me that a little fun is more fruitful than one might think.

My thesis coordinators that believed in my high expectations and supported me all the way through, showing availability at all cost! All of the university staff which allow this to be experienced by every student that dares to cross this path.

A very warm thanks to my FSTLisboa teammates that welcomed me so well and with whom I've had the unexpected opportunity to work with, learn a lot and push myself into believing in higher achievements.

My Continental Engineering Services colleagues who have welcomed me in June in their team and that had the necessary flexibility, understanding and support through the hardest times of my dissertation development.

My dog, Laika, for the wonderful walks to get my head a little off work!

In some sort of way I actually want to thank the global pandemic, for forcing me to have some time to myself and really think it through. It helped me to find the path that I want to take.

ABSTRACT

This dissertation focuses on utilising computational fluid dynamics tools to achieve an optimized Drag Reduction System configuration from an existent design of a Formula Student car rear wing. The considered rear wing is a multi-element wing with 3 airfoils that produces a considerable fraction of the car's total aerodynamic downforce. This requires a downforce/drag forces trade-off that impacts the performance of the car in each segment of the race track. The introduction of a Drag Reduction System requires that the system is well design to avoid adding complexity without considerable benefits. A typical formula student DRS concept is applied where the two most rear-er flaps are rotated in order to decrease or increase drag. Achieving a good DRS system through the best possible configuration in terms of angle of attack of the flaps, as well as the center of rotation position was considered to have the potential to be a considerable improvement to the cars' performance. In the present work *StarCCM+* is used to simulate the external aerodynamics of the isolated rear wing. Simulation macros are developed in order get a better understanding of the overall force mapping of all lift and drag forces on the current rear wing configuration. Through a first force mapping study is in seen how the second flap's angle of attack has more influence in the overall forces on the wing. The lift and drag mapping showed the expected close proximity between this separate force components. Iteratively, the best configuration in terms of angles and centers of rotation of the flap is achieved. Through a 2D analysis of the isolated airfoil it is seen that the lowest drag angle of attack is about 0. On a first iteration of optimization process the first movable flap sits at 0 while for the second flap shows that a −6 angle of attack is preferable in order to reduce drag. It is seen that varying the centers of rotation also has impact the force values although it is less than varying the angles of attack. The combination of the angles of attack study with the center of rotation showed that the preferable minimum drag configuration sits at a $\alpha_{flap1} = 0$, a $\alpha_{flap2} = -6$, a $COR_{flap1} = 20\%$ and a $COR_{flap2} = 0\%$. The tools developed through this dissertation are left to the team in such a way that it makes it faster to achieve the iterative study of the DRS system configuration.

Keywords: CFD, Rear Wing, Formula Student, Drag Reduction System, DRS, Aerodynamics, Turbulence.

RESUMO

Esta dissertação concentra-se na utilização de ferramentas computacionais de dinâmica de fluidos para obter uma configuração otimizada do Sistema de Redução de Arrasto para a asa traseira de um carro de *Formula Student*. A asa em questão é uma asa multi-elemento com 3 aerofólios que produz frações consideráveis das forças aerodinâmicas descendente e de arrasto totais do carro. Isso requer um compromisso entre as forças descendente e de arrasto que afeta o desempenho do carro em cada segmento da pista de corrida. A introdução de um sistema de redução de arrasto requer que o sistema seja bem projetado para evitar que se adicione complexidade ao carro sem um acréscimo de benefícios que o justifiquem. Um conceito típico de DRS de *Formula Student* é aplicado onde os dois flaps mais traseiros são girados a fim de diminuir ou aumentar o arrasto. Conseguir um bom sistema DRS através da melhor configuração possível em termos de ângulo de ataque dos flaps, bem como da posição do centro de rotação foi considerado como tendo potencial para ser uma melhoria considerável no desempenho dos carros. No presente trabalho, a ferramenta textit StarCCM + é usado para simular numericamente a aerodinâmica externa da asa traseira do carro *FST 10e* da equipa *FSTLisboa*. Macros de simulação são desenvolvidos para facilitar a obtenção do mapeamento geral das forças e sustentação e arrasto na configuração atual da asa traseira. Por meio de um primeiro estudo de mapeamento de força, é possível ver como o ângulo de ataque do segundo flap é mais impactante nas forças gerais na asa. O mapeamento de sustentação e arrasto mostrou também a proximidade esperada entre estes dois componentes de força aerodinâmica. Iterativamente, chegou-se à melhor configuração em termos de ângulos e centros de rotação. Por meio de uma análise 2D do aerofólio isolado, verifica-se que o menor ângulo de arrasto de ataque é cerca de 0. Em uma primeira iteração do processo de otimização, o primeiro flap móvel fica em 0 enquanto que o segundo flap mostra que um ângulo de ataque de -6 é preferível para reduzir o arrasto. A diferença de ângulo ótimo do segundo flap entende-se como sendo relacionada com a existência de um *gurney flap* e à interação entre os vários flaps. Vê-se que variar os centros de rotação também tem impacto nos valores de força, embora seja menor do que variar os ângulos de ataque. A combinação dos ângulos de estudo de ataque com o centro de rotação mostrou que a configuração de arrasto mínimo preferível fica em $\alpha_{flap1} = 0$, a $\alpha_{flap2} = -6$, a $COR_{flap1} = 20\%$ e um $COR_{flap2} = 0\%$. As ferramentas desenvolvidas nesta dissertação são deixadas para a equipa de forma a agilizar o estudo iterativo da configuração do sistema DRS.

Palavras-chave: CFD, Rear Wing, Formula Student, Sistema de Redução de Arrasto, DRS, Aerodinâmica, Turbulência.

Contents

Appendices

Annexes

List of Figures

List of Tables

ACRONYMS

AR	Aspect Ratio 27
CFD	Computational Fluid Dynamics 8
DRS	Drag Reduction System 1, 8, 9, 30
PDE	Partial Differential Equations 47

Symbols

$2D$	Two-dimensional 12, 46
$3D$	Three-dimensional 49
α_{flap1}	First flap angle of attack vi, ix, xvi, xvii, 72, 73, 76, 81, 82, 84, 86
α_{flap2}	Second flap angle of attack vi, ix, xvi, xvii, 72, 73, 76, 81, 82, 84, 86
α	Angle of attack 13
c_{Flap1}	Chord of the rear wing's first flap 56
c_{Flap2}	Chord of the rear wing's second flap 56
C_D	Drag coefficient 15
CG	Center of gravity 4
C_L	Downforce coefficient 15
COR_{flap1}	Center of rotation of flap 1 vi, ix
COR_{flap2}	Center of rotation of flap 2 vi, ix
D	Drag 12
δ	Boundary layer thickness 16
L	Downforce 13
Re	Reynolds number 11, 16, 18, 21, 50, 52

1

INTRODUCTION

On this chapter a brief introduction to motorsport aerodynamics and to the Formula Student Competition is done so that it is possible to better understand the scope of this thesis. This chapter reflects the motivation behind the work, the overall goals as well as the thesis outline.

The following dissertation will engage on the numerical study of the aerodynamic behaviour of a drag reduction system, or Drag Reduction System (DRS), for a Formula Student car. Furthermore, in an academic sense, the principles and techniques behind Computational Fluid Dynamics are explored and applied to the current project. The case study involves the 2020 electric race car developed by the FST Lisboa Team, the FST10e, seen in figure 1.1. A CFD analysis is done around its rear wing and an iterative study is done around the possible DRS configurations as a way to optimize its different aspects before moving into the mechanical design of the system.

Figure 1.1: FST10e at the Estoril circuit.

1.1 Brief Historic Introduction to Vehicle Aerodynamics

Motorsport, like other sports, requires physical fitness, concentration, preparation and training but is also where the progress in technology may play the biggest role in dominating the race [1]. Taking advantage of the properties of the air flow around a race car is one of the most promising fields where investing in engineering investigations may bring considerable improvements in the race car performance.

The concept of external aerodynamics was firstly introduced mainly as an attempt to reduced the air resistive forces, also know as drag. The previous type of aerodynamics awareness was practically introduced in parallel with the initial growth of the automotive industry. Only around the beginning of the 1970s were we able to start understanding the greater potential of the interaction between aerodynamic forces and vehicle performance and handling. Around this time, Frank Winchell and his Chevrolet/Chaparral associates started to explore the benefits of adding additional downforce to the car without a relevant increase of the total car weight through aerodynamic downforce [2]. In a few years Chevrolet/ Chaparral and Lotus pioneered two concepts that revolutionized downforce generating race cars. The first was by adding "inverted"wings. After a few positioning trials in cars, such as the Chaparral 2E in figure 1.2, quickly converged into the more known positioning of one higher mounted rear wing and the two or single front-mounted wings, as seen in the Lotus 72D figure 1.3.

Figure 1.2: Chaparral 2E were a high mounted rear wing was firstly experimented before being introduced into F1.

Figure 1.3: Latest version of the Lotus 49B after a few rear wing mounting adjustments due to safety reasons.

A few years later, the ground-effect and vacuum-traction was introduced as the second far-reaching discovery in downforce generation. Also Chaparral and Lotus pioneered the introduction of creating suction between the car under-body and the ground. Commonly this is exploited by getting the car's floor as close to the ground as possible and by "sealing"the laterals of the floor with the so called "skirts". This approach is the reason behind the concept of some of the most iconic race cars such as the Chaparral 2J, in figure 1.4, and the Formula 1 cars' Lotus 78 and Brabham BT46 in figures 1.5 and 1.6 respectively.

1.2 Aerodynamics' Impact on Vehicle Performance

One of the main goals of introducing aerodynamics into a car's design in to produce down-force as well as reducing drag forces. Well designed aerodynamic devices have brought massive performance improvements in motorsport vehicles.

Figure 1.4: Chaparral 2J, the *Sucker car*, with fan mounted at the back to create suction underneath the underfloor by accelerating the airflow.

Figure 1.5: Lotus 78, the *ground effect* car that took advantage of side skirts to seal the floor and produce extra suction through the *Venturi* effect as will be explained in the chapter 2.

Figure 1.6: Brabham BT46, the *Fan Car*.

Increasing the aerodynamic load on the car also introduces drag which opposes the straight line acceleration capability. Ignoring the rolling resistance, the equivalent force that the car needs to overcome to drive itself forward is the aerodynamic drag force. This force can be presented in a simplified vehicle dynamics approach as in equation 1.1. ρ is the air density, C_D is the overall drag coefficient and A the frontal area,

$$D = \frac{1}{2}\rho C_D A\dot{x}^2 \tag{1.1}$$

Racing car performance is deeply affected by the dynamic behavior hence, vehicle dynamics improvement is crucial. Open-wheel racing car dynamics, such as the formula student's, are dependent on the effectiveness and efficiency of its aerodynamics [3].

In a straight line, considering that F is the equivalent force driving the car forward, the acceleration can be described as in expression 1.2.

$$m\ddot{x} = F - \frac{1}{2}\rho C_D A\dot{x}^2 \tag{1.2}$$

To achieve the quickest path when cornering, the driver tries to use the smallest radius of curvature possible at maximum speed representing the quickest path. The tire grip takes the most important role when improving the cornering performance. Tire grip is directly related to the car load multiplied by the friction coefficient ($F_z = N\mu$) which equals all the forces that the car produces on the road including aerodynamic downforce. Increasing the car's mass to achieve more load is not a viable way of improving corner ability because it reduces the car's acceleration capability due to inertial forces. Introducing aerodynamic load outcomes in more cornering capabilty due to the extra grip without adding weight to the car, working as "weightless"load. Figure 1.7 shows how aerodynamics have increased through out the time after being introduced in 1970 [4].

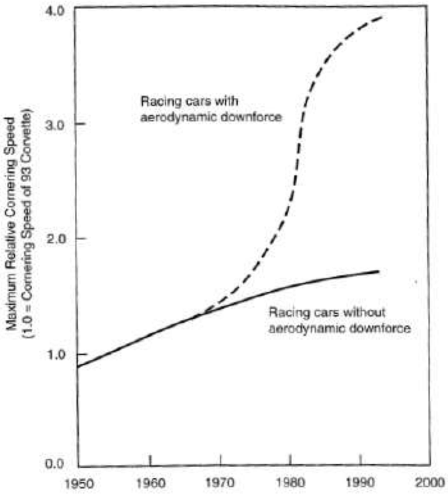

Figure 1.7: Evolution of lateral acceleration ability with and withou aerodynamics

The equilibrium when cornering can be described as in equation 1.3.

$$\mu F_z = \mu\left(mg + \frac{1}{2}\rho C_L A v^2\right) = \frac{mv^2}{R} \tag{1.3}$$

1.3 Load Distribution

Well distributing the forces through out the car aerodynamic components is of extreme importance and will also influence the way the aerodynamic components are thought and designed. Easier car handling usually comes from getting the aerodynamic load center closer to the *CG* [5].

This means that for a certain rear wings' downforce the goal may not to obtain the maximum downforce if it unbalances the rest of car. This defines one of the main goals of the present dissertation, the mapping of the aerodynamic forces throughout the several rear wing configuration so that this can be used as input for the vehicle dynamics department to ensure the best aerodynamic balance at all times. This also gives a hint of how an actively controlled wing during the race could be beneficial. The static aerodynamic balance can then be developed in equations 1.4 and 1.5 upon the definition of the free body diagram of the formula student car, figure 1.8 assuming that the side elements and undertray produce downforce close to the *CG* [5].

$$\uparrow: \quad \sum_i \mathbf{e}_z \cdot \mathbf{F}^{(i)} = 0 \quad \Rightarrow \quad N_f + N_r - mg - L_f - L_r = 0 \tag{1.4}$$

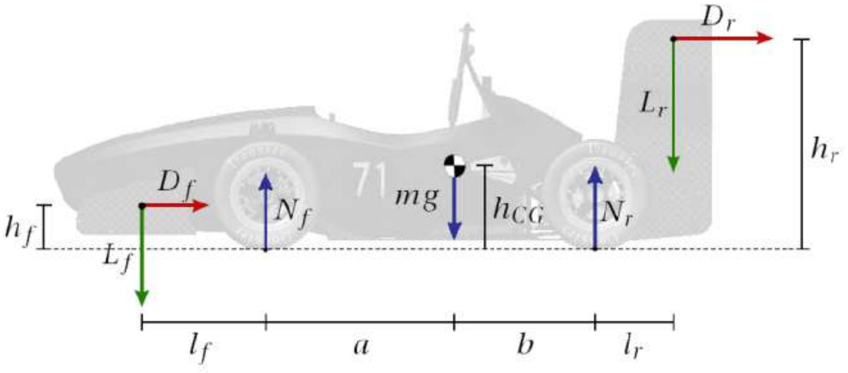

Figure 1.8: Free body diagram of the frontwing and rear wing forces acting on a formula student car

$$\curvearrowleft: \quad \sum_i \left(\mathbf{r}^{(i)} - \mathbf{r}_{CG}\right) \times \mathbf{F}^{(i)} = \mathbf{0} \quad \Rightarrow \quad \begin{aligned} & bN_r - aN_f - (l_r + b) L_r + \left(l_f + a\right) L_f \\ & + (h_{CG} - h_r) D_r + \left(h_{CG} - h_f\right) D_f = 0 \end{aligned} \tag{1.5}$$

1.4 Formula Student Competition Overview

Formula Student achieves the title of one of the most challenging engineering competitions between students where students build a internal combustion engine, an electric or an driverless race car from scratch to compete in several international events with other universities' teams. In the competition, after a set of scrutineering tests there are a set of static and dynamic events where the teams need to pass and excel in order to achieve the highest number of points. The sum of the points will determine the standings. This work will focus on the dynamic events and how it can improve the car's performance by utilizing a Drag Reduction System. The scrutineering and the static test are followed by the dynamic tests. At first there is the Acceleration event, followed by Skidpad and Autocross and then the main race, the Endurance event, that counts up to 325 points overall.

Concerning a formula student competition, velocities reached are not particularly high. The maximum velocity is often bellow 110 km/h which is usually not reached due to the fact that most of the dynamic part of the competition is spent on tight corners, with the exception of the acceleration event.

1.4.1 Dynamic Events

Table 1.1 presents a brief description of the dynamic events for the electric category.

As the scope of this work is to optimize the drag reduction, several events' performances can be enhanced such as the straight line speed in the acceleration, autocross and endurance as well as the fuel economy/ battery consumption in the endurance event.

Table 1.1: Description of the Formula Student Dynamic Events regulated by the *FSG*'s regulations book [6].

Event	Description	Maximum achievable points
Skidpad	Fastest lap time in a 8 figure circuit.	75
Acceleration	Fastest time over a 75m straight.	75
Autocross	Fast lap time over a 1km long circuit with straights, curves and chicanes.	100
Endurance	22 kilometers long track where acceleration, speed, handling, dynamics, fuel economy and reliability are evaluated	325

1.4.2 Formula Student Aerodynamics

Figure 1.9 shows the FST10e car simplified CAD for aerodynamics numerical simulation. The picture highlights the main groups of aerodynamic components that are usually present in the nowadays formula student race cars. These components are usually a front and rear wings, side elements which may include flaps, diffusers and other sub-components, an undertray usually as close to the ground as possible with increasing height up to the rear diffuser. All components are design by students with the goal of having the downforce-drag relation that best suits with car.

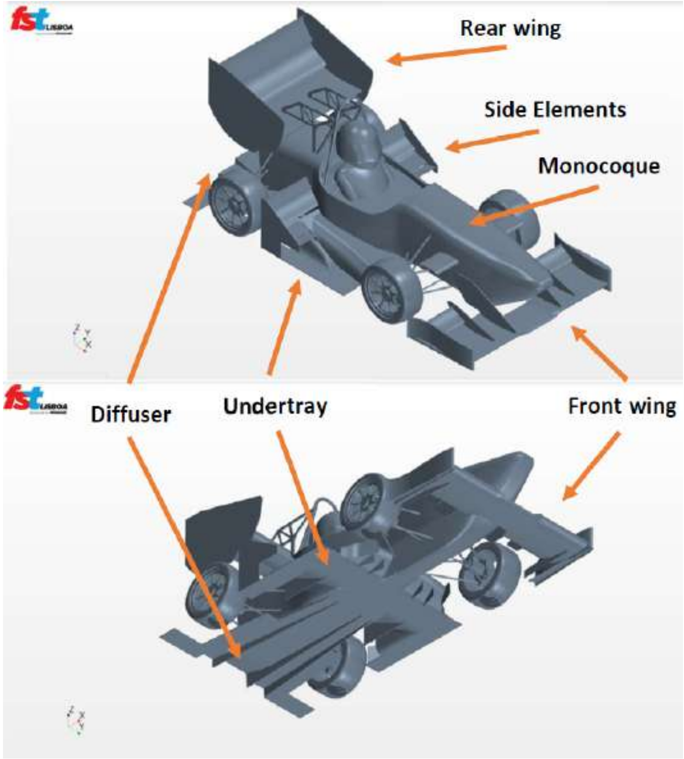

Figure 1.9: FST10e Aerodynamics Appendixes

A race car wing such as a rear wing is an inverted high-downforce wing who's geometrical properties suit the conditions that it will be expose to. Typically it presents a low aspect-ratio, high camber, multi-elements such as flaps and many other properties that correspond to its narrow operation range conditions, when compared with airplane wings. An ideal wing shape is never achieved due to the usual regulations attributed to each competition.

1.4.3 Aerodynamic Regulations

In nowadays' Formula student regulations, aerodynamic devices are restricted to the design boxes presented in figure 1.10. [6].

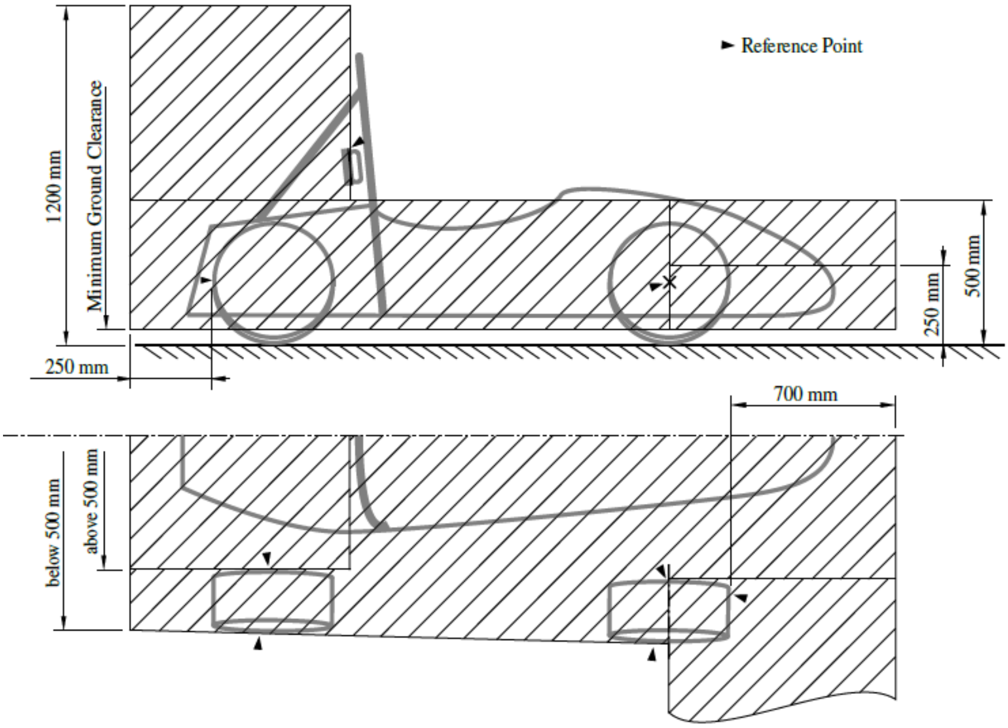

Figure 1.10: Maximum dimensions of the aerodynamic package taken from the *Formula Student Germany* Rules for the 2020 competition. [6]

In spite of the limitations imposed by the regulations, some other aspects need to be accounted for. In the case of the rear wing these are mainly the interaction between a wing and rest of the car components and the impact of the wing's low aspect-ratio in its pressure distribution. In race car engineering, ground-effect due to ground proximity has a large relevance as it increases significantly the downforce generated by a wing. However it is much more critical in the case of a front-mounted wing which can be as high as a tenth of its chord. When it comes to the rear wing working under the car's wake and with even smaller aspect ratio, these are the essential subjects of investigation.

1.5 Research Aim

Computational Fluid Dynamics (CFD) studies have been done around the FST10e rear wing from which it was predicted to produce almost 40% of the car's total drag forces. Teams make an effort to increase the downforce component by increasing the angles of attack in the case of wings. The gains in the downforce come as trade-off, as it also increases the drag component of the aerodynamic forces created. Due to the usual formula student speeds the drag component is some times neglected because during most of the highest scoring dynamic events the car is mainly under really tight cornering, where the drag component unfavourable to acceleration is not as important as sticking the car to the ground with downforce.

Nevertheless, when trying to reach a top spot in the overall results, every aspect counts, and a matter of tenth of seconds can make the difference in moving any team up or down the leader board. Certainly, a well designed Drag Reduction System has an overall positive impact by improving dynamic events' times as an enhancement of the vehicle dynamics through active aerodynamics. The main goals of the dissertation will be to quantify the aerodynamic improvements and advantages of the DRS using computational fluid dynamics' tools. Drag reduction through an introduction of a DRS will be analysed, as well as its trade-off with the downforce generated. Different configurations that enhance the drag reduction are explored. It will also engage in an academical investigation of how the flow behaves around a race car rear wing, the FST10e in particular, and how it interacts with the Drag Reduction System configurations.

1.6 Dissertation Outline

The thesis broken into 6 chapters as follows:

Chapter 1, as an introduction, includes historic background on vehicle aero dynamics, an overview on vehicle aerodynamics performance, its influence in the overall vehicle dynamics and usual devices used for this matter. The Formula Student competition is briefly described, detailing the different events and regulations of the competition.

In chapter 2 a fundamental approach of aerodynamics is done. Aerodynamic theory is correlated with the lift and drag phenomena. Turbulence and viscosity effects are introduced. The aerodynamic appendixes of a formula student car are also introduced having a closer look at the rear wing. There it is possible to correlate how the aerodynamic phenomena introduced previously affects the wing design.

Chapter 3 starts detailing the numerical methods used in order to simulate external aerodynamics aerodynamics. Turbulence modelling is detailed focusing on the $\kappa - \omega$ SST model as it ends up being the one used. Transition modelling is explained and correlated with the turbulence models and finally a brief introduction to the finite volume method and mesh discretization as well as the numerical error estimation.

Chapter 4 includes preliminary tests around a 2 dimensional airfoil where turbulence models and transition models are analysed. Afterwards a mesh analysis is done proceeding to the application of the mesh parameters on a experimental case in order to evaluate its proximity with real experimentla results. After these analysis a preliminary study of the FST 10e rear wing baseline configuration is done.

Chapter 5 Starts by describing the purposes of developing simulation macros for the optimization studies. Force mapping analysis are done varying the angles and centers of rotation of both flaps. Results discussion is included in this chapter.

Finally, chapter 6 presents suggestions of further work on aerodynamics and other engineering fields within the team in order to take the DRS design into more developed stages. The final remarks and sum-up of the study conclusions are also made on this chapter.

2

AERODYNAMICS

The application of developed CFD and turbulence modelling, as one of the main goals of this thesis, requires an initial explanation of the mathematical principles behind them. The Siemens StarCCM+ software is used along the thesis for all the simulations but a deeper explanation of everything behind the code is done in this chapter to better analyse the results and make the results more comprehensible in the following chapters. The computational resources were landed to the author by the FSTLisboa Team and Nova's School of Science's Mechanical and Industrial Engineering department.

The mathematical formulation of any aerodynamics related problem is greatly dependent on the Reynolds number Re, which represents the ratio between inertial and viscous forces in a specific flow as described in equation 2.1. This non-dimensional coefficient is often used as a replacement of flow velocity analyses because it grants a wider comparability.

$$Re = \frac{\rho V L}{\mu} = \frac{V L}{\nu} \tag{2.1}$$

For the specific type of car velocities that are inherent to the formula student competition, it is possible to consider a velocity of $V = 15\ ms^{-1}$ applying it to the air flow. The chord length of the FST10e rear wing is considered as $L = 0.4 + 0.2 + 0.2 = 0.8\ m$. A dynamic viscosity of $\mu = 1.511 \times 10^{-5} kg/m \cdot s$ and a air density of $\rho = 1.225\ kg/m^3$ were used. For this type of flow it is achieved a Reynolds number of the order of 10^5. With this order of Reynolds numbers a **turbulent** flow will develop with moderate dependence on the Reynolds number [7]. Also, within the external aerodynamics cases, many authors focus on the range between $10^5 < Re < 10^6$ as the low Reynolds number as mentioned in [8] where *J. Winslow* explains how there can be separation within the boundary layer for this types of flow.

With that being said it is important to understand when the laminar flow can become turbulent passing throw a transition state. For the airfoil case this will happen due to adverse pressure gradient with the angle of attack being a major responsible. Therefore, transition may be present on the wing and play a role on the development of the boundary-layers on the wings' surfaces.

In this following chapter, important concepts regarding the aerodynamic definitions, concepts and behavior of wings will be described. These will help understand the phenomenons seen in the following chapters and understand the terminologies used. The main forces acting on a simple airfoil are explored, as well as how they correlate to the flow around it.

2.1 Airfoils

An airfoil stands for the two-dimensional cross section of wing which can vary across the latter due to the introduction of sweep, taper, twist and any geometrical change involved in the wing planform. This chapter introduces the basic terminology and phenomena, associated with both type of structures.

Car wings can be designed based on previous studied airfoil profiles to achieve maximum downforce, or "negative lift".

For formula student cars, high lift low speed aerodynamics airfoils are used. In most cases, these wings have a characteristic shape represented by a rounded leading edge, a sharp trailing edge. Airfoil selection should be done comparing the stall behaviour, transition location, pressure recovery, pressure distribution and boundary-layer characteristics of various airfoils. Many geometric properties can be used when describing an airfoil, as shown in figure 2.1.

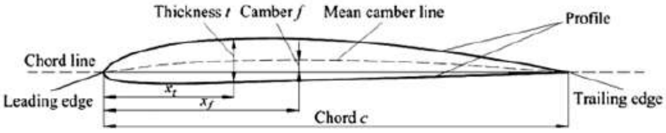

Figure 2.1: Airfoil common nomenclature

The following list describes the most common wing nomenclature generally used when describing a $2D$ airfoil and flow behaviour around it.

- Leading edge LE - point at the front of the airfoil that has maximum curvature and minimum radius;
- Trailing edge TE - point of minimum curvature at the rear of the airfoil;
- Chord line c- straight line connecting leading and trailing edges;
- Mean camber line - line midway between the upper and lower surfaces
- Thickness distribution which varies along the chord;

The forces exerted on an airfoil can be split into several components:

- Drag D – force exerted in the direction of the flow (against airfoil movement relative to the flow) by air resistance due to frontal area:

- Downforce L – resulting force on the wing due to the flow interaction in a perpendicular direction of the flow.

The remaining concepts associated with the aerodynamics of an airfoil are:

- Angle of Attack α - angle between the cord line does and the flow direction;
- Aerodynamic centre - chord-wise length about which the pitching moment is independent of the lift coefficient and angle of attack;
- Centre of pressure - chord-wise location about which the pitching moment is zero.

2.1.0.1 Aerodynamic Behavior

Lift is the major requirement under any aircraft design where the investigation of this force was firstly introduced. The lift phenomenon is correlated with the interaction between a surface and the airflow that it encounters. In the case of the airfoil, its shape directly affects how lift occurs. Pressure differences vary with the flow stream velocity as it suffers local changes in direction and magnitude as shown in figures 2.2 and 2.3. The previous phenomenon is explained by the *Bernoulli*'s principle described in equation 2.2 where permanent, incompressible flow conditions apply.

$$\frac{v^2}{2} + gz - \frac{p}{\rho} = constant \tag{2.2}$$

The three terms with pressure units that are seen in the *Bernoulli equation* and that should be distinguished are:

- Static Pressure p - force per unit area exerted by a fluid on a surface at rest relative to the fluid. Commonly associated with the pressure potential energy per unit volume;
- Dynamic pressure $\frac{1}{2}\rho U^2$ - Commonly associated with the flow energy per unit volume;
- Hydrostatic pressure ρgz - mostly associated with hydraulics as the pressure exerted within a liquid at rest with respect to adjacent bodies.

The total pressure p_T represents the sum of the previous components. One should notice that the dynamic pressure is commonly associated with the flow energy per volume unit.

When applied to air in between two points, as in an automotive aerodynamics case, the *Bernoulli equation* can be rearranged into a more intuitive form in equation 2.3.

$$p_2 - p_1 = -\frac{1}{2}\rho(U_2^2 - U_1^2) \tag{2.3}$$

The approaching flow encounters convex and concave surfaces, which create low or high-pressure regions, commonly described as a consequence of the change in velocity. As shown in figures 2.2 and 2.3, the flow around the leading edge creates a higher pressure region as its shape tends to decrease the velocity of the incoming air. In this region, a stagnation point can be found where the flow velocity is null. Here flow meets an intermediary location between the flow moving to the pressure or suction side of the airfoil. Moreover, as seen in figure 2.2, on the upper surface of the airfoil, velocity decreases and a higher pressure region forms with respect to the opposite side of the airfoil.

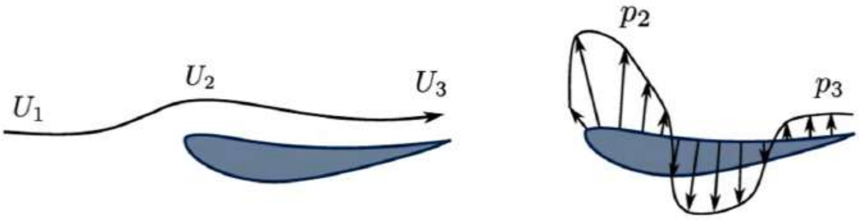

Figure 2.2: Flow across the upper surface of an airflow and it's resulting pressure distribution

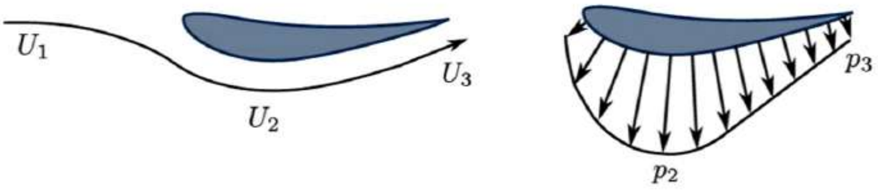

Figure 2.3: Flow across the lower surface of an airflow and it's resulting pressure distribution

As know, pressure acts normal to the encountered surfaces. While high pressure pushes the surface inwards, low pressure creates suction away from the surface. The previous phenomena creates loads acting on each surface, acting upwards in the case of aircrafts or downwards in the case of racing vehicles' applied airfoils.

It is known that the net load isn't perfectly perpendicular to airflow. Another component develops in the direction of the flow, which resembles the commonly called "air resistance"or drag and that is proportional to the surface area, normal to the flow direction as described in the drag coefficient equation 2.4.

The ground-clearance with respect to the airfoil should be studied due to the *Venturi* effect. This effect explains that if the normal area to the flow is reduced then pressure decreases and velocity increases, as is the case between the airfoil and the ground. The Venturi effect directly derives from the *Bernoulli* equation and can help clarify how lift and drag are affect by the geometry of the airfoil in the free stream case without the ground effect. The convex side of the airfoil pushes the air molecules against each other increasing their velocity and consequently decreasing it's pressure as previously stated.

The concave side does the complete opposite.

2.1.1 Aerodynamic Coefficients

From the aerodynamic forces, the drag C_D and lift C_L coefficients can be computed. The basic formulation of these coefficients that is usually present as in equations 2.4 and 2.5 where U_{ref} is the incoming free stream velocity, ρ is the air density and A_f and A_t are the frontal and vertical projection areas.

$$C_D = \frac{D}{0.5\rho A_f U_{ref}^2} \tag{2.4}$$

$$C_L = \frac{L}{0.5\rho A_t U_{ref}^2} \tag{2.5}$$

From the previous formulation it is not understood the different forces' types. Further in this chapter the different types of drag will be explained. For now let it be noted that it is possible to distinguish the pressure forces from the shear viscous forces [9] from which it is possible to write a more complete form of the general aerodynamic forces coefficients,

$$C_D = C_{Df} + C_{Dp} = \frac{D_f + D_p}{0.5\rho A_f U_{ref}^2} \tag{2.6}$$

$$C_L = C_{Lf} + C_{Lp} = \frac{L_f + L_p}{0.5\rho A_f U_{ref}^2} \tag{2.7}$$

Both drag types are obtained by adding each control volume contribution that lies on the wings' surface. Expressions 2.8 and 2.9 represent how each type of drag is calculated.

$$D_f = \sum \left(\mu A_f \frac{U_1}{\delta} \right)_x \tag{2.8}$$

$$D_p = \sum \left(-P A_f \right)_x \tag{2.9}$$

In the case o a race car rear wing the lift and drag coefficient analysis is often replace by a the coefficient multiplied by the cross sectional area as the latter varies across the structure. The shear stress and pressure are given by equations 2.10, 2.11.

$$C_f = \frac{\tau_w}{0.5\rho U_{ref}^2} \tag{2.10}$$

$$C_p = \frac{P - P_0}{0.5\rho U_{ref}^2} \tag{2.11}$$

where τ_w is the wall shear stress and P_0 is the reference pressure.

Another important coefficient that is used as a correlation parameter the aerodynamic efficiency defined as the lift over drag ratio.

2.2 Fluid viscosity and the Boundary Layer

Depending on the Reynolds number *Re* of a specific flow the viscous effect are some times relevant to consider depending on the structure scale and flow velocity. Fluid elements directly in contact with a wall experience the well know *no-slip condition* [10] [7] [4] [2]. Due to the presence of the wall, *shear stresses* τ develop in the fluid/wall interface elements which brings the fluid elements in the interface to a stop. This deceleration happens due to the diffusive forces that remove energy from the flow. Wall shear stresses τ_w then propagate and continuously decelerate the following elements in a upward direction by progressive propagation of the viscous effects between the elements at a molecular level. In a region close to a wall where the viscous stresses effects induced by the no-slip condition are quantifiable, the flow velocity exhibits a characteristic shape know as the **boundary layer** as seen in figure 2.4.

The thickness δ of this layer increases along the surface. A thicker boundary layer will create more viscous friction drag. [4]. It is usually considered that the boundary layer thickness extends from surface until the local element velocity reaches 99% of the stream velocity flow velocity $U(y) = 99\% U_\infty$.

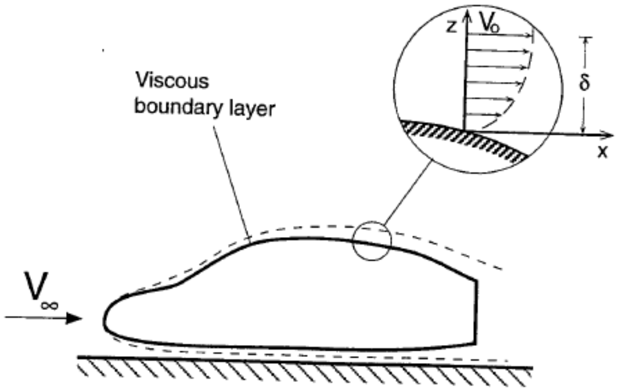

Figure 2.4: Development of the typical velocity profile of a boundary layer in a vehicle surface.

Air, as a Newtonian fluid, has shear stresses that are directly proportional to the velocity differential among the fluid elements. The constant that defines this proportionality is the dynamic viscosity μ and the relation between the velocity field and the shear stresses for Newtonian fluids is defined as in expression 2.12.

$$\tau = \mu \frac{dU}{dy} \tag{2.12}$$

If undisturbed the flow near a wall develops a laminar boundary layer as the sublayers remain with very little interaction. As they progressively increase in velocity differences and start to interact more randomly due to viscous stresses a transition to a turbulent boundary occurs even in a smooth surface body. A **turbulent** boundary layer is the most predominant state within typical engineering cases. In the case of automotive aerodynamics, as a wall bounded flow, all of these boundary layer states are likely to occur which is why correct definition and numerical modelling of these states must be applied.

2.2.1 Transition

Transition refers to exchange of the boundary layer flow condition from laminar to turbulent. Well-describing this phenomenon is an asset to obtain an accurate solution for the flow characteristics for the specific case. The transition phenomenon can be caused by different aspects such as specific Reynolds number conditions, level of surface roughness, outer flow disturbances or **turbulence intensity**. Two transition types often occur. *Bypass transition* is common in flows where the free stream turbulence is dominant like in internal turbo-machinery flows. *Natural transition* happens due to small disturbances that surpass a critical Reynolds number from which the so-called *Tollmien-Schlichting* waves form. Free stream turbulence level for external aerodynamics like the ones around motorsport wings is considerably lower [11] so natural transition is much more likely to appear in the present study. Figure 2.5 presents a detailed representation of the described natural transition which is further documented in [12].

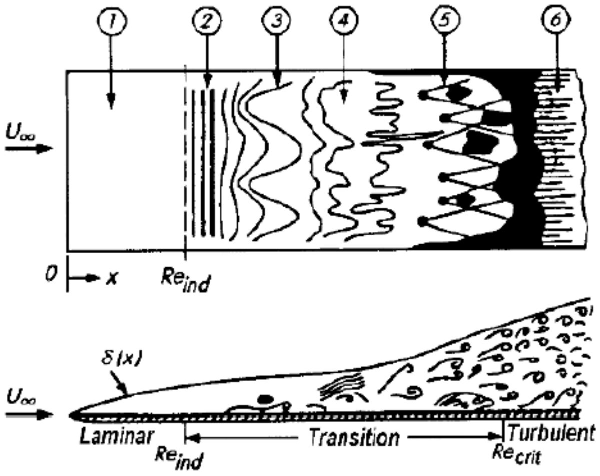

Figure 2.5: Sketch of the laminar boundary layer transition to turbulent [13]. (1) laminar undisturbed flow; (2) asymmetric Tollmien-Schlichting waves [12]; (3) three-dimensional waves and vortexes formation; (4) vortex decay; (5) formation of turbulent spots; (6) fully turbulent flow.

Forcing or inducing boundary layer transition on the suction side of a wing has been proven to delay separation [10] or to eliminate laminar separation bubble, reduce circulation [14].

2.2.2 Turbulent Boundary Layer

A turbulent boundary layer is described by the random velocity magnitudes and direction of the air particles with non-parallel components distributing momentum through out the boundary layer helping the flow to stay attached and develop a thicker boundary layer. A developed boundary layer in a car can reach a rear wing with a few centimeters high [15].

The shear stress or skin-friction coefficient C_f previously introduced in 2.1.1 comes in-handy as it represents the friction forces between the wing surface and the air. Therefore a turbulent boundary layer presents a larger skin friction coefficient with respect to a laminar boundary layer as it has more intense viscous stresses. Therefore higher skin friction coefficients create higher skin friction drag forces which will be described in the following sub-chapters. Also the thickness δ increases if the Reynolds Number Re decreases. One should notice that as car velocity increases an increasing momentum of the free stream compared to the lost momentum due to viscous effects induces a decrease in the boundary layer thickness.

2.2.2.1 Structure of a layered turbulent boundary layer

The two essential regions of the boundary layers are the inner and outer layers and can be seen in figure 2.6. The first is represented by 10 to 20% of the total boundary layer where viscous and/or turbulent stresses dominate the flow which is then divided into three sub layers to account for the different stresses sources. The second region is then dominated by inertial forces.

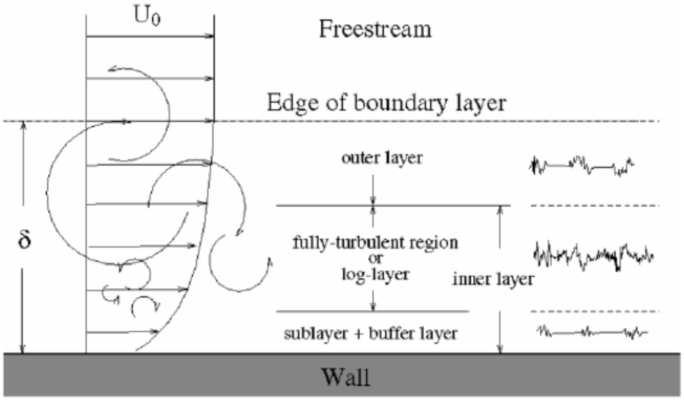

Figure 2.6: Turbulent boundary sub-layers representation.

Closer too a wall boundary the Reynolds number will decrease up to 1 which is when the viscous forces start to have higher influence then the free stream inertial parameters. after this point the mean velocity of the flow starts to depend uniquely on the distance y to the wall, flow density ρ, viscosity μ and the wall shear stress τ_w [16]. On this matter the **law of the wall** is formulated in a dimensionless matter as

$$u^+ = \frac{U}{u_\tau} = f\left(\frac{\rho u_\tau y}{\mu}\right) = f(y^+) \tag{2.13}$$

where $u_\tau = \sqrt{\frac{\tau_w}{\rho}}$ is know as the *wall friction* velocity [12], the characteristic velocity at a given wall shear stress within a turbulent flow. The dimensionless velocity u^+ and the dimensionless length $y+$ stand as two important quantities that are used to characterize the turbulent boundary sub-layers formula.

Far from the wall but also within the within the turbulent boundary layer adjacent to a body surface the mean flow velocity dependence on the wall viscous stresses decreases progressively not depending on the viscosity itself. Therefore the dependence on the boundary layer thickness δ is introduced. By considering that retardation of the flow with respect to the centerline value $U_{max} - U$ is due to the wall shear stress the **velocity-defect law** is achieved for this region - expression 2.14 [16].

$$\frac{U_{max} - U}{u_\tau} = g\left(\frac{y}{\delta}\right) \tag{2.14}$$

Within the inner-layer different sub-layers can be found:

- **Viscous sub-layer** - a thin layer where the flow bordering the wall is governed by viscous stresses which are assumed to be equal to the wall viscous stresses. Here linear relation is obtained between the non-dimensional velocity u^+ and distance to the wall y^+;
- **Buffer-layer** Where viscous and turbulent stresses are of the same order and where a good $u^+ - y^+$ relation can´t be obtained;
- **Log-law Layer** where turbulent stresses prevail and where a logarithmic relation is seen between the non-dimensional variables.

The outer-layer the flow is not dependent on direct viscous effects and is note dominated by the the core flow inertia. The velocity-defect law resembles the best relation for this region Table 2.1 and figure 2.7 present the spatial range of the sub-layers and the law of the wall and velocity-defect law applied to them whose derivation can be found in [16][10][12].

2.2.3 Separation

As the air moves along a surface the boundary layer thickens as the air in this region loses energy due to skin friction. Figure 2.8 shows how in the rearward region of an airfoil, as the air moves to the trailing edge it slows down and pressure starts to increase forming the *pressure recovery* area [2].

Flow separation can occur in an airfoil suction side due to an increase in the angle of attack or other aspects. This happens when the lack of flow energy meets the pressure

Table 2.1: Boundary Sub-layers characteristic distance to the wall and velocity-distance $u^+ - y^+$ relation by application of the law of the wall and velocity-defect law to the inner and outer sub-layers respectively. Note that A and B are constants whose findings are out of this thesis scope and $k \approx 0.4$ is the von Karman's constant which relates to the mixing length scale of turbulence $l_m = ky$ [12][16].

Layer	Sub-layer	Distance from the wall	Law applied
Inner	Viscous sub-layer	$y^+ < 5$	$u^+ = y^+$
Inner	Buffer layer	$5 < y^+ < 30$	N/A
Inner	Log-law layer	$30 < y^+ < 500$	$u^+ = \frac{1}{k} ln(y^+) + B$
Outer	Defect layer	$500 < y^+$	$\frac{U_{max} - U}{u_\tau} = ln\frac{y}{\delta} + A$

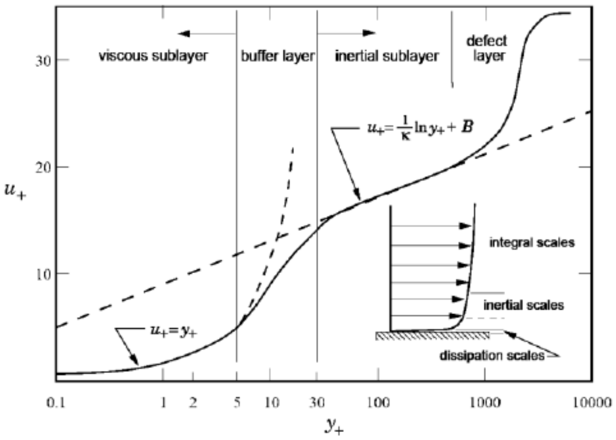

Figure 2.7: Turbulent boundary sub-layers representation. [17]

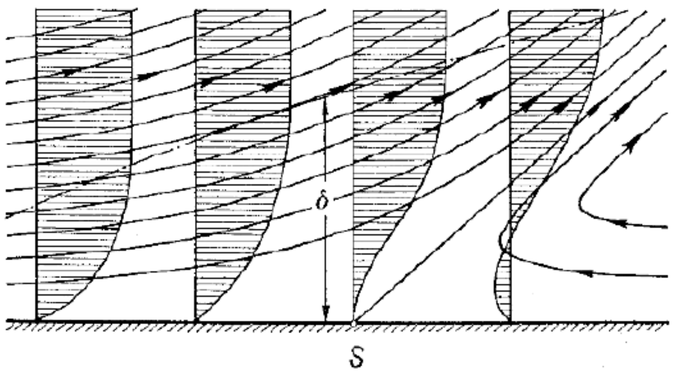

Figure 2.8: Scheme of flow separation. [2]

build up. A reversed flow region is created at the surface as seen in figure 2.9 where a further thickening of the boundary layer occurs and is transported into the outer flow at a certain angle by means of the back flow close to the wall. At the wall in separation point the velocity gradient perpendicular to the wall and the wall shear stress is null. The separation condition is then given by equation 2.15.

$$\tau_w = \mu \left(\frac{\partial u}{\partial y} \right)_w = 0 \tag{2.15}$$

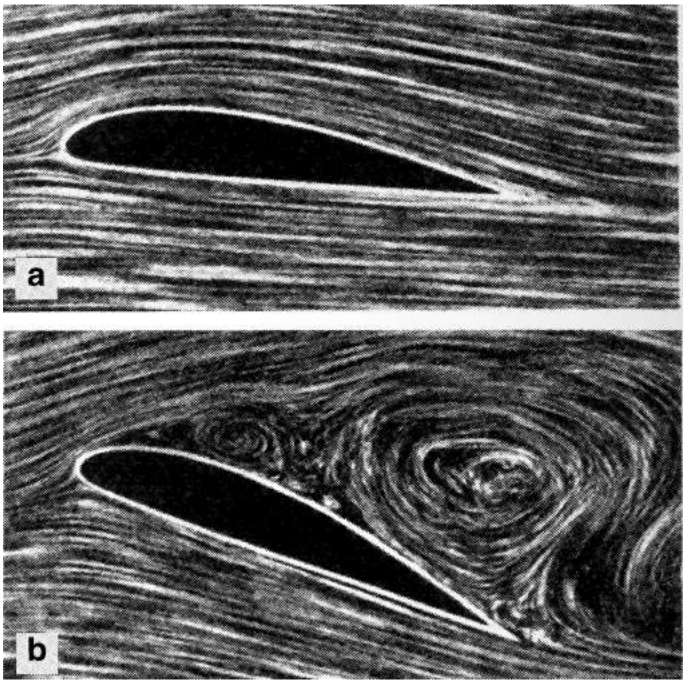

Figure 2.9: Flow around an airfoil. a) Attached flow b) Stalled airfoil with complete separation [12]

For a complete wing flow separation or at the rear of a typical race car flow separation breaks down into a large-scale turbulence known as *wake*. Flow separation rapidly reduces downforce and brings additional drag forces to the system [4], [2]. The form drag (pressure drag) is introduced is then introduced.

In a complete formula student race car or wing another phenomenon of flow separation can occur for low Reynolds numbers Re ($10^4 - 2x10^5$) which also gives rise to boundary layer transition [18] [4]. As the air approaches in a laminar way and follows the car surfaces there can be regions of local separation where the flow eventually reattaches to the following surface usually due to transition from laminar to turbulent where the flow regains sufficient energy to stay attached. This region of local flow separation is know as laminar bubble and the phenomenon can be seen in figure 2.10.

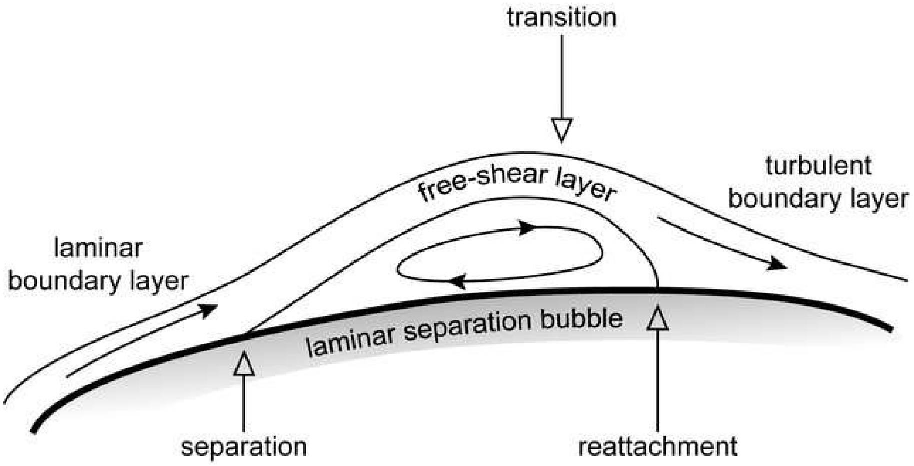

Figure 2.10: Scheme of the formation of localized laminar flow separation bubbles and transition from laminar. [19]

2.3 Types of Drag

In the case of the FST10e it is estimated through previous simulations that the rear wing may represent around 37% of the cars' total drag.

As has been presented it is possible to distinguish and sum the different types of drag [4], [15]. The total drag as the resultant force in the direction of the undisturbed flow, can then be separated into two major types of drag, **Skin-Friction Drag** and **Pressure Drag**.

The **Skin-Friction Drag** is created due to the shear stresses in boundary layer as a consequence of the deceleration of the flow near the surface as previously explained.

The **Pressure Drag** is created from the pressure distribution acting on the wing which can be due to [20] :

- Flow separation, usually correspondent to the largest drag component - *Form Drag*;
- Formation of vortexes along the structure - *Vortex Drag*;
- The lift forces created - *Induced drag*;

The definition of **Wake** should also be noticed as the violent eddying or vorticity at a larger scale behind any body. Through the total pressure plots it is possible to see that at the aft there is an increase in wake energy through the flow momentum loss.

2.4 Formula Student Aerodynamics Devices

In the history of motorsport several aerodynamic devices have been developed and added to the vehicles aerodynamic package such as front wings, rear wings, undertrays, sidepods, side wings, diffusers, among others. Every component has a great impact on the performance of the others and may have very different purposes but a common overall goal off reducing lap times.

2.4.1 Front wing

From front to back, the air flowing through the cars structure initially contacts the front wing. This element can be responsible for up to 30% of the car's total downforce in some cases. By being the first structure to meet the free stream it determines the flow behaviour over the rest of the car and underbody flow;

Taking the FST09e as example, it is possible to identify the components used in figure 2.11.

Figure 2.11: FST09e front wing and its components

The front wing is typically composed of a multi-element wings whose cross section resemble cascades of airfoils, which are can be attached to an end-plate and support plates. A lot of other components can be added within the imagination of each team.

2.4.2 Undertray and Diffusers

The undertray increases downforce a without a significant increase in drag. It creates e a low-pressure region under the car to to it's proximity to the ground accelerating the flow that is then expanded with the help of the rear and lateral diffusers smoothing it's exit avoiding a large wake formation. Underbody channels are usually also seen where strakes working as vortex generators are common as in the FST10e rear diffuser in figure 2.12. This component efficiency is well dependent on the flow intakes and degree of disturbances in the inflow.

2.4.3 Side elements

The side elements are one of the most arbitrary group of components and it is usually where the most creative components appear. Figure 2.13 shows some of the components present in the FST10e car. A wing cascade can be observed to increase the effect of a lateral diffusor, generate some downforce by these flaps themselves and also to control the flow approaching the rear wheels. Also a upside down wing is seen - the bullhorn - which is used to decrease the up wash generated from the front wing reducing the degree

Figure 2.12: Overall view of the undertray on the left and close up view on the FST10e rear diffusor and its channels.

of flow disturbances approaching the rear wing. It should be noticed that it creates some lift instead of downforce but is compensated by the rear wing increase in efficiency.

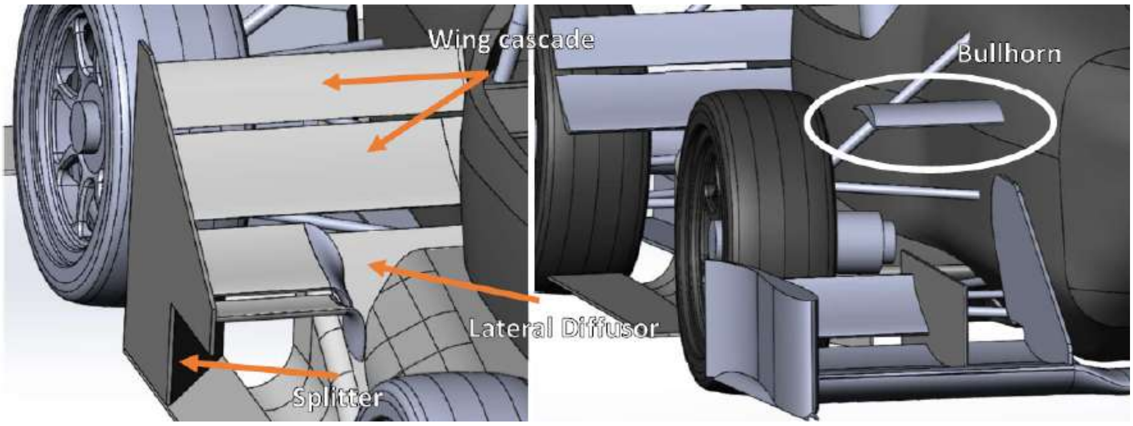

Figure 2.13: FST10e side elements

2.4.4 Rear Wing

The rear wing is an aerodynamic device that makes its appearance in almost every racing vehicle due to its potential in improving cornering speeds and high-speed braking by generating a significant amount of downforce that provides back wheel traction.

Race Car rear wings may well have the major impact on the vehicle performance. They increase significantly the forces transmitted to the rear tyres, increasing its grip capabilities and, consequently, cornering speeds.

The benefits in terms of down force, associated with a rear wing, comes at the cost of this being one of the major sources of drag. Increasing its down force capabilities that allow better cornering will have a negative impact in straight line speed due to a decrease in straight line acceleration capabilities.

A few authors have taken a deeper look into rear wings, their properties, interactions, typical flow behaviors, etc, with the main goal of achieving better design strategies.

CFD has been a very powerful tool to achieve optimization, nevertheless, meaningful conclusions by themselves can only be withdrawn from experimental testing.

Previous tests carried out by many authors allowed important knowledge to be achieved. These tests were mainly related to: wake (upstream components wake/ rear wing interaction and wing wake itself); wing edges and end-plate vorticity; aspect ratio, high-downforce wings ground effect wings (more related to the front wing) which is closer to the floor), multi-element wings and gurney flaps effects on performance, wing position (vertical and longitudinal), among others.

The rear wing has the same basis as the front wing, having almost the same impact in downforce and in balancing the car. In the case of the FST10e a gurney flap is added to the last flap which is a small tip perpendicular to the flap. It's effect is shown in figure 2.14. It has the purpose of delaying the reattachment of the flow from both sides of the air foils by creating a re-circulation area from which the flow on the pressure side will have to deflect from. This increases the pressure difference in such a way that the flow from the suction side keeps attached to the flap.

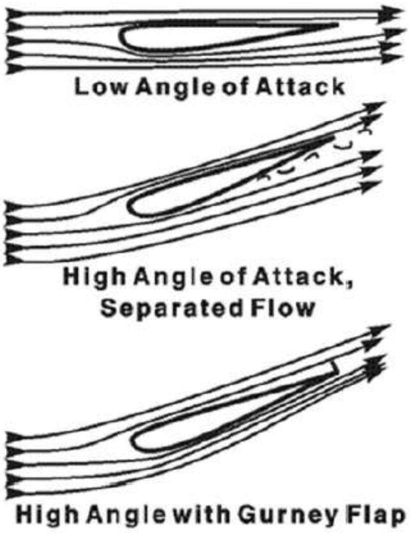

Figure 2.14: The effect of the gurney flap

Fixation of the rear wing to the car in the case of the FST10e is made using carbon fiber rods fixated to the endplates and aluminium trusses directly fixated to the main element.

2.5 Multi-Element Wings

In race cars high-lift aerodynamics several strategies to obtain maximum down force are explored. Among the previous a multi-element airfoil remains as one of the most used when trying to delay flow separation [4].

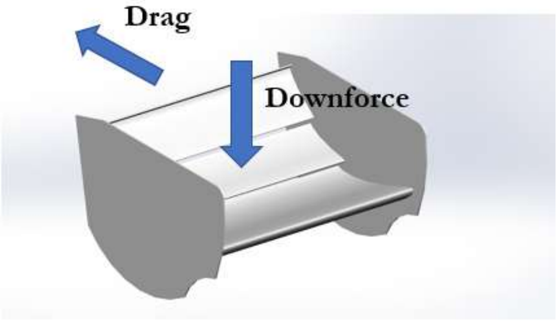

Figure 2.15: Rear wing forces

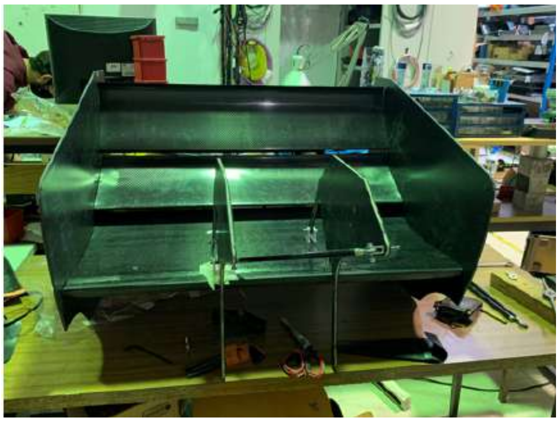

Figure 2.16: Assembled FST10e rear wing

The major benefit of using more then one airfoil profile with equivalent total chord length to a single airfoil wing is that the camber of the first option can be further increased without stalling, as explained in figure 2.17.

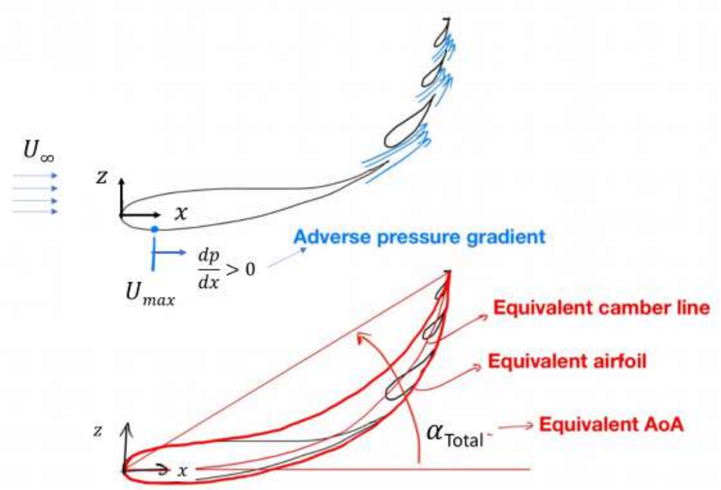

Figure 2.17: Multi-element wing with equivalent chord length allowing the flow to be re-energized. [21]

The slots in between airfoils allows for a specific amount of air to pass between profiles energizing the boundary layer in the suction side of the multi-element wing. Delaying flow separation can increase the value of the maximum achievable down-force and, as a consequence, increases drag at this configuration. The added airfoil cross-sectioned shapes are designated flaps (if down-stream of the main wing) or slats (if up-stream of the main wing).

For reference, a FST10e rear wing example can be seen in figure 2.18 were the wool threads - an recurrent cheap technique to observe flow direction [15], [4] - are forced into the rear wing flaps as the flow stays attached even at such high angles of attack. It should be noted that figure 2.18 serves only as an understanding auxiliary and should not be taken as a a validation resources as the conditions such as flow velocity were not controlled in that instance.

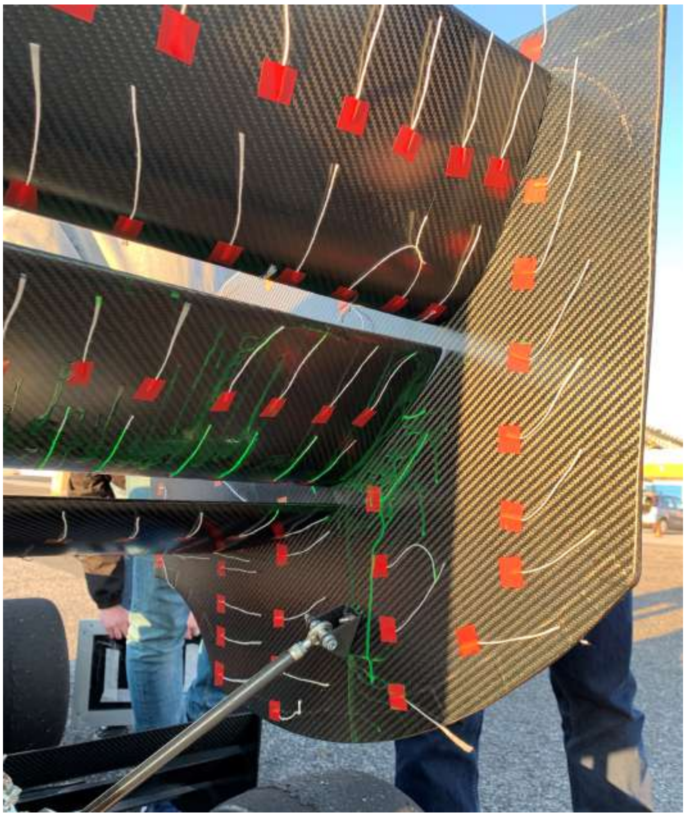

Figure 2.18: FST10e's rear wing with wool tufts were flow attached to the suction side of the flaps is seen.

Joseph Katz also explores [4] what are the changes needed in the shape of the multi-element wings when converting airplane-type wings to race car wings due to the much lower Aspect Ratio (AR). For small AR (up to $AR = 6$) the maximum achievable drag before having flow separation is considered to be around $C_L = 1.2\ AR$ [4].

In each side of a wing, endplates are commonly present. Endplates are used to help control the vortex formations at the wing tips that usually form due to the pressure difference between the upper and lower surfaces of the airfoil which will create drag and reduce downforce by lowering this pressure difference. This effect is often seen when an airplane crosses a cloud where two big vortexes form rotating inwards to aircraft and outwards in a car's front wing. Usually front wing endplates seem very complex as the shape of the endplate can also be used to control the flow that will interact with the tire and impact tire wake. For the case of the rear wing, in [22] the endplate shape is explored to understand how it impacts the flow through the wing.

2.5.1 Vortical Flows and Endplates

The flow past a wing tends to be complex and understanding the trends of its behaviour is crucial when trying to optimize its performance. Due to the specific traditional shape of the application of inverted wings in motorsport different flow structures and phenomena are seen and studied. In the various lift-generating components vortexes are heavily present and influence the forces acting on the wing. In finite wings with no endplates the pressure differential between the suction and pressure side can't be sustained which means that the flow will go from the pressure to suction side creating air movement in a swirling manner at the wing tips. This originates two large trailing vortexes due to the finite wing geometry [4] [23] as schematized in figure 2.19 a). Considering a finite wing introduces the tri-dimensional component into equation and therefore, the section aerodynamic properties, such as the pressure distribution, are not constant as in the corresponding section airfoil. The wing-tip vortexes are know for creating slight change in the flow direction angle know as *downwash* [23], [10]. The presence of this *induced* angle of attack α_i tilts the *effective* angle of attack α_{eff} that each section of the wing with respect to the geometric angle of attack of the wing α. This relation is presented in equation 2.16 and figure 2.19 b).

$$\alpha_{eff} = \alpha - \alpha_i \tag{2.16}$$

The consequence of this phenomenon is that there is a local lift component in the free stream direction creating and *induced* drag component as a form of **pressure drag**, discussed in the chapter 2.3.

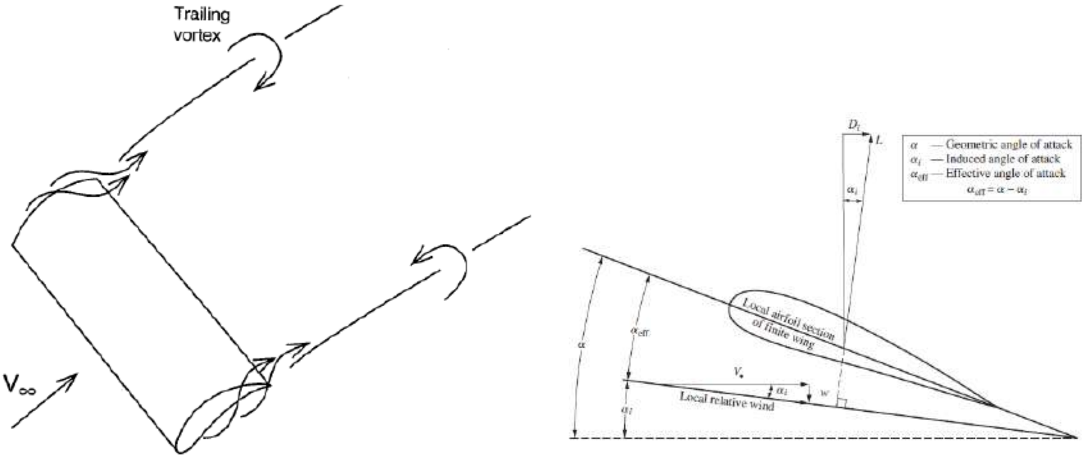

(a) Wingtip vortexes schematized. [4]

(b) Effective angle of attack α_{eff} relation with the geometric α and $inducedangleofattack$ [23]

Figure 2.19: Wing-tip vortexes effect.

To reduce the *induced* drag by the wing tip vortexes, endplates were introduced. These break the available path of the flow from pressure to suction side. Nevertheless in a classic rectangular endplate, smaller vortexes are created at the lower and top edges know as the primary and secondary vortexes respectively. This effect is schematized in figure 2.20. In [22] the effect of the endplate geometry is experimented in order to reduce the induced drag component proved to work when changing its geometry into a vertical wing. In [24] the ground effect over the endplate vortexes is explored providing that it affect the strength and core position of the vortexes. In both of the previous studies also cornering effects are considered. The endplates vortexes will be analysed in the current study to understand how the DRS configurations influence them and if the induced drag of these vortexes can be responsible in efficiency shifts.

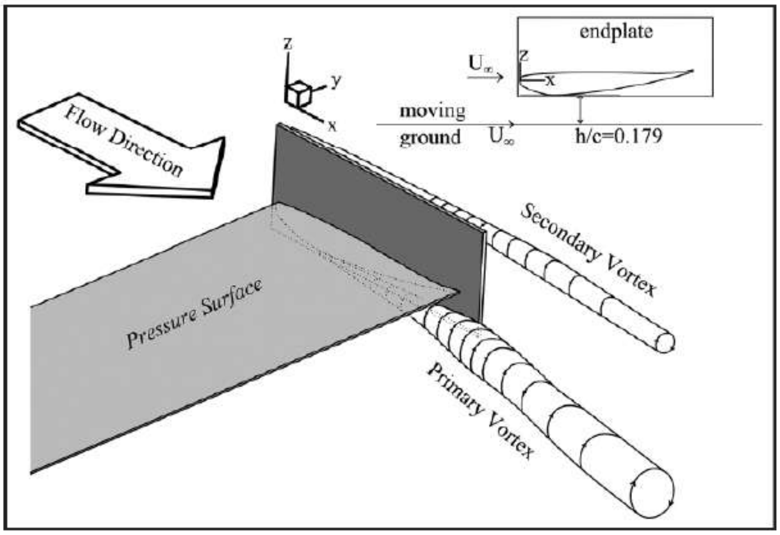

Figure 2.20: Formation of the primary and secondary vortexes on the inside and on the outside of the endplate respectively.

The effect of a wing proximity to the ground is to constrain the flow below the suction surface further accelerating it when compared with a wing out of ground effect.

[25] [3]

2.6 Active Aerodynamics

The purpose of introducing active aerodynamics in motorsport came from the fact that along the track, the conditions that the car is exposed to are constantly changing. Aerodynamic performance of a vehicle can be enhanced by introducing a system that intends to adapt the aerodynamic components of the car to the local requirements. For this reason active aerodynamics were introduced. The number of different active aerodynamic systems that have been developed are enormous. For example, Miliken [2] discusses the enhancement that can be achieved by guiding or blowing air into the boundary layer or removing it using suction which as been proven to effectively delay the stall condition by drawing back flow separation. A related popular approach of this type of active aerodynamics in Formula 1 is the **F-Duct**. This system was introduced by McLaren in 2010 estimated to increase the overall car's top speed by 6 to 10 km/h [26], also working as a drag reduction system which wouldn't violate the F1 regulations at the time. The functioning of the system can be seen in figure 2.21. The systems includes 2 ducts where duct number 2 has two outlets. One of the outlets redirects air flow to the rearwing flap when in a straight line speed. The reason behind this flow field disruption is that it induces separation in the flap which will reduce the overall donwforce and consequently the drag forces.

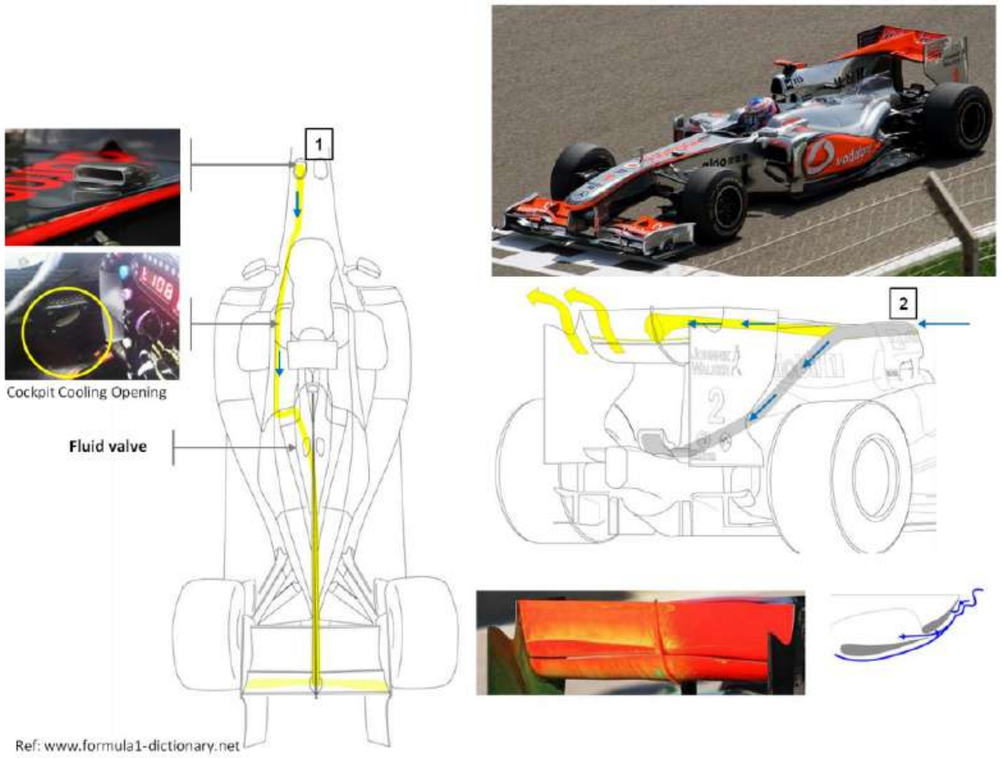

Figure 2.21: F duct

The concepts of using discrete but dynamically positioned or fully automate and continuous motioning of aerodynamics devices are not new. In 1996, the Chaparral 2E already had a single element wing with an variable angle of attack controlled by the driver through a pedal [27] [28].

Most active aerodynamics concepts have been previously developed by professional racing teams, such as Formula 1 teams. The most well known form of active aerodynamics in motorsport is the Drag Reduction System, which was introduced in Formula 1 in 2011 [15]. The system aimed at improving the overtaking ability when a car was closely following another, as seen in figure 2.22, under specific conditions dictated by the FIA - *Federation Internationale de L'Automobile*. The flap of the two-element rear wing's would rotate around the trailling edge, i.e. the nose of the flap would be raised, to a low drag configuration giving a straight line speed advantage.

The Drag Reduction System (DRS) introduced in Formula 1 has prevailed as a strategy

Figure 2.22: A closed rearwing is seen on top whose configuration can be exchanged to DRS configuration as seen bellow under certain regulated conditions

to keep races more competitive as it gives a straight line acceleration advantage to the car that can deploy this system under specific circumstances.

For every type of motorsports the major advantage of using DRS is how the lap time can be reduced by increasing the acceleration capability when reducing the drag forces in sections of the track where cornering ability and maximum grip is not the most important factor. In formula student competitions the system brings additional benefits. The reduction in air resistance will also have an impact on the power consumption which is of major importance in the endurance event. Considering the DRS system in the rear wing, it can help to increase the stability of the car and, in some cases, even act as a aerodynamic brake reducing the "pitch"effect of the car. The DRS concept that is studied in this dissertation will focus on the rotation of the two rear flaps of the FST10e rearwing around specific centers of rotation as shown in figure 2.23. Different test to achieve a first iteration of the best DRS configuration will be done in terms of angles and center of rotation.

2.6.1 Drag Reduction System

Several active aerodynamics concepts and approaches have been applied by different formula student with different purposes and focuses. In Formula Student competitions the growing interest in active aerodynamics started to appear from 2010 onward. 2011

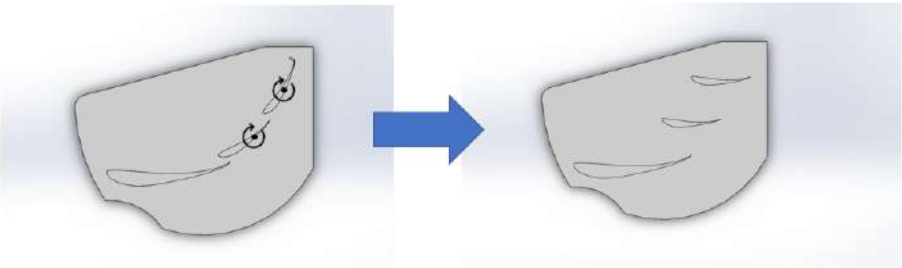

Figure 2.23: Rotation of the two flaps around a projection of the 50% of the chord on the camber line.

marked the year of the first introduction of a DRS in Formula SAE history by the Oklahoma Formula SAE team [27].

From early on the advantages of have a real time adjustment of the flaps configurations have been considered and implemented.

In [29] a formulation of the dynamic properties of the vehicle has been co-related with behaviour of the the active aerodynamic system in order to improve handling. The system would generate the right downforce in each tire druing acceleration and cornering maneuvers and consequently balance the load transfers at peak performance during acceleration and cornering. An implementation of a system to control each tire vertical force was investigated through tire modelling. A 8-DOF nonlinear vehicle model with nonlinear tire model was considered to simulate the dynamic performance of the car. The vehicle steady-state and transient responses are considered, according to [2] to achieve the optimal downforce in each tire but lacks accuracy when a constant drag coefficient is considered in the vehicle dynamics model. The studied system [29] proved to have load transfers of the same order of the downforce that could be generated by the system by comparing the vehicle model simulations with the wings CFD simulations. Hence it was recognized that a small racing car, that ran at lower velocities, could have improved performance if each tire would have an individually assigned wing with variable angles of attack. For this purpose both the front and rear wings where split in two as shown in figures 2.24 and 2.25.

Figure 2.24: Front wing with lateral flaps individually controlled.

Figure 2.25: Rear wing with a split second flap to be controlled individually.

In a 2013 a widely citted thesis was developed around the complete design and implementation of a active aerodynamic system on the University of Texas Formula SAE car [30]. The self-design five element front and rear wings, whose downforce was considered to be an asset when cornering, were also considered to produce significant drag forces.

The main objective of the project was to maximize the straight line acceleration capabilities by creating a system that could actively change the flap angles between maximum downforce and minimum drag configurations for each side of the car. This configuration was achieved by a set of two-dimensional CFD simulations that were followed by the implementation and testing of the electro-mechanical actuation system with a self-developed control system. The movable flaps were rotated about a quarter of the chord. Figures 2.26 and 2.27 show the mechanical designed systems in the opened and closed positions respectively.

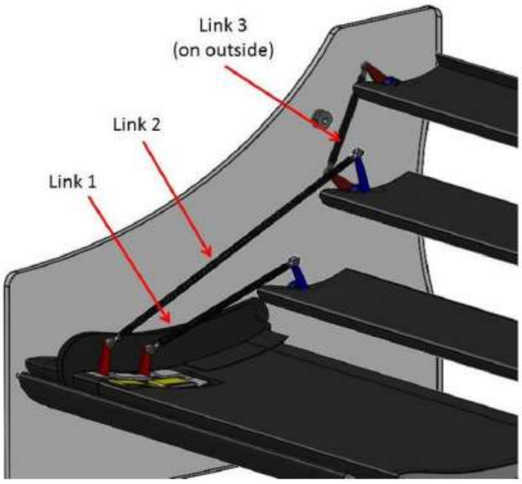

Figure 2.26: Rear wings mechanical system in opened position.

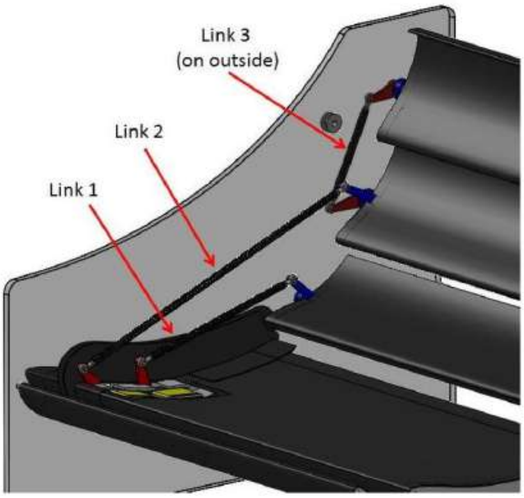

Figure 2.27: Rear wings mechanical system in closed position.

The final mechanical integration of is shown in 2.28.

In [27] the analogy of the state of the art of an Formula 1 drag reduction system at the time is done. It states that such systems allows for enhanced downforce during cornering and braking switching to a low drag configuration. The reduced drag, as a consequence of a single flap rotation, is referred as the aerodynamic decoupling of the high-lift producing multi-element wing. The authors in [27] use the 2011 configuration of the Monash front and rear wings as their study starting point. The simulation setup of this study is used as one of the references in chapter 4. Full scale wind-tunnel tests were performed on the isolated wing progressively turning the flaps until a 0° angle of attack obtaining the CFD and wind tunnel (WT) correlation.

Figure 2.28: UTA 2013 Formula SAE car with DRS system. [30]

3

AERODYNAMICS AND MATHEMATICAL FORMULATION

In the next chapter the set of equations that describe the aerodynamic fluid behaviour are described as well as the set of aerodynamic assumptions, models, coefficients, solvers and further techniques to accurately evaluate the case-study.

3.1 Aerodynamic Theory

Any fluid flow considered macroscopically as a continuum should be able to be represented within the conservation laws of physics. The basis of these laws should be within the following statements:

- Mass should be conserved;
- Rate of change of momentum should equal the sum of forces acting on a fluid particle;
- Rate of change of energy should equal the sum of rate of work and heat transfer in a particle - first law of thermodynamics.

When describing the external aerodynamics of a race car wing at low Reynolds numbers an incompressible, isothermal, viscous flow should be assumed whereas the fundamental equations that should be understood are the continuity and momentum equations presented as 3.1 and 3.2 respectively. From the momentum transport equation, *Newton's Second Law* it is possible to derive the differential equations of motion 3.2 satisfying the continuum assumption [31].

$$\rho\left(\frac{\partial u}{\partial x}+\frac{\partial v}{\partial y}+\frac{\partial w}{\partial z}\right)=0 \tag{3.1}$$

$$\rho g_x + \frac{\partial \sigma_{xx}}{\partial x} + \frac{\partial \tau_{yx}}{\partial y} + \frac{\partial \tau_{zx}}{\partial z} = \rho\left(\frac{\partial u}{\partial t} + u\frac{\partial u}{\partial x} + v\frac{\partial u}{\partial y} + w\frac{\partial u}{\partial z}\right), \tag{3.2a}$$

$$\rho g_y + \frac{\partial \tau_{xy}}{\partial x} + \frac{\partial \sigma_{yx}}{\partial y} + \frac{\partial \tau_{z}}{\partial z} = \rho\left(\frac{\partial v}{\partial t} + u\frac{\partial v}{\partial x} + v\frac{\partial v}{\partial y} + w\frac{\partial u}{\partial z}\right), \tag{3.2b}$$

$$\rho g_z + \frac{\partial \tau_{xz}}{\partial x} + \frac{\partial \tau_{yz}}{\partial y} + \frac{\partial \sigma_{zz}}{\partial z} = \rho\left(\frac{\partial w}{\partial t} + u\frac{\partial w}{\partial x} + v\frac{\partial w}{\partial y} + w\frac{\partial w}{\partial z}\right), \tag{3.2c}$$

Also, for a Newtonian fluid it is possible to relate the viscous stresses with the rate of shearing strain proportionally. Stresses can be represented as functions of the fluid properties and velocity gradients, in a simpified notation 3.3 where $U_i = u$ an $x_i = x$ when $i = x$.[1]

$$\tau_{ij} = \mu\left(\frac{\partial U_i}{\partial x_j} + \frac{\partial U_j}{\partial x_i}\right), \tag{3.3a}$$

$$\frac{\partial \sigma_{ij}}{\partial x_j} = -\frac{\partial p}{\partial x_i} + \mu\left[\frac{\partial^2 U_i}{\partial x_j^2} + \frac{1}{3}\frac{\partial}{\partial x_i}\left(\frac{\partial U_k}{\partial x_k}\right)\right] \tag{3.3b}$$

Introducing the previously described relations into the differential equations and considering isothermal, incompressible flow with constant viscosity it is possible to obtain the differential equations of motion, the Navier-Stokes equations 3.4,

$$\frac{DU_i}{Dt} \equiv \frac{\partial U_i}{\partial t} + U_j\left(\frac{\partial U_i}{\partial x_j}\right) = -\frac{1}{\rho}\frac{\partial p}{\partial x_i} + \nu\frac{\partial^2 U_i}{\partial x_j^2} + f_i \tag{3.4}$$

where $\frac{D}{Dt} = \frac{\partial}{\partial t} + \vec{U}.\nabla$ is the total derivative, $\nabla = \frac{\partial}{\partial x}\vec{e}_x + \frac{\partial}{\partial x}\vec{e}_y + \frac{\partial}{\partial x}\vec{e}_z$ is the vectorial operator $\nu = \mu/\rho$ is the kinematic viscosity, f_i is the mass force in the component i per mass unit. meaning that the total change in momentum transport per mass unit equals the sum of the total change in the flow as a function of time with the convective change associated with the transportation of one fluid particle from one point to another with different velocity.

3.2 Turbulence

Turbulence is the cause of the known flow of eddies that have dynamically complex behaviors and interactions. The need to predict turbulence and its effects in engineering induced research around this topics from which several numerical methods appeared. Two of them will be discussed and explored in this work:

- **Turbulence models for the Reynolds-averaged Navier-Stokes equations**: They're focused on the mean flow and the turbulence effects on its properties. The flow

---

[1] The detailed derivations of these equations can be found in [10], [12], [32].

behaviour is averaged and the fluctuations terms appear in the time averaged Navier-Stokes equations. The latter are then modelled by classical turbulence numerical models. This method is know for requiring less computational resources to obtain more precise results but are usually enough for most engineering cases.

- **Large-eddy Simulation**: Tries to predict the behaviour of larger eddies by space filtering the unsteady Navier-Stokes equations. It rejects smaller eddies that influence the resolved flow by the means of a sub-grid scale model. Solving unsteady Navier-Stokes equations requires bigger computational resources, both in terms of storage and computation capabilities.

More recently, new models have been developed that combine the previous two. The increased predictability of the turbulent flow properties in the Large Eddy models is merged with the RANS models to achieve more efficient computational times. An example of a research combination is the designated Detached Eddy Simulation [33].

3.2.1 Reynolds Averaged Navier-Stokes Equations (RANS)

With the purpose of analysing a incompressible and viscous flow, the continuity and momentum equations should be solved. The variables that this equations are solved for are the U_x, U_y, U_z and p. The form of the *Reynolds Averaged Navier-Stokes* equations is considered when time-dependent variables of the momentum equations are converted into time averaged ($\bar{u}$) and fluctuation components (u'). This method is called the *Reynolds* decomposition $u = \bar{u} + u'$. The resulting RANS equations are equations 3.5 and 3.6, given in the *Einstein* notation in Cartesian coordinates. These can be used with approximations based on knowledge of the properties of flow turbulence to give approximate time-averaged solutions to the Navier–Stokes equations [17].

$$\rho \frac{\partial \bar{u}_i}{\partial x_i} = 0 \tag{3.5}$$

$$\underbrace{\rho \bar{u}_j \frac{\partial \bar{u}_i}{\partial x_j}}_{\text{Change in mean momentum}} = \underbrace{\rho \bar{f}_i}_{\text{Mean body force}} + \frac{\partial}{\partial x_j}[\underbrace{\bar{p}\delta_{ij}}_{\text{Isotropic Stress}} + \underbrace{\mu\left(\frac{\partial \bar{u}_i}{\partial x_j} + \frac{\partial \bar{u}_j}{\partial x_i}\right)}_{\text{Viscous Stresses}}] \underbrace{-\overline{\rho u_i' u_j'}}_{\text{Apparent Stress}} \tag{3.6}$$

In the previously described momentum equation it should be noticed that the isotropic stress is thanks to the mean pressure field and the apparent stress issue to the fluctuating velocity field, usually referred to as the Reynolds stress. The Reynolds Stress non-linear term is the basis of the RANS turbulence models as it requires additional modeling to close the RANS equation. This time averaged component can be written in the form of equation 3.7 where μ_t is the turbulent dynamic viscosity that the turbulence models solve for.

$$-\overline{\rho u_i' u_j'} = \mu_t(\frac{\partial \bar{u}_i}{\partial x_j} + \frac{\partial \bar{u}_j}{\partial x_i}) \tag{3.7}$$

3.2.2 RANS Models

There are four main RANS turbulence models that can be applied to the current investigation which should be described:

- Spallart-Almarras of 1 equation ;
- $\kappa - \epsilon$ of 2 equations;
- Wilcox $\kappa - \omega$ of 2 equations;
- Menter's $\kappa - \omega$ Shear Stress Transport of 2 equations.

Four RANS turbulence models are recommend by several authors when predicting external aerodynamics: Spallart-Almarras, standard κ-ω and κ-ω SST. Each has a specific approach when solving the discussed averaged Navier–Stokes equations which govern the velocity and pressure of a fluid flow.

3.2.3 κ-ω SST Model

The considered as most suitable RANS turbulence model is the Menter's developed κ-ω SST.

Historically, it is important to have in mind that the κ-ϵ and the standard κ-ω were previously developed although both had limitations when performing certain simulations. Firstly the κ -ϵ was inadequate in a variety of flows as it was unreliable near wall damping functions (f), as will be explained later. Secondly the κ -ω model was developed to perform better at near wall conditions being less sensitive near wall. Although having sensitivity to the free stream of turbulence at the inlet, it does not require near wall damping functions. It was then found that both models didn't predict a correct separation from the surface when compared with the literature, as the wall shear stress was too high.

For the type of case that it is applied in this study, and for most external aerodynamics cases, the κ-ω SST model was developed mainly solving the prediction problems of flow separation.

For standard κ -ϵ equation 3.8 describes the transport equation for turbulent kinetic energy κ while equation 3.9 describes the transport equation for the turbulent dissipation rate ϵ.

$$\frac{\partial \rho \kappa}{\partial t} + \nabla \cdot (\rho U \kappa) = \nabla \cdot \left(\left(\mu + \frac{\mu_t}{\sigma_\kappa} \right) \nabla \kappa \right) + P\kappa - \rho \epsilon \tag{3.8}$$

$$\frac{\partial\rho\epsilon}{\partial t}+\nabla\cdot(\rho U\epsilon)=\nabla\cdot\left(\left(\mu+\frac{\mu_t}{\sigma_\kappa}\right)\nabla\epsilon\right)+C_{1\epsilon}P_\kappa\frac{\epsilon}{\kappa}-C_{2\epsilon}P_\kappa\frac{\epsilon^2}{\kappa} \tag{3.9}$$

Noticing that $\epsilon = C_\mu\kappa\omega$ a direct comparison with the $\kappa-\omega$ model can be done by substituting the previous expression in the transport equation for the turbulent dissipation rate ϵ. This substitution results in expression 3.10 whereas for the real $\kappa-\omega$ equation 3.11 it can be seen that the last term is lacking.

$$\frac{\partial\rho\omega}{\partial t}+\nabla\cdot(\rho U\omega)=\nabla\cdot\left(\left(\mu+\frac{\mu_t}{\sigma_\kappa}\right)\nabla\omega\right)+\frac{\gamma}{\nu_t}P_\kappa-\beta\rho\omega^2+2\frac{\rho\sigma\omega^2}{\omega}\nabla\kappa:\nabla\omega \tag{3.10}$$

$$\frac{\partial\rho\omega}{\partial t}+\nabla\cdot(\rho U\omega)=\nabla\cdot\left(\left(\mu+\frac{\mu_t}{\sigma_\kappa}\right)\nabla\omega\right)+\frac{\gamma}{\nu_t}P_\kappa-\beta\rho\omega^2 \tag{3.11}$$

All of the terms are the same as previously said with the exception of the last term. For both equation, on the left-hand side it can be seen the temporal derivative and convection term, and on the right-hand side the diffusion, production and dissipation terms.

For the additional term, if multiplied by $(1-F_1)$ as in 3.12

$$2(1-F_1)\frac{\rho\sigma\omega^2}{\omega}\nabla\kappa:\nabla\omega \tag{3.12}$$

it is possible to blend both $\kappa-\epsilon$ and $\kappa-\omega$ if $F_1=0$ or $F_1=1$ respectively. This can be of interest because it creates an alternative calculation path where it is possible to use the $\kappa-\omega$ near the wall, where it gets better near wall behaviour, switching to the $\kappa-\epsilon$ far from the wall where it is important to have less sensitivity to the inlet imposed turbulence intensity and turbulence length scale.

Adding the turbulent kinetic energy transport equation 3.8 to the ϵ substituted turbulent diffusion transport equation 3.10 a model refered by *Menter* in [34] as the $\kappa-\omega BSL$ model where the switch between $\kappa-\epsilon$ and $\kappa-\omega$ with the help of a function F_1.

Note: The $\nabla\kappa:\nabla\omega$ notation represents the tensor inner product of the two gradient terms $\nabla\kappa$ and $\nabla\omega$ meaning 3.13

$$\nabla\kappa:\nabla\omega=\frac{\partial\kappa}{\partial x_j}\frac{\partial\omega}{\partial x_j}=\frac{\partial\kappa}{\partial x}\frac{\partial\omega}{\partial x}+\frac{\partial\kappa}{\partial y}\frac{\partial\omega}{\partial y}+\frac{\partial\kappa}{\partial z}\frac{\partial\omega}{\partial z} \tag{3.13}$$

The functionality of the blending function F_1 turns self-explanatory with figure 3.1 where it can be seen that it takes the value of 1 in a inner region of the boundary layer and transitioning to zero when it gradually gets away from the outer region. Studies done proved that the blending function can have a complex equation but initially it is defined as a smooth transition between the models by assuming equation 3.14 form where the variable arg_1 intuitively assumes the dependence on the distance to the closest wall (Equation 3.15) , usually the normal distance y.

$$F_1 = tanh(arg_1^4) \tag{3.14}$$

$$arg_1 = min\left[max\left(\frac{\sqrt{\kappa}}{\beta^* \omega d}, \frac{500\nu}{d^2\omega}\right), \frac{4\rho\sigma_{\omega 2}\kappa}{CD_\kappa \omega d^2}\right] \tag{3.15}$$

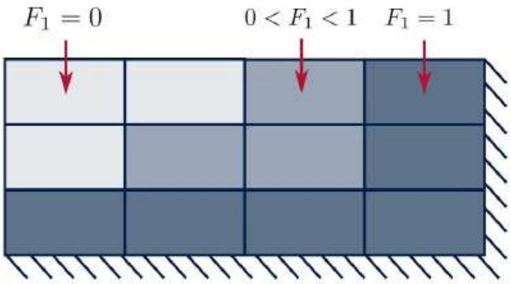

Figure 3.1: Blending function values with respect to the mesh element position

By assuming ϕ_1 as any constant in the original $\kappa-\epsilon$, ϕ_2 as any constant in the in the readjusted model and ϕ as a constant in the new model then the following relationship between the models [34] can be obtained:

$$\phi = F_1\phi_\omega + (1-F_1)\phi_\epsilon \tag{3.16}$$

Finally for the $\kappa-\omega$ Shear-Stress Transport (SST) model a viscosity limiter (an eddy viscosity modifier) is introduced (Equation 3.18) to account for the effect of the transport of the principal turbulent shear stress $\tau = \rho\overline{u_i' u_j'}$ that for conventional two-equation models can be rewritten in form of equation 3.17 as described in [34].

$$\tau = \rho\sqrt{\frac{Production_\kappa}{Dissipation_\kappa}}a_1\kappa \tag{3.17}$$

It know achieves better agreement with experimental measurements and improves the model's performance in flows with adverse pressure gradients and wake regions. One should take into account that F_2 takes the usual functionality of the first presented blending function F_1. If F_2 or S, the magnitude of the shear strain, are large then the viscosity is limited (reduced).

$$\mu_t = \frac{a_1\rho\kappa}{max(a_1\omega, SF_2})) \tag{3.18}$$

The last statements mean that F_2 takes the same hyperbolic tangent form (Equation 3.19) as seen for F_1 to ensure a smooth transition between original viscosity and limited viscosity, while arg_2 still ensures the dependence on the distance to the closest wall (Equation 3.20).

$$F_2 = tanh(arg_2^4) \tag{3.19}$$

$$arg_2 = max\left(\frac{2\sqrt{\kappa}}{\beta^*\omega d}, \frac{500\nu}{\omega d^2}\right) \tag{3.20}$$

The κ-ω SST model can now be rewritten in the form of equations 3.21 and 3.22.

$$\frac{\partial \rho\kappa}{\partial t} + \nabla\cdot(\rho U\kappa) = \nabla\cdot[(\mu+\mu_t\sigma_\kappa)\nabla\kappa] + P_\kappa - \beta^*\rho\kappa\omega \tag{3.21}$$

$$\frac{\partial\rho\omega}{\partial t} + \nabla\cdot(\rho U\omega) = \nabla\cdot\left(\left(\mu+\frac{\mu_t}{\sigma_\kappa}\right)\nabla\omega\right) + \frac{\gamma}{\nu_t}P_\kappa - \beta\rho\omega^2 + 2(1-F_1)\frac{\rho\sigma\omega^2}{\omega}\nabla\kappa:\nabla\omega \tag{3.22}$$

As specified in figure 3.2 taken from Star CCM+ the closure coefficients for the specified model are:

$$\begin{gathered}\sigma_{\kappa 1} = 0.85, \quad \sigma_{\omega_1} = 0.5, \quad \beta_1 = 0.0750, \quad a_1 = 0.31, \\ \beta^* = 0.09, \quad \kappa = 0.41, \quad \gamma_1 = \frac{\beta_1}{\beta^*} - \frac{\sigma_{\omega 1}\kappa^2}{\sqrt{\beta^*}}\end{gathered} \tag{3.23}$$

$$\sigma_{\kappa 2} = 1.0, \quad \sigma_{\omega_2} = 0.856, \quad \beta_2 = 0.0828, \quad \gamma_2 = \frac{\beta_2}{\beta^*} - \frac{\sigma_{\omega 2}\kappa^2}{\sqrt{\beta^*}} \tag{3.24}$$

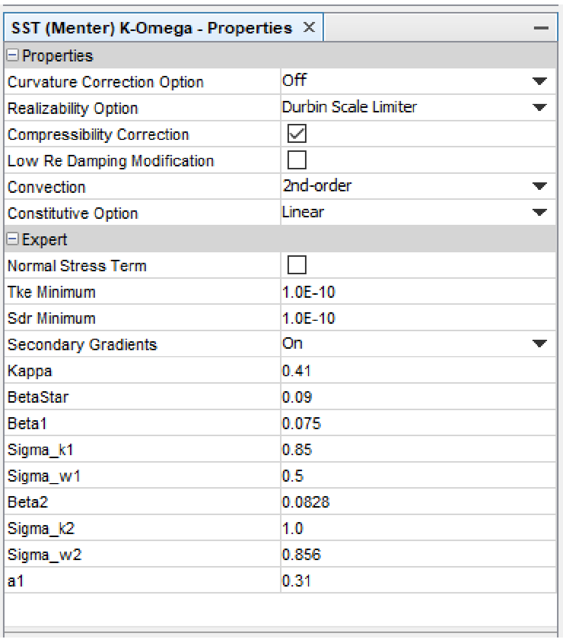

SST (Menter) K-Omega - Properties

Properties	
Curvature Correction Option	Off
Realizability Option	Durbin Scale Limiter
Compressibility Correction	☑
Low Re Damping Modification	☐
Convection	2nd-order
Constitutive Option	Linear
Expert	
Normal Stress Term	☐
Tke Minimum	1.0E-10
Sdr Minimum	1.0E-10
Secondary Gradients	On
Kappa	0.41
BetaStar	0.09
Beta1	0.075
Sigma_k1	0.85
Sigma_w1	0.5
Beta2	0.0828
Sigma_k2	1.0
Sigma_w2	0.856
a1	0.31

Figure 3.2: Star CCM+ $\kappa-\omega SST$ model coefficients

Ense the κ-ω SST model becomes the most widely used model for external aerodynamics and other simulations were separation is important as it agrees better with the experiments of slightly separated flows than the other RANS models due to the viscosity limiter introduced.

3.3 Transition Models

For the specific type of aerodynamics problem considered, it is important to have a correct prediction of the laminar-turbulent transition so the presence of a transition model should be considered and is importance should be evaluated.. Transition models are coupled with turbulence models and are based on solving an additional transport equation for intermittency γ [35]. Intermittency is the concept of the time over which the flow is turbulent where $\gamma = 1$ correpondes to a fully turbulent flow and $\gamma = 0$ a fully laminar flow.

Two correlation based transition models are available: γ-SST Transition Model and $\gamma - Re_\theta$-SST.

3.3.1 γ Transition Model

For the studied case a local approach one-equation correlation-based transition model is applied, the γ **Transition Model** [36], which adds one equation for the turbulence intermittency γ, equation 3.25. In equation 3.25 ρ is the density, $\bar{v}$ is the mean velocity vector, μ is the dynamic viscosity, μ_t is the turbulent eddy viscosity, σ_f is a model coefficient, P_γ is the production term and E_γ is the Destruction Term.

$$\frac{d}{dt}(\rho\gamma) + \nabla\cdot(\rho\gamma\bar{v}) = \nabla\cdot\left[(\mu + \frac{\mu_t}{\sigma_f})\nabla\gamma\right] + P_\gamma - E_\gamma \tag{3.25}$$

The introduced coefficients for the γ Transition Model are shown in figure 3.3.

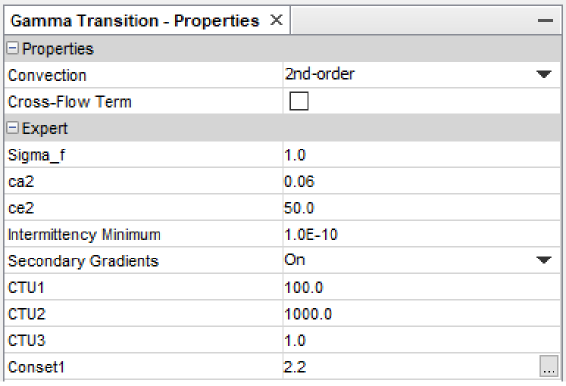

Properties	
Convection	2nd-order
Cross-Flow Term	☐
Expert	
Sigma_f	1.0
ca2	0.06
ce2	50.0
Intermittency Minimum	1.0E-10
Secondary Gradients	On
CTU1	100.0
CTU2	1000.0
CTU3	1.0
Conset1	2.2

Figure 3.3: Star CCM+ γ Transition model coefficients.

3.3.2 $\gamma - Re_\theta$ Transition Model

The previously described model model is a simplification of the widely used $\gamma - Re_\theta$ **Transition Model** model. This model also accounts for a transport equation for the transition momentum thickness Reynolds number $\overline{\mathrm{Re}}_{\theta t}$ [37] which relates this quantity with a vorticity-based Reynolds number. This equation is described in equation 3.26 where $\sigma_{\theta t}$ is the model coefficient, $P_{\theta t}$ is the production term and D_{SCF} is the cross-flow term.

$$\frac{d}{dt}\left(\rho\overline{\mathrm{Re}}_{\theta t}\right) + \nabla\cdot\left(\rho\overline{\mathrm{Re}}_{\theta t}\overline{\mathbf{v}}\right) = \nabla\cdot\left[\sigma_{\theta t}(\mu + \mu_t)\nabla\overline{\mathrm{Re}}_{\theta t}\right] + P_{\theta t} + D_{\mathrm{SCF}} \tag{3.26}$$

Accounting for an extra equation brings extra computational expense to the simulation and as a large number of iterative equations is expected this transition model will be avoided if the $\gamma - SST$ Model proves closely efficient.

3.4 Finite Volume Method

In order to solve the Navier-Stokes equations the numerical code has to discretize them prior to solving them along with the spatial domain.

Through the **Finite Volume Method**, the spatial domain is separated into small control volumes solving the discretized Navier-Stokes for each of them. For this matter the pressure-velocity coupling and the spatial need **discretization schemes** [38].

Star CCM+ provides flow models to address different fluid flow cases. Each employs different CFD solvers with mathematical solving algorithms. These are needed to compute the unknowns in the available governing equations. The available flow models are: the Viscous Flow Model, Segregated Flow Model and the Coupled Flow Model. The **Viscous Flow Model** is usually recommended for Non-Newtonian so it is not within the scope of this thesis. So only the Segregated and Couple Flow solvers will be further investigated.

When solving a fluid flow every velocity component appears each momentum equation and in the continuity equations intrinsically coupling all of the equations. There is no equation to solve for the pressure variable although it appears in both momentum equations.

3.4.1 Finite volume discretization

The general transport equation form for any scalar property ϕ, equation 3.27 is a second-order equation as can be seen by the diffusion term.

$$\underbrace{\frac{d\rho\phi}{dt}}_{\text{temporal derivative}} + \underbrace{\nabla.(\rho U\phi)}_{\text{convective term}} - \underbrace{\nabla.(\rho\Gamma_\rho\nabla\phi)}_{\text{diffusion term}} = \underbrace{S_\phi(\phi)}_{\text{source term}} \tag{3.27}$$

When integrated over a control volume V and after applying the Gauss's divergence theorem (A.1) the previous equation forms equation 3.28.

$$\underbrace{\frac{d}{dt}\int_V \rho\phi dV}_{\text{transient term}} + \underbrace{\int_A \rho v\phi \cdot da}_{\text{convective flux}} - \underbrace{\int_A \Gamma\nabla\phi da}_{\text{diffusion flux}} = \underbrace{\int_V S_\phi dV}_{\text{source term}} \tag{3.28}$$

Star CCM+ applies a set of surface and volume integration approximations to reach the final transport equation formulation. Both surface and volume integrals approximations were briefly described in appendix A in sections A.2.1 and A.5 respectively.

Applying the previous approximations yields the semi-discrete simplified transport

$$\frac{d}{dt}(V\rho\phi)_0 + \sum_f [\rho\phi v \cdot a]_f = \sum_f (\Gamma\nabla\phi \cdot a)_f + \left(S_\phi V\right)_0 \qquad (3.29)$$

In the Finite-Volume Method several schemes and methods have been developed to compute the variables and gradients. Numerical schemes have to be applied to the diffusion and convection fluxes.

3.4.2 Coupled Flow Solvers

The **Coupled Flow Model** is usually more robust than the **Segregated Flow model** when it comes to compressible flows and for heat transfer related cases such as high-Rayleigh number natural convection. It usually requires more memory [39] and it's calculation time has a linear relationship with the number of cells. It employs a Coupled Flow Solver which simultaneously solves the conservation equation for mass and momentum as a vector of equations. The formulation used is know for it's robustness for solving flows with dominant source terms, (eg. rotation).

3.4.3 Segregated Flow Model

The segregated flow model employs a segregated solver which solves the flow equations in segregated way meaning that it solves each of the momentum equations for each dimension in turn. The pressure-velocity coupling can be done by two algorithms in Star CCM+: SIMPLE or PISO. When trying to achieve steady state solution while PISO is recommend for transient cases where a smaller time-step and greater temporal accuracy is needed [39]. **SIMPLE**, or Semi-Implicit Method for Pressure-Linked Equations algorithm, described in [16], works as a guess-and-correct procedure approach to compute the pressure variable on a staggered grid arrangement. The **Segregated Flow Solver** is applied as it is suitable for low speeds and incompressible flow with a good compromise between accuracy and computation and convergence time [40].

3.5 Grid discretization

StarCCM+ offers a set of different volume meshers from which a choice between these should be done taking into account several aspects of the desired simulation such as the available computational memory, and time for mesh construction, aspired accuracy, convergence and geometry aspects such as how thin the geometry can be.

- Tetrahedral - tetrahedral core mesh cells;
- Polyhedral - arbitrary polyhedral core mesh cells;
- Trimmed - trimmed hexahedral core mesh cells;

- Thin Mesh - tetrahedral or polyhedral based prismatic thin mesh
- Advancing Layer Mesh - polyhedral core mesh, with in-built prismatic layers that advance inward from a polygonal surface mesh.

Also prism layer mesher can be included within the first three types which are presented in the following chapter. The three major available mesh types, as shown in figure 3.4, in what concerns the shape of the elements are: Tetrahedral, Polyhedral and Trimmed Meshes.

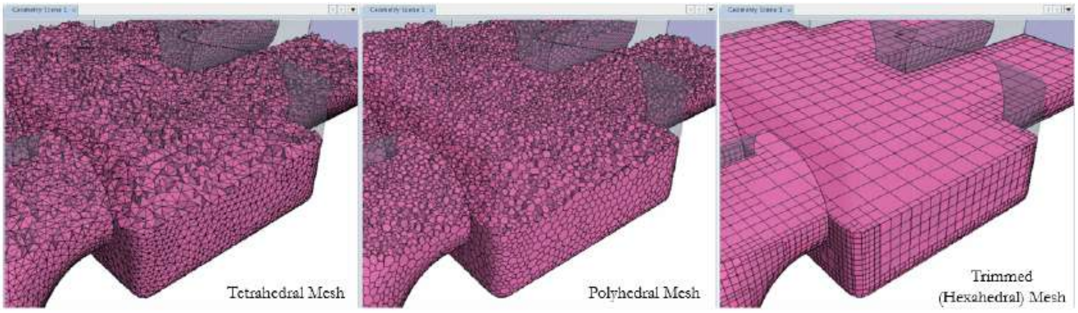

Figure 3.4: Different types of volume meshes.

While the tetrahedral mesher has a faster and lighter mesh generator, the polyhedral and trimmed meshers usually represent higher quality meshes and require less elements to achieve more accurate results. The Polyhedral mesh is the one chosen for the simulations done in this study as it provides a balanced solution for complex geometries and are easier to generate which could beneficial for a larger number of automatically changed geometry simulations which will be present in this study.

3.5.1 Prism Layer

To enhance the numerical modelling of a turbulent boundary layer prism or inflation layers are used where its purpose is to cover correctly the hole boundary layer thickness. The velocity profile near the wall changes very rapidly due to the viscous effects near a wall. Due to the linearly approximated values between cells' centers, the higher the gradients the thinner the elements the flow is nearer to the wall. For that reason prism layers or inflation layers are usually thin and long, as seen in figure **??**, also because there isn't a relevant change in the flow velocity magnitude in the flow direction.

The parameters to consider when designing the prism layers are:

- The number of prismatic layers;
- The growth ratio from the wall;
- The height of the first layer.

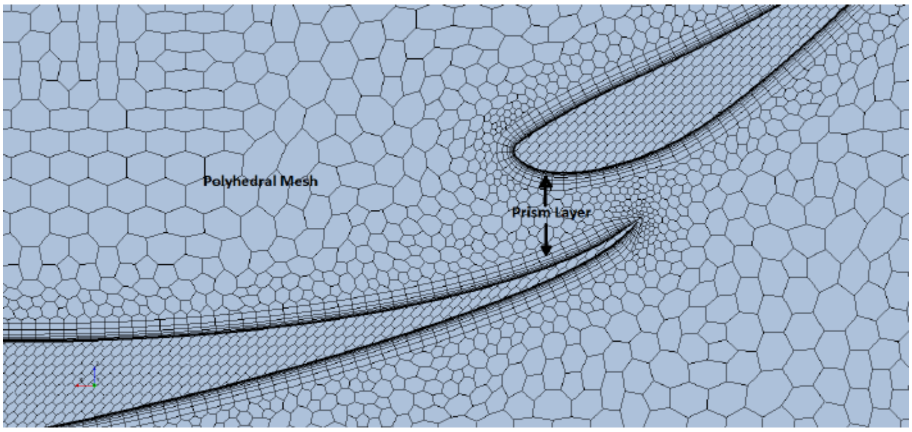

Figure 3.5: Rear wing section view where the prism layer to polyhedral mesh transition can be seen.

A choice has to be done around the desired y+.

Using specific turbulence models like the k- SST: If the first cell near to the surface is in the viscous sub-layer (y+ < 5) StarCCM+ will fully resolve the boundary layer by calculating the velocity value of every cell, if the first cell is in the log layer it will use the empirical assumption about the viscous sublayer- wall function, discussed in chapter 2.2.2.1.

3.6 Mesh Refinement and Convergence Study

3.6.1 Code Verification

Considering the described domain a mesh consisting of polyhedral elements was the first choice for the 2*D* simulations. Afterwards, the same mesh configuration was applied to the single airfoil case for bibliographic validation.

A starting assessment of the mesh numerical error was done, followed by a mesh refinement study.

3.6.2 Error and Uncertainty in Computational Fluid Dynamics

When debating the reliance of CFD modelling the terms *Error* and *Uncertainty* should be clarified.

An *Error* is a quantifiable CFD defectiveness that is not caused by the lack of knowledge. The common type of errors as in figure 3.6 are *User Errors* as a result of the inadequate use of software's, *Coding Errors* as mistakes within the software, and *Numerical Errors*. The later ones will be clarified up-next.

On the other hand the *Uncertainty* refers to defectiveness related to the insufficient knowingness. This could be related to the limited information and approximations of the geometric and physical properties of the case study, *Input uncertainty*, or to the physics'

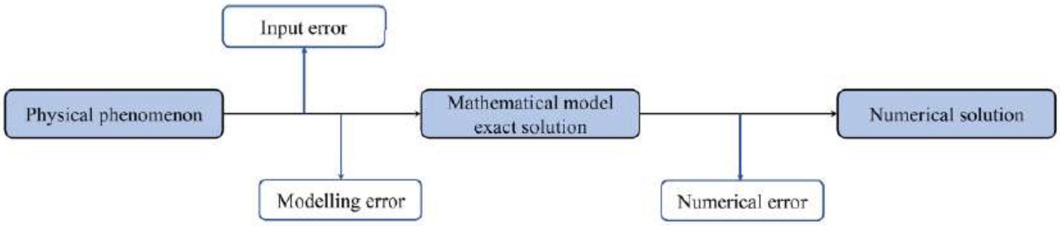

Figure 3.6: Types of simulation errors.

properties regarding the flow approximations such as the case modelling of turbulence, *Model Uncertainty* [16].

As the basis of CFD modelling relies on solving Partial Differential Equations (PDE)'s on a mesh type of discretization, numerical errors are induced in the following forms [41]:

- *Discretization errors* - Insufficient spatial and temporal discretization convergence or ;
- *Iterative convergence errors* - Insufficient convergence of an iterative procedure related to the truncation of the simulation after a specific number of iteration steps from which the solution is considered to be sufficiently close;
- Computer *Round-off* errors due to the finite number approximations of significant digits ;
- Computer programming errors.

A quantitatively assessment of numerical errors and uncertainties can be represented by equations 3.30 and 3.31 respectively [42]. As explained in [42] an Uncertainty U is an estimate of an error that 95% of the true value of δ is contained in the $\pm U$ interval.

$$\delta_{SN} = \delta_I + \delta_G + \delta_T + \delta_P = \delta I + \sum_{j=1}^{J} \delta_j \tag{3.30}$$

$$U_{SN}^2 = U_I^2 + U_d^2 + U_T^2 + U_P^2 = U_I^2 + \sum_{j=1}^{J} U_j^2 \tag{3.31}$$

In equations 3.30 and 3.31 the term δ_{SN} refers to the simulation numerical error while U_{SN} is the numerical uncertainty. Furthermore δ_I is the error associated with the number of iterations, δ_d discretization size, δ_T and other parameters δ_P. The same goes for the uncertainty indexes.

The concept of solution *Verification* illustrates the estimation of the previously decomposed numerical error and uncertainty contributions through iterative and parameter convergence [42]. This estimation is done through a set of convergence studies. In iterative and parameter convergence studies several parameter refinements in a *systematic* way

[41] are done to obtain solution which may present the following Monotonic convergence, oscillatory convergence or divergence.

3.6.3 Numerical Error Estimation

In the following study the numerical error should represent the biggest contribution to the results dispersion [43] from which the first usually prevails due to the discretization of the governing equations. Using unstructured meshes limits the order of accuracy of available discretization techniques. Two strategy are used to access the discretization error can be used that are then used to calculate an discretization uncertainty [44]:

- Estimation of an exact solution, order of convergence and discretization error through a spatial and temporal refinement study.
- Computing the error by an error transport equation applying a higher-order accuracy estimation.

Eça's and Hoekstra's procedure [44] works several grid refinement exercises to estimate the discretization uncertainty U_d through the calculation of the discretization error E_d. Calculation of the discretization error E_d is done by the truncated power series expansion [41],

$$E_d(\Phi) \equiv \Phi - \Phi_0 \approx \alpha_s \Delta h_i^{p_s} + \alpha_t \Delta t_i^{p_t} \tag{3.32}$$

where s and t represent spatial and temporal respectively, α the error constant and δh and δt the characteristic spatial and temporal grid resolution. Here p also represents the order of accuracy of the discretization scheme

The relation presented in 3.33 can be applied to an "exact"solution Φ_0 with 95% coverage.

$$\Phi - U_d(\Phi) \leq \Phi_0 \leq \Phi + U_d(\Phi) \tag{3.33}$$

The spatial and temporal refinement ratios are then introduced as in equation 3.34 as equal for simplicity where index 1 represents the finest grid resolution.

$$r_i \equiv \frac{\Delta t_1}{\Delta t_i} = \frac{\Delta h_i}{\Delta h_1} \tag{3.34}$$

The values of E_d, α and p should then be found by a least-squares means approach with a minimum of three solutions. Due to the complexity of the geometry and the difficulty of achieving certain procedure standards [45] the order of accuracy is assumed as $p = 2$ and the discretization error is computed as in equation 3.35 where i denotes the finest grid.

$$E_d(\Phi) = \Phi_i - \Phi_0 = \frac{\Phi_{i+1} - \phi_i}{r_{i+1}^p - 1} r_i^p \tag{3.35}$$

4

Preliminary Steady-State Simulations

The following chapter presents the preliminary simulations done in order to evaluate the 2D chosen airfoils and the FST10e rear wing configuration. The basic airfoil behaviour is analysed for the inverted S1223 airfoil comparing with experimental results and results estimated by the panel-method. Turbulence models are compared in the 2D case. Further more, a mesh is elaborated and analysed for the $3D$ cases preparing this mesh for the 3D iterative studies of the DRS configurations.

4.1 Introduction

Two separate cases of simulations were done for 2D and 3D situations. Initially two-dimensional simulations were done around a single profile to have an initial perspective of how the change in angle of attack α alters the wings' behaviour. The same set of simulations is done for different turbulence models in order to analyse it's impact in the results. Moving to the tri-dimensional simulations a first mesh refinement study was done to optimize the mesh applied to the tri-dimensional rear-wing. The same mesh criteria are left in such a way that it can be applied to a different wing case with experimental data.

The chosen 3D mesh is then applied to another wings' case for further comparison with the experimental wind-tunnel data in order to have a first perception of how accurate the rear wing results can be.

4.2 2D Airfoil Simulation

The purposes of the 2D simulations is to have a first perception of airfoil behaviour, is also to evaluate how the results will oscillate with the different types of turbulence and transition models. Results will be compared with the results calculated for the same Reynolds number of by the open-source software Javafoil which applies the panel-method. Results are also compared with experimental results from [46] which unfortunately are only available for a significantly lower $Re = 300,000$. Nevertheless it is possible to make some remarks on the forces rate of change along the different angles of attack and the overall behaviour. For this case, no direct comparison will be made due to the different Re. The experimental case was taken also because the panel-method is known for struggling with an accurate prediction of separation.

4.2.1 Selig S1223 Airfoil

In the specific FST10e rear wing case, the main wing and the flaps are made of an extrusion of the Selig S1223-il airfoil which is a recommended high-lift low Reynolds number airfoil. The S1223 airfoil is presented in figure 4.3 with streamlines and the velocity distribution around it which were generated by the open-source software *Javafoil* that uses the *panel method*[47]. The S1223 takes advantage of a concave pressure recovery and aft loading whose favorable properties are further explored in [48] and whose geometric properties are presented in table 4.1.

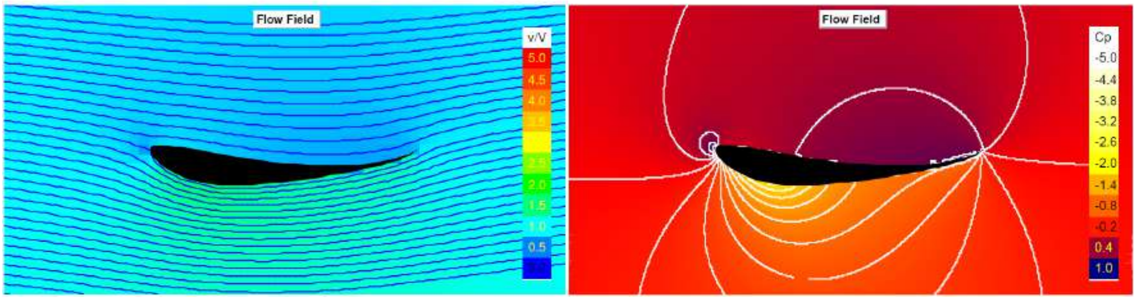

(a) Velocity distribution and streamlines.

(b) Cp distribution and iso Cp lines.

Figure 4.1: S1223 *JavaFoil* plots

Table 4.1: S1223 Airfoil geometric properties from UIUC Airfoil Database

(s1223-il) S1223	Selig S1223 high lift low Reynolds number airfoil
Max thickness	12.1% at 19.8% chord
Max camber	8.1% at 49% chord

4.2.2 Simulation Set-Up

Figure 4.2 shows the domain used for the two-dimensional simulations of the flow around the S1223 airfoil with a chord of $1m$. The domain has a height of $5m$ and a length of $20m$ where the leading edge of the airfoil sits at a distance of $6m$ from the inlet and a distance of $0.8m$ from the ground.

The unstructured mesh chosen is shown in figure 4.3 a). Prism layers are created with smooth dimensional transition into the unstructured mesh. Careful mesh refinement iterations and convergence analysis were conducted but were omitted for this first set

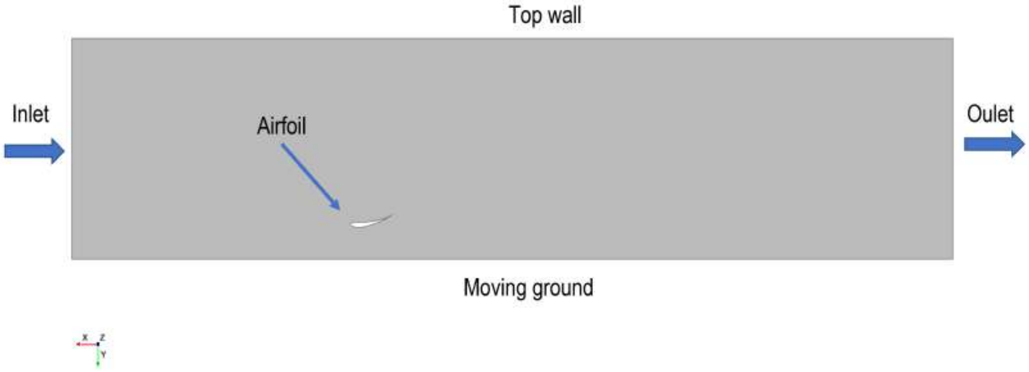

Figure 4.2: Two-dimensional domain for the S1223 airfoil.

of 2D simulations for simplicity. The result was a refined 68324 elements mesh. It was verified that the wall $y+$ remained below 5 near on the airfoils' surface.

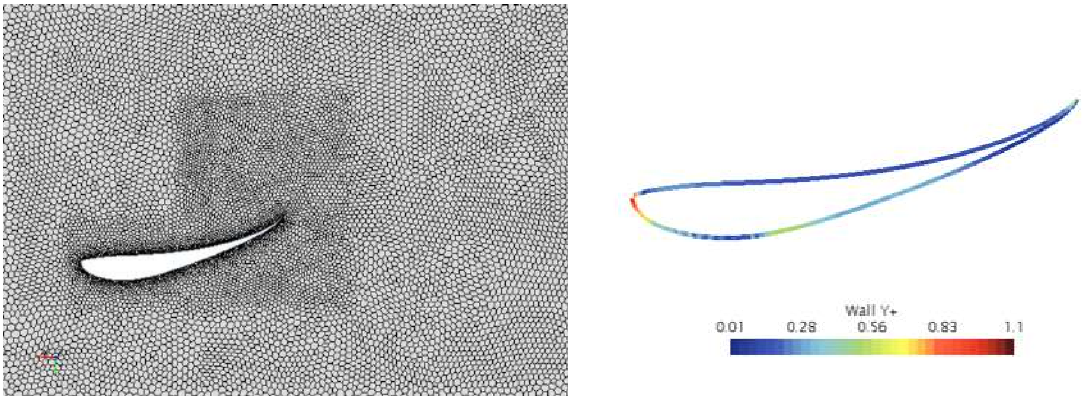

(a) Mesh closer to the airfoil with density boxes for wake refinement.

(b) Wall $y+$ along the airfoil surfaces.

Figure 4.3: Mesh and $y+$ around the airfoil.

The inlet velocity is $15m/s$ in the negative x direction of the coordinate system of figure 4.2 and the outlet as a pressure outlet with a reference $0Pa$. The ground is initially set as a moving ground with the same direction and magnitude of the inlet flow velocity. The airfoil wall is set as a wall with a no-slip condition and the top of the domain as a symmetry plane to have no impact in the flow on the rest of the domain.

The $\kappa - \epsilon$ and $\kappa - \omega\ SST$ models are tested individually. Afterwards the two discussed γ and $\gamma - Re_\theta$ transition models are coupled with the $\kappa - \omega\ SST$ model and compared. For each of the previous model simulations were done varying the angle of attack of the airfoil from -6° to 20° for comparison with literature results.

4.2.3 2D Turbulence And Transition Models Assessment

The plots in figures 4.4 and 4.5 show the lift and drag coefficients evolution along the different angles of attack for different cases. On one side it shows the different results from the CFD simulations for the different turbulence and transition models tested. On the other side the plots show the experimental results from [46] and the estimated results using the *JavaFoil* open-source software.

It should be noted that the *Re* for the current simulation is of about 10^6 while the results from [46] are obtained with a $Re = 300000$. The estimated *Re* is equivalent to the one used for the panel method calculation which isn't able to predict flow separation correctly.

From figures 4.4 and 4.5 it is seen that the angle of attack at which the maximum lift coefficient is better predicted by the $\kappa-\omega\ SST$ with the coupled transition models when compared with the panel-method results for the same Reynolds number. The angle at which the maximum lift coefficient happens in the experimental results is higher then panel method which is expected due to the lower *Re*. $k-epsilon$ seems to become unstable as it reaches higher lift coefficient closer to stall as it is know to perform poorly when predicting separated flows under adverse pressure gradients as according to literature [16] [34]. Plain $\kappa-\omega\ SST$ and $k-epsilon$ are excluded from the future simulations as they seem to under-predict the resultant forces. A very close behaviour is seen between the two set of simulations with the γ and $\gamma-Re_\theta$ transition models. The $\kappa-\omega\ SST$ turbulence model coupled with the γ transition model is chosen for the previous reason. It should be taken into account that the DRS simulations will required a large number of simulations and choosing this transition model will mean calculating half of the transition related equations reducing computational time.

As the values obtained for the $\kappa-\omega\ SST$ turbulence model coupled with the γ transition model are still some what higher then the ones calculated by the panel-method, another set of simulations were conducted to assess how much the ground effect played role in this discrepancy. Also the under-prediction of the aerodynamics under separated flows with the panel-method may also explain the slightly lower lift values. The plots in figures 4.6 and 4.7 show the lift and drag coefficients evolution along the different angles of attack for comparison cases (experimental and panel-method) and the $\kappa-\omega\ SST$ with the γ transition model with and with out a moving ground. For the latter the no-slip condition and boundary velocity were removed. It is shown that the results come closer to the results calculated by the panel method. From the previous set of simulation the decision was to proceed with the $\kappa-\omega\ SST$ turbulence model coupled with the *Gamma* Transition model for the next simulations. For future reference it should be noted at this point that the angle of attack that corresponds to the lowest drag coefficient for the chosen turbulence model is of 0° and through the panel method it is also estimated to enter the negative angle of attack values until about -3.

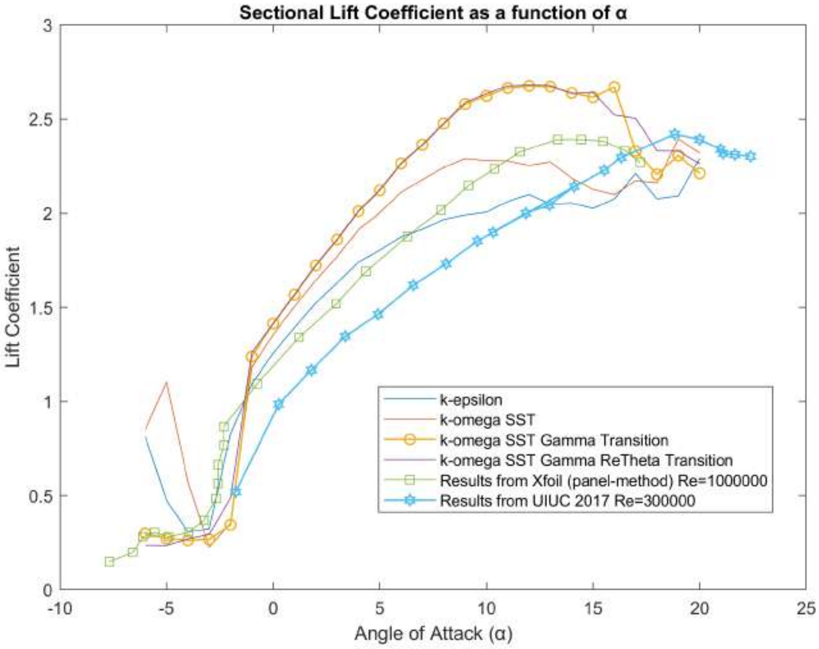

Figure 4.4: Lift coefficient results over different angles of attack for the different turbulence and transition models in comparison with experimental [46] and panel-method results.

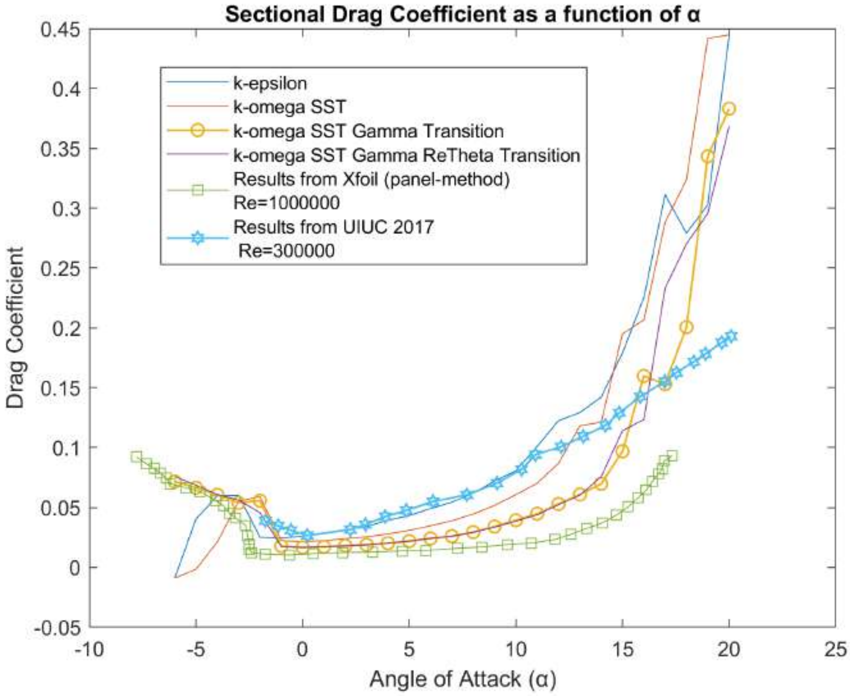

Figure 4.5: Drag coefficient results over different angles of attack for the different turbulence and transition models in comparison with experimental [46] and panel-method results.

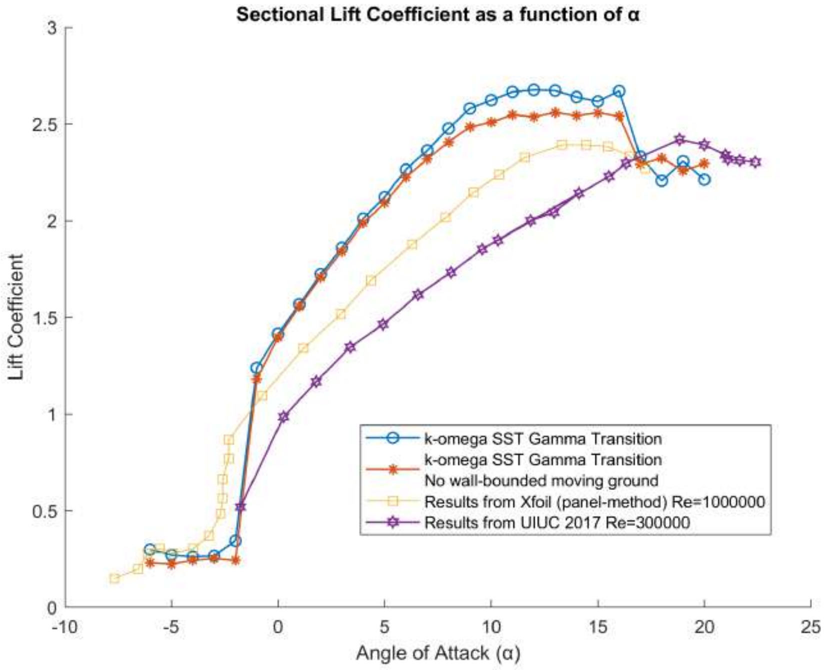

Figure 4.6: Lift coefficient results over different angles of attack for the$\kappa - \omega SST$ with the γ transition model with and without a moving ground no-slip boundary in comparison with experimental [46] and panel-method results.

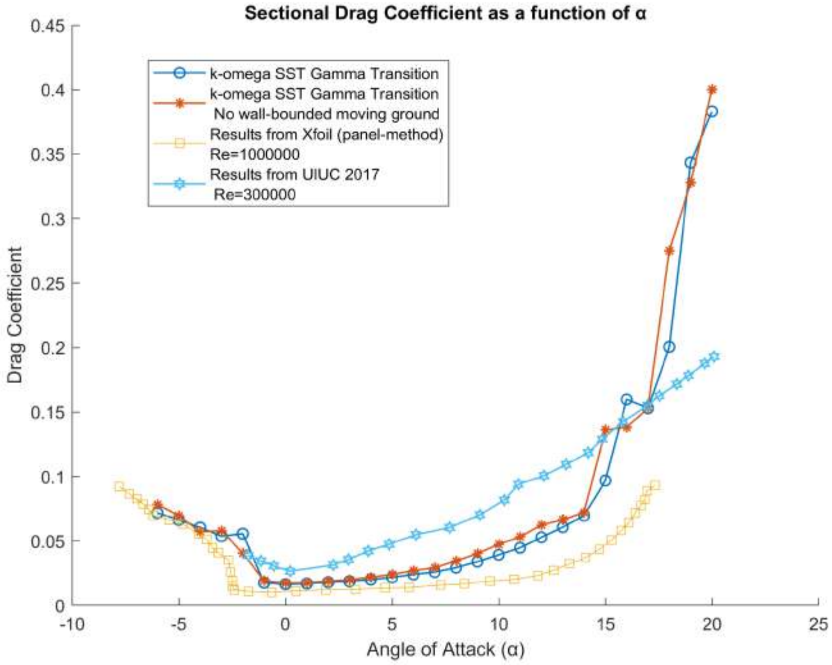

Figure 4.7: Drag coefficient results over different angles of attack for the different turbulence and transition models in comparison with experimental [46] and panel-method results.

4.2.4 Flow Analysis For 13° Angle Of Attack

For further analysis of the flow, the 13° angle of attack was chosen as reference to evaluate the flow behavior around the airfoils' surfaces. The choice is done based on the fact that this presented the biggest lift coefficient for the $\kappa - \omega\ SST$. In figures 4.8 and 4.9 the pressure distribution and the skin friction at the airfoil surfaces are seen. At the $x = 1.6m$ domain position on the airfoil suction side surface it it possible to see the formation of an adverse pressure gradient with a slight disturbance of the pressure coefficient and a peak of the skin friction. This indicates the presence of separation of the laminar boundary layer which is seen in figure 4.9. The flow then reattaches as a turbulent boundary layer with slightly increased skin friction forces witnessing the formation of the laminar transition bubble discussed in chapter 2.2.3. This phenomenon is shown in figure 4.10 where streamlines are seen partially flowing in the anti-stream-wise direction. These then turn stream-wise in a more downstream position indicating reattachment of the boundary layer.

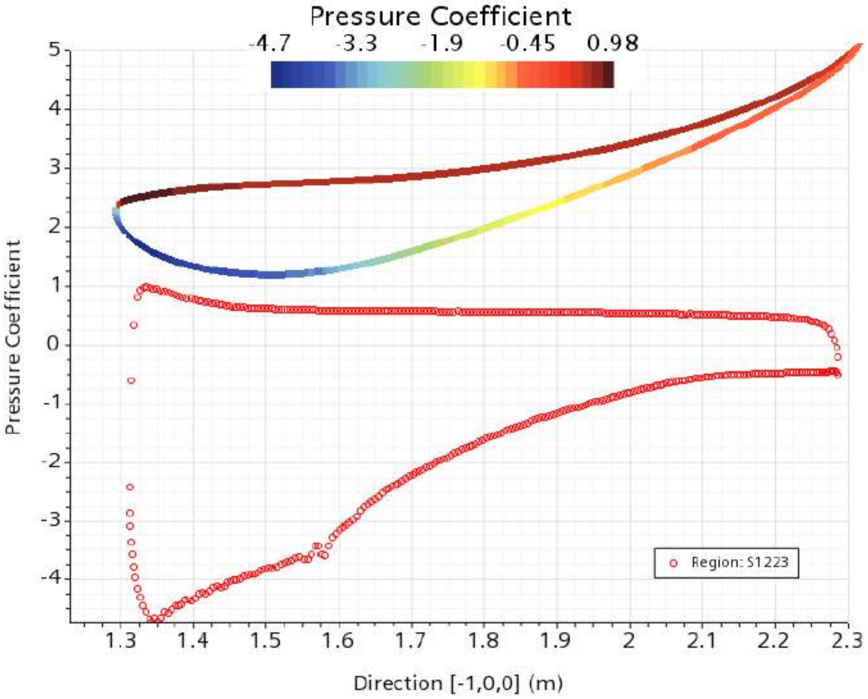

Figure 4.8: Pressure coefficient distribution around the airfoil surfaces using the γ transition model coupled with $\kappa - \omega SST$ turbulence model.

To assess the convergence of the solution over this airfoil one can look into the force coefficients convergence and at the normalized residuals in figures 4.11 a) and b).

It is seen that the forces stabilize at about 1100 iterations. Convergence is assumed to be achieved.

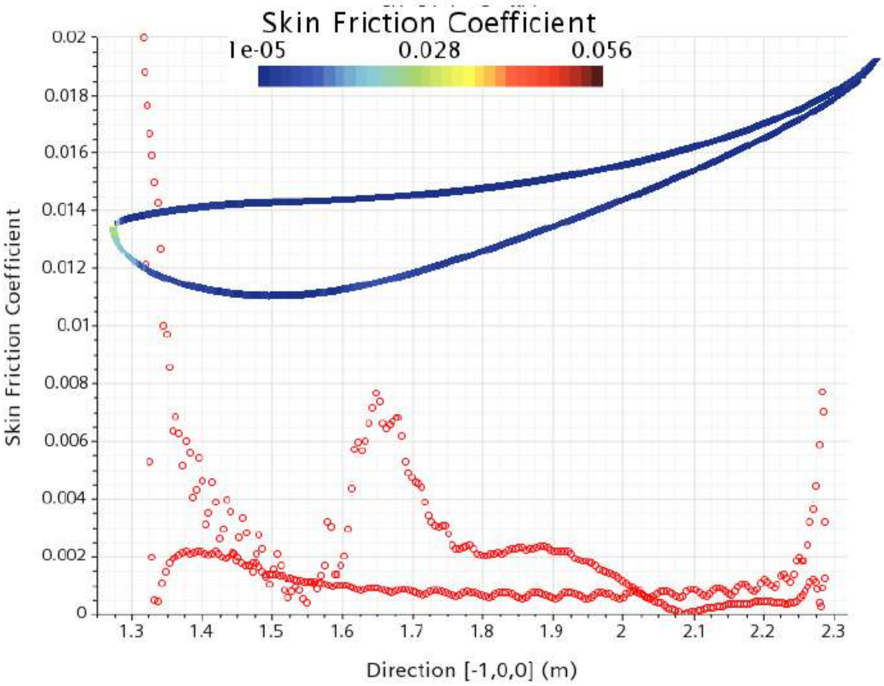

Figure 4.9: Skin friction coefficient distribution around the airfoil surfaces using the γ transition model coupled with $\kappa - \omega SST$ turbulence model.

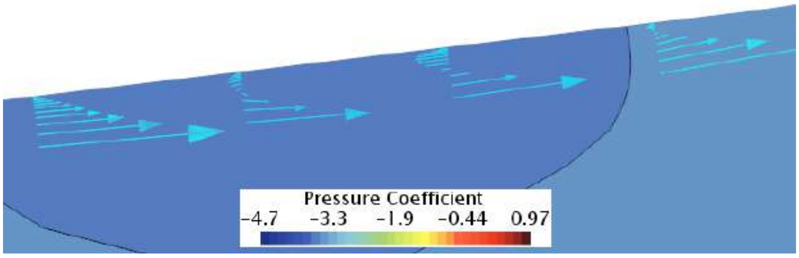

Figure 4.10: Closer view ath the pressure distribution and stream lines near the transition bubble.

4.3 FST 10e Simulations' Initial Setup

4.3.0.1 Geometry and Domain

It should be noted that due to flow symmetry around the rear wing a symmetry approach can be applied were only half of the wing is used defining its middle plane as a symmetric boundary.

For further reference the nomenclature in figure 4.12 was used where the constituents of the rear wing are the left and right endplates, the main element, the first and second flaps and a gurney flap at the trailing edge of the second flap. The main and first and second flaps have chord lengths of ?? = $400mm$, $c_{Flap1} = 200mm$ and $c_{Flap2} = 200mm$ respectively. This makes an approximate total chord length of $c_t = 800mm$.

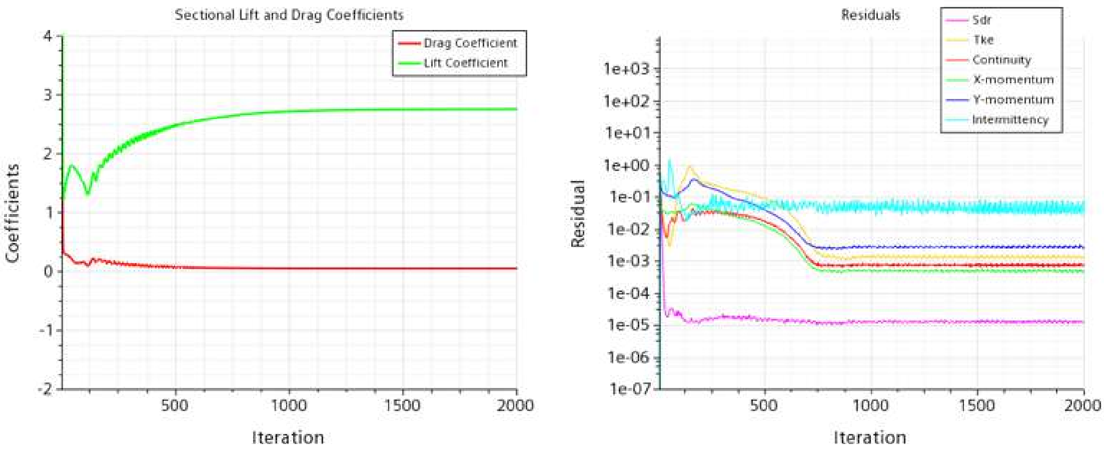

(a) Lift coefficient over 2000 iterations.

(b) Representative residuals over 2000 iterations.

Figure 4.11: Convergence analysis

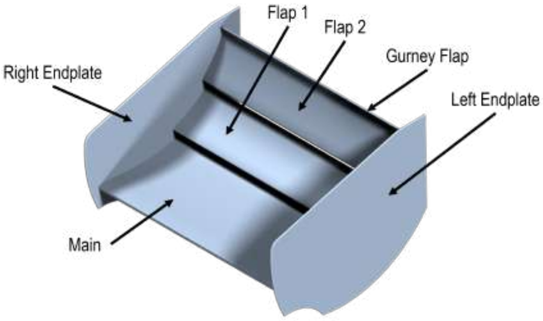

Figure 4.12: Rear wing components.

[27] used a 5 chord lengths in front, 8 chord lengths above, 10 chord lengths behind. For the initial tri-dimensional study of the rear wing a domain of 18m in length, 5m in height and 5m in width to ensure that it domain size wouldn't have an impact on the results. The domain dimensions used for the current study are presented in figure 4.13, which were considered to be big over-dimensioned in order to capture the correct flow structure without influencing it. The estimated average track velocity is 15 m/s, while 16.7 m/s was considered in [27] as well as a turbulence intensity of 1%.

4.3.0.2 Boundary Conditions

Having the previous aspects into account as well as the conditions introduced in the previous chapters, the boundary conditions applied can be summed into:

- Oulet defined as a pressure outlet with $0Pa$;
- Inlet as velocity inlet with $V_{inlet} = 15m/s$;

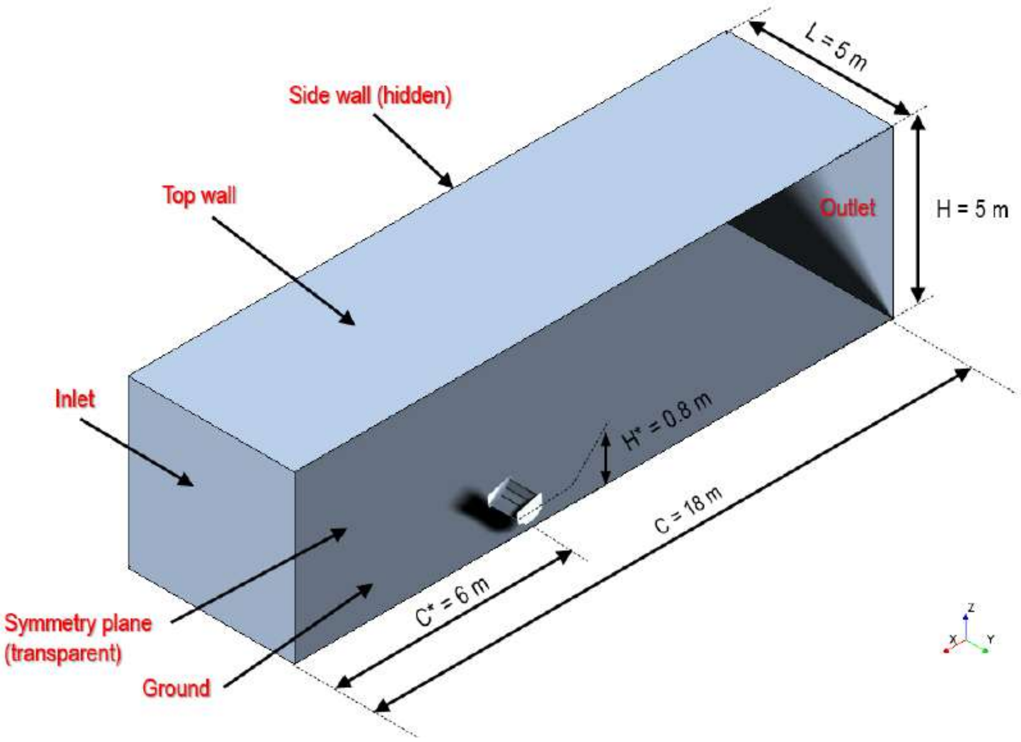

Figure 4.13: Domain dimensions in black and boundaries description in red. C* and H* refer to the distance of the leading edge of the main element to the inlet and to the ground respectively.

- Moving ground with $V_{ground} = 15 m/s$ in the flow direction and with the no-slip condition;
- No-slip condition at the rear wing surfaces $V_{wing} = 0 m/s$;
- Top and side walls defined as symmetry planes as they are considered to be far enough to have no relevant influence in the flow on the region of interest;
- Middle plane defined as symmetry plane.

4.4 Preliminary Mesh Development and Analysis

The first set of simulations were do in order to refine the mesh in order simulation results as accurate as possible with the available computational resources.

The mesh discretization evaluation and building approach was to apply the previously described methods to ensure a uniform refinement to allow enhanced quantification of the errors and/or uncertainties associated with the mesh. This section of the chapter will describe how the mesh was parameterized in such a way that the most uniform refinement could be applied as a function of a refinement rate variable Ri. Three different refinement types were done where in each a four different assessments of the mesh were done for Ri values between 1 and 2. For each refinement type, a cell size and density box refinements were done. The diagram in figure 4.14 sums up the mesh refinement study simulations. Finally the latter mesh parameter setup was chosen with a specific refinement rate Ri.

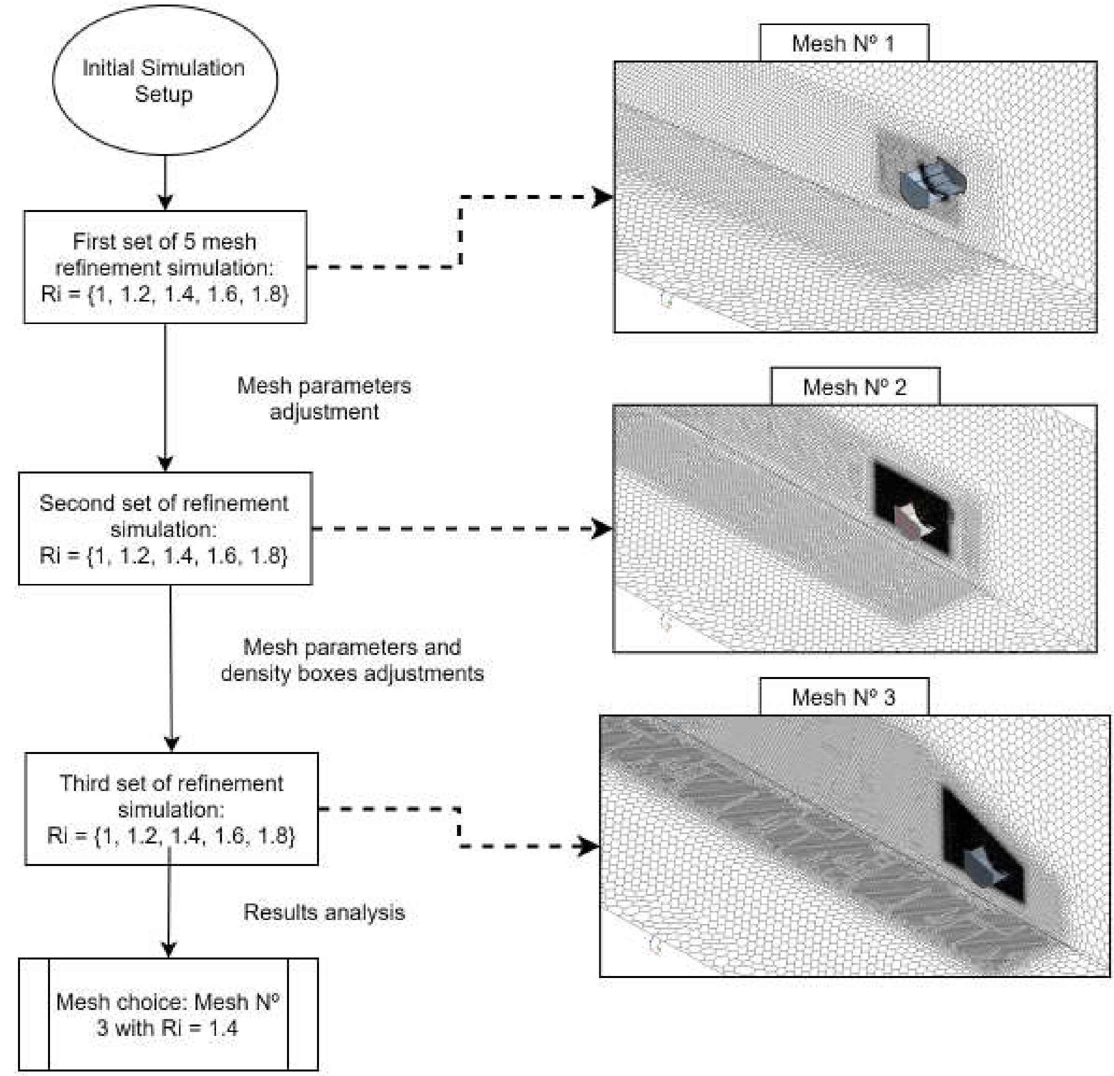

Figure 4.14: Mesh refinement scheme were the initial mesh (mesh 1) and the following mesh adjustments (mesh 2 and 3) are presented with a $Ri = 1$. As described each mesh has 5 refinement studies with $Ri = 1, 1.2, 1.4, 1.6, 1.8$.

4.4.1 Surface Wrapper and Imprint

Before proceeding to generate the mesh is it a good practice to use Star CCM+'s tool *Surface Wrapper* to improve the quality of the imported CAD's surfaces. This provides a closed, non-intersecting surface that allows an improved mesh generation by by-passing the usual complex geometry errors e.g. intersecting parts errors, surface mismatches, duplicate and internal surfaces. By applying initial element target sizing a first discretization can be done for each major group component. For instance, the Rear Wing group of part surfaces has a target size of 1.0mm being equal to the defined minimum target size. Likewise, the *Contact Prevention* feature is used to avoid close surfaces fusing into one another which is a recurring problem due to the mesh elements size relation to the distance between parts.

Also before meshing an *Imprint* operation is done which inscribes close surfaces and edges, within a defined tolerance of 0.1mm in the current case. A conformal surface mesh between parts is then created.

4.4.2 Mesh Refinement

After the surface preparation the mesh discretization is done applying controls to the overall domain. Specific mesh parameters are attributed to the main element, the flaps and endplate. Two density boxes are created to better capture the flow features as the rear wing wake.

4.4.2.1 Density Boxes

Two density boxes are created: one that extends from a little further than the rear wing to the back of the domain, the other mostly encompasses the rear wing and near wake development.

The density boxes geometries and parameters of each baseline mesh ($R_i = 1$) were adjusted from the second to the third mesh. The goal was to remove unnecessary refinement, sparing computational resources and better capturing certain parts of the flow.

4.4.2.2 Mesh Refinement Cases

An initial polyhedral coarse mesh was created where all the mesh parameters where defined as a function of a refinement rate variable *Ri*. This mesh corresponded to a *Ri* equal to 1. From this mesh a set o five simulations was done where the *Ri* value was increased by 0.2 in each following simulation, being the finest simulation correspondent to a *Ri* of 1.8. By taking this procedure a uniform mesh refinement is achieve for each of the three sets of mesh cases.

Due to the tri-dimensional properties of the mesh, the *Ri* parameter is introduced powered to one third ($Ri^{\frac{1}{3}}$) into a mesh parameter θ as in expression 4.1 or 4.2 if the point is to progressively increase is output or decrease it. For example, for the same mesh refinement the number of prism layers should increased proportionally to $R_i^{\frac{1}{3}}$ and the base size of the overall elements should decrease by multiplying a $\frac{1}{R_i^{\frac{1}{3}}}$. The value of c represents the baseline value of the parameter θ from each the refinement is done.

$$\theta = \frac{c}{R_i^{\frac{1}{3}}} \tag{4.1}$$

$$\theta = cR_i^{\frac{1}{3}} \tag{4.2}$$

The most relevant mesh parameters applied to the overall domain, density boxes, main, flaps and endplate are presented in table 4.2.

Table 4.2: Mesh control parameters.

	Default	**Wake Density Box**	**Wing Density Box**	**Wing**	**Endplate**
Base Size	$\frac{0.3}{Ri^{1/3}}$	$\frac{0.06}{Ri^{1/3}}$	$\frac{0.01}{Ri^{1/3}}$	Default	Default
Target Surface Size	Default	Default	Default	$\frac{0.008}{Ri^{1/3}}$	$\frac{0.01}{Ri^{1/3}}$
Minimum Surface Size	$\frac{0.001}{Ri^{1/3}}$	$\frac{0.001}{Ri^{1/3}}$	$\frac{0.001}{Ri^{1/3}}$	$\frac{0.001}{Ri^{1/3}}$	$\frac{0.001}{Ri^{1/3}}$
Surface Growth Rate	1.3	1.3	1.3	1.3	1.3
Volume Growth Rate	1.1	1.1	1.1	1.1	1.1
Number of Prism Layers	N/A	N/A	N/A	$12 * Ri^{\frac{1}{3}}$	$6 * Ri^{\frac{1}{3}}$
Prism Layer Near Wall Thickness	N/A	N/A	N/A	$\frac{0.00002}{Ri^{1/3}}$	$\frac{0.00002}{Ri^{1/3}}$
Prism Layer Total Thickness	N/A	N/A	N/A	6 mm	6 mm

4.4.3 Mesh Tests Analysis

From the three stages of mesh refinement studies the forces and force coefficients, number of iterations and stability were analysed. Tables 4.3, 4.4 and 4.5 present the number of elements and the previous evaluated parameters for the refinement rate on each mesh case. In respect to the overall results of the three mesh studies also the total average of the refinement results and the difference between the maximum and minimum results were taken. Stability was evaluated in terms of how the lift and drag varied along the the several iterations. In the following tables *Not Stable* refers to highly inconstant oscillations of the forces; *Semi Stable* refers to inconstant peak with periodic oscillations and *Stable* allows for constant and periodic oscillations. *Not Stable* and *Stable* lift coefficient cases are exemplified in figures 4.15 and 4.16.

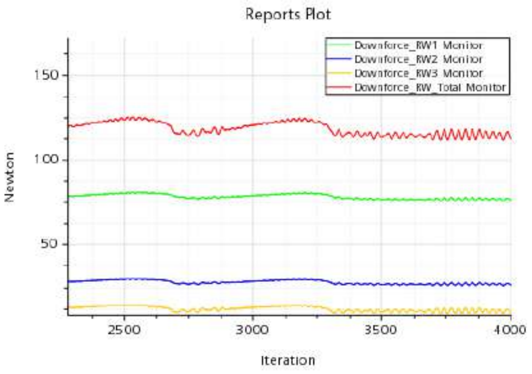

Figure 4.15: Lift force convergence considered *Not stable*.

Figure 4.16: Lift force convergence considered *Stable*.

In general all of the simulations were left running until 4000 iterations and the forces and coefficients values represent an average of the last 100 iterations. By analysing figures 4.17 and 4.18 is is seen that the last mesh is understood as the ideal mesh base line as the results present more stability and agreement in all of the refinement rates. Solution stability actually seems to decrease from the first to the second mesh as the cell size starting point is refined. Nevertheless the results are closer to the third ideal mesh.

Table 4.3: 1st mesh results.

Rear wing - 1st **Mesh**							
Nº Elements	Refinement rate	CL	CD	L (N)	D (N)	Iterations	Stability
1539365	1	1.62914	0.63655	112.2579	43.8623	4000	Semi stable
1712185	1.2	1.588434	0.600823	109.453	41.40046	4000	Semi stable
1984603	1.4	1.581251	0.596702	108.9581	41.11652	4000	Semi stable
2184581	1.6	1.57459	0.594464	108.4991	40.96228	4000	Stable
2348680	1.8	1.568983	0.590225	108.1128	40.67019	4000	Semi stable
	Average	1.588479	0.603753	109.4562	41.60235		
	$\delta_{higher-smaller}$	0.060156	0.046325	4.145143	3.192108		

Table 4.4: 2nd mesh results.

Rear wing - 2nd **Mesh**							
Nº Elements	Refinement rate	CL	CD	L (N)	D (N)	Iterations	Stability
4950896	1	1.640305	0.641703	113.0273	44.21731	3200	Semi-Stable
5965110	1.2	1.659123	0.648071	114.324	44.65618	3900	Stable
6924847	1.4	1.791723	7.17E-01	1.23E+02	4.94E+01	4000	Not Stable
7864914	1.6	1.65E+00	6.46E-01	1.13E+02	4.45E+01	4000	Not Stable
8733194	1.8	1.653195	0.643349	113.9155	44.3308	4000	Stable
	Average	1.677994	0.659406	115.6243	45.43721		
	$\delta_{higher-smaller}$	0.151418	7.58E-02	1.04E+01	5.22E+00		

Table 4.5: 3rd mesh results.

Rear wing - 3$^{rd} Mesh$							
Nº Elements	Refinement rate	CL	CD	L	D	Iterations	Stability
4233484	1	1.66243	0.655179	114.5518	45.1459	4000	Semi-stable
4975069	1.2	1.678762	0.661465	115.6772	45.57905	4000	Stable
5657408	1.4	1.663739	0.656145	114.642	45.21252	4000	Stable
6377217	1.6	1.662692	0.657207	114.5699	45.28567	4000	Stable
7099360	1.8	1.662359	0.653412	114.5469	45.02416	4000	Stable
		1.665996	0.656682	114.7976	45.24946		
		0.016403	0.008053	1.130259	0.554885		

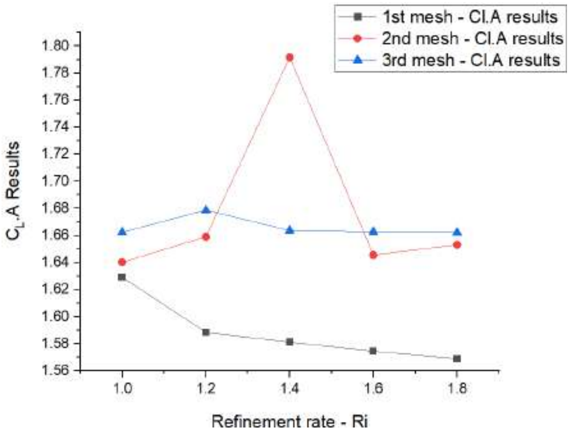

Figure 4.17: Graphic of the lift coefficient values for each mesh refinement study.

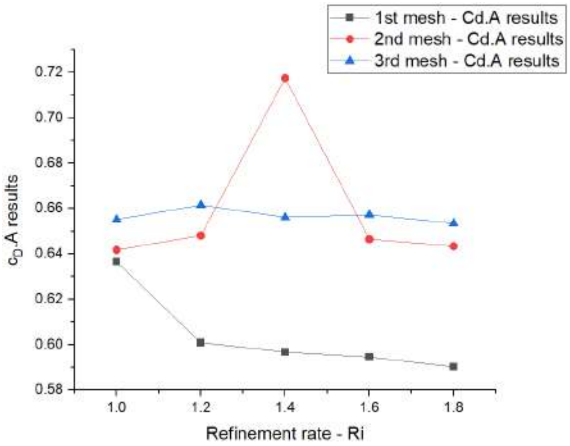

Figure 4.18: Graphic of the drag coefficient values for each mesh refinement study.

The graphic in figure 4.19 allows to understand how the average values of the refinement studies increase. The increase happens as the refinement from the 1st to 2nd mesh is done and stabilizes at the latter average value when final adjustments are done for the 3rd mesh. In figure 4.20 it is understood that result instabilities arise from the 1st to 2nd mesh as the difference between maximum and minimum values Δ increase. As result stability increase in the last mesh the Δ decreases giving extra confidence in the results from the 3rd mesh refinement tests.

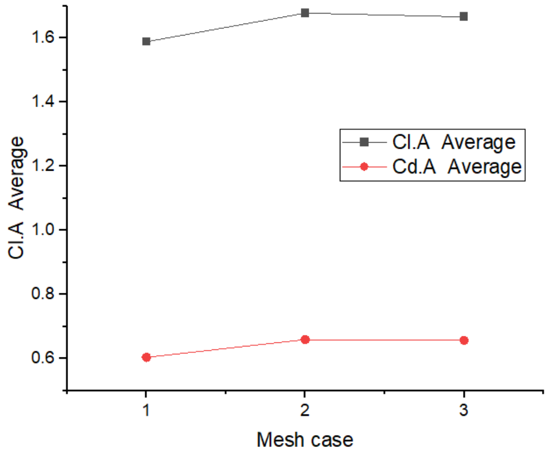

Figure 4.19: Graphic of the average lift and drag coefficients values for each mesh refinement study.

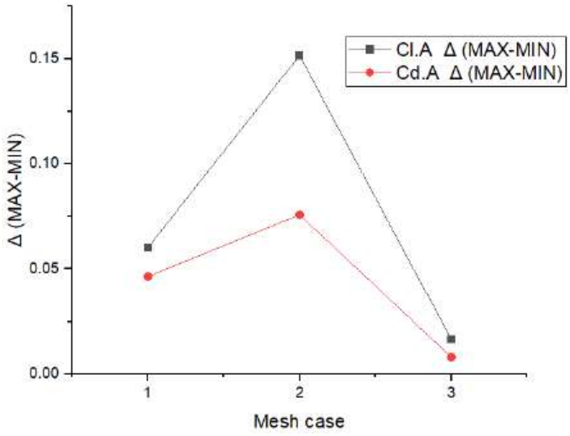

Figure 4.20: Graphic of the difference between the lift and drag coefficients' maximum and minimum values for each mesh refinement study.

The increase in oscillation was seen to coincide with the appearance of vortex shedding at the trailing edge of the last flap on the 2nd as seen in figure 4.22 while an attempt to average it is seen in figure 4.21 for the 1st mesh.

Effectively vortex shedding is expected to appear in this region so the latter results appear to be more precise and the forces assumed correct are the higher ones. Vortex

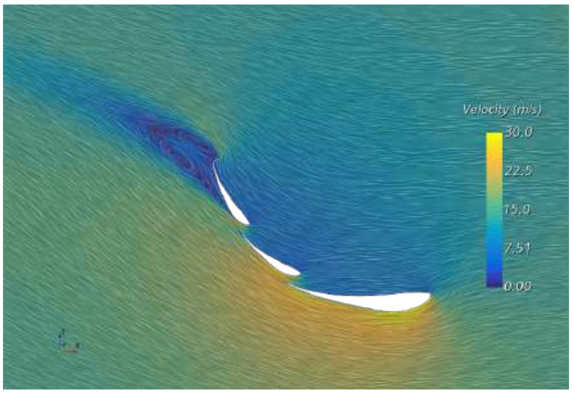

Figure 4.21: Averaged vortex shedding captured in the 1^{st} mesh set of simulations.

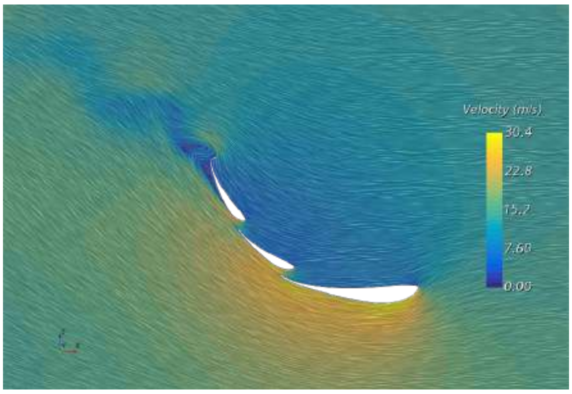

Figure 4.22: Transient vortex shedding captured in the 2^{nd} mesh set of simulations.

shedding is a transient phenomena which in such a scale can be difficult to average through the RANS turbulence models. The refinement of the mesh seems to explain the periodic oscillation in the results as every time there is an oscillatory release of a vortexes the forces acting on the wing will change.

The results' stability is worse in the 2^{nd} mesh refinement study when comparing to the 2^{nd} mesh cases so an adjustment of the density box is done where it expands further downstream and higher than previously in order to better capture the vortex shedding phenomena. The results appear to present the next oscillatory vortex shedding phenomena but in a more regular and cyclical way. Comparing again figures 4.21 and 4.22 it is seen that the averaging of the vortex shedding is represented as a bigger separation region explaining the lower values tendency of lift coefficient. Drag coefficient is also lower probably due to the decrease in *induced drag*.

4.4.4 Mesh Choice

The numerical errors where calculated based on the strategy that was suggested in chapter 3.6.3. It is verified that cases 1 and 3 decrease in numerical error as the refinement rate is done. After $R_i = 1.4$ there is achieved a minimum error so this refinement rate should be enough for the chosen mesh.

Due to the increased in stability and as it captures the flow structures better the 3^{rd} mesh cases are considered to be more precise. From these reasons the chosen mesh was the application of the refinement rate R_i of 1.4 to the 3^{rd} mesh as was considered to be refined enough to have no impact in the results. The numerical error of the chosen mesh is estimated to be of around 0.13% for the lift and drag coefficients. Evaluating figures 4.25 and 4.26 it can be seen that the overall y^+ is lower then 3 which means that it is in the viscous sublayer and can be correctly computed though a linear relation.

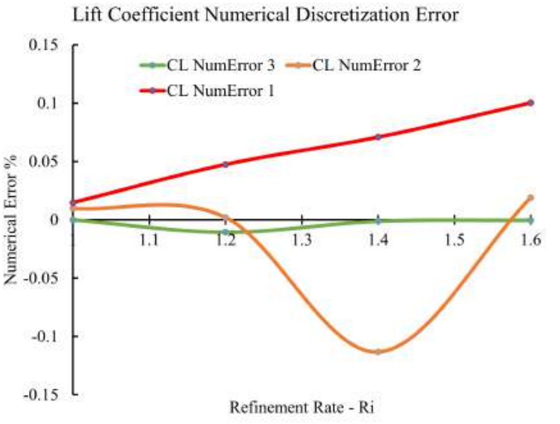

Figure 4.23: Numerical discretization error evolution for the Lift Coefficient of each refinement rate case.

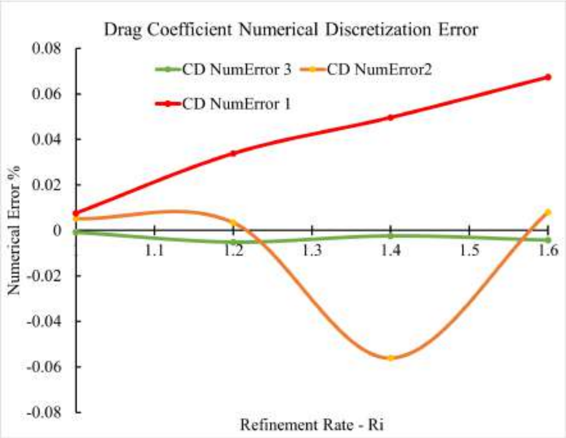

Figure 4.24: Numerical discretization error evolution for the Drag Coefficient of each refinement rate case.

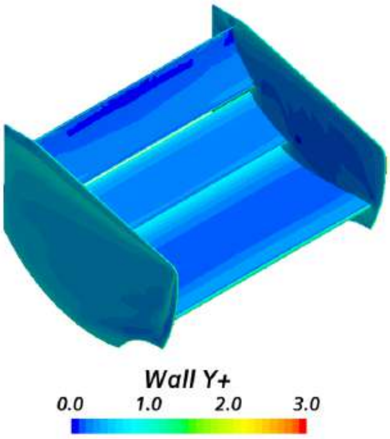

Figure 4.25: y^+ top view.

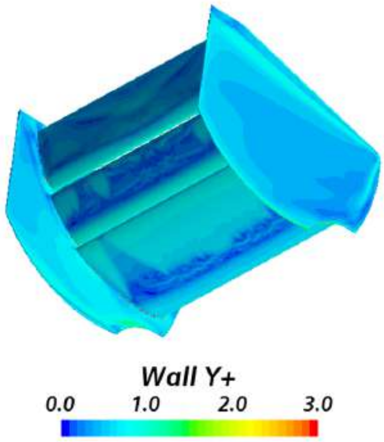

Figure 4.26: y^+ bottom view.

4.5 Rear Wing Baseline Simulation

A further analyses of how the simulations results should be done in terms of CFD modelling and physical results. The final results from the baseline simulation with the chosen mesh are:

- Rear Wing Downforce Coefficient: $C_L.A = 1.79$
- Rear Wing Drag Coefficient: $C_D.A = 0.73$
- Rear Wing Total Downforce: $L_{RW}.A = 247.70N$
- Main Downforce: $L_{Main}.A = 162.60N$
- Flap 1 Downforce: $L_{Flap1}.A = 58.32N$
- Flap 2 Downforce: $L_{Flap2}.A = 27.96N$

- Rear Wing Total Drag: $D_{RW}.A = 100.60N$
- Main Drag: $D_{Main}.A = 11.56N$
- Flap 1 Drag: $D_{Flap1}.A = 42.00$
- Flap 2 Drag: $D_{Flap2}.A = 46.00$

4.5.1 Pressure and Velocity Around the Rear Wing

The surface pressure coefficient around the wing is displayed in figures 4.27 and 4.28. The higher pressure on the pressure side and lower pressure on the suction side are visible and the pressure differential between the two surfaces justifies the negative lift force acting on the wing. By the bottom view one can associate the slight increase in pressure closer to the trailing edge of the second flap due to the residual flow separation and vortex shedding. The pressure distributions from figures 4.27 and 4.28 can be correlated with the velocity and contour from figures 4.29 and 4.30. It can be verified that the higher velocity is verified on the suction side where pressure decreases and the opposite on the pressure side.

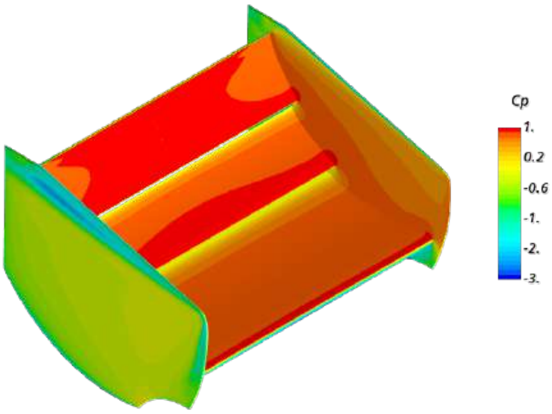

Figure 4.27: Top view of the pressure coefficient distribution on the rear wing.

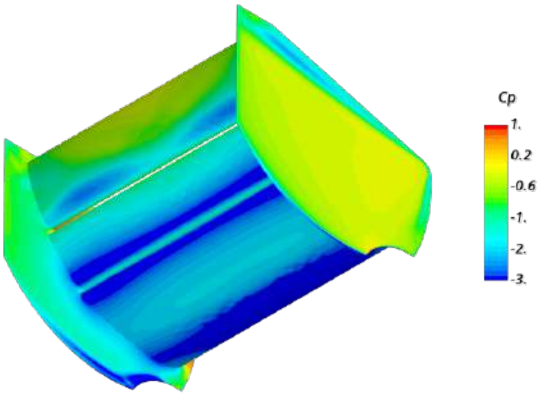

Figure 4.28: Bottom view of the pressure coefficient distribution on the rear wing.

4.5.2 Rear Wing Primary and Secondary Vortexes

The total pressure coefficient is used to evaluate flow energy changes and the Q-Criterion which helps visualize the rear wing wake and its swirling motion as wake convects downstream. The endplate primary and secondary vortexes can be identified in figures 4.31 and 4.32 by the swirling in an outward and inward direction respectively. Through the total pressure coefficient it should be noticed that the flow loses most of its momentum energy converting it into turbulent kinetic energy. Also the primary vortex seems to swirl in the flow stream direction and the secondary vortex moves inward and upward following the *downwash* (or in this case *upwash*) created in the suction side of the wing as the

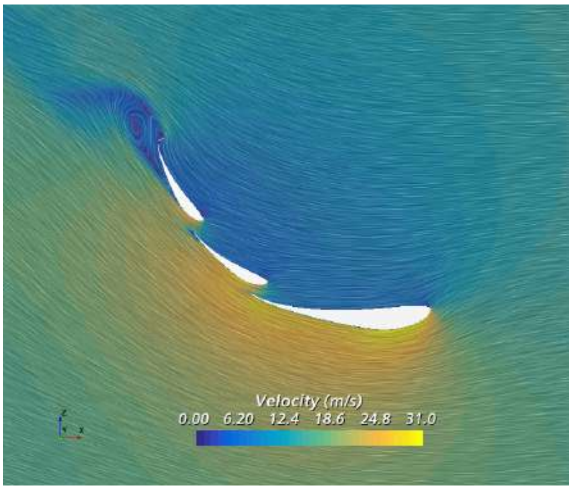

Figure 4.29: Velocity contours at the symmetry plane.

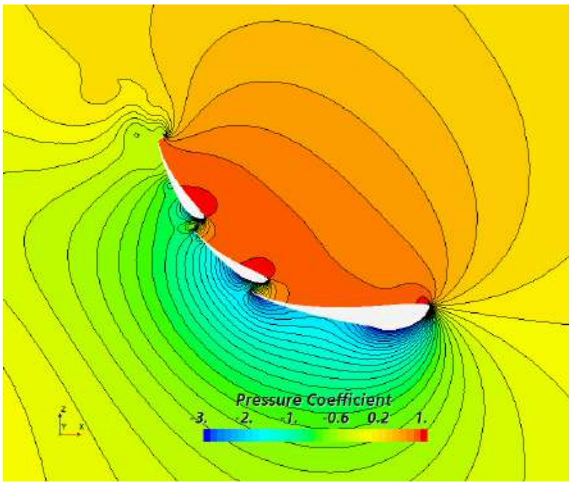

Figure 4.30: Pressure coefficient distribution in the symmetry plane.

flow direction gains a vertical component by keeping attached to the suction surface. It is expected that if the multi-element wing effect is broken by reducing the angles of attack of the rear flaps. The pressure differential should decrease hence the vortexes intensity should also decrease and the secondary vortex convect more in the free stream direction.

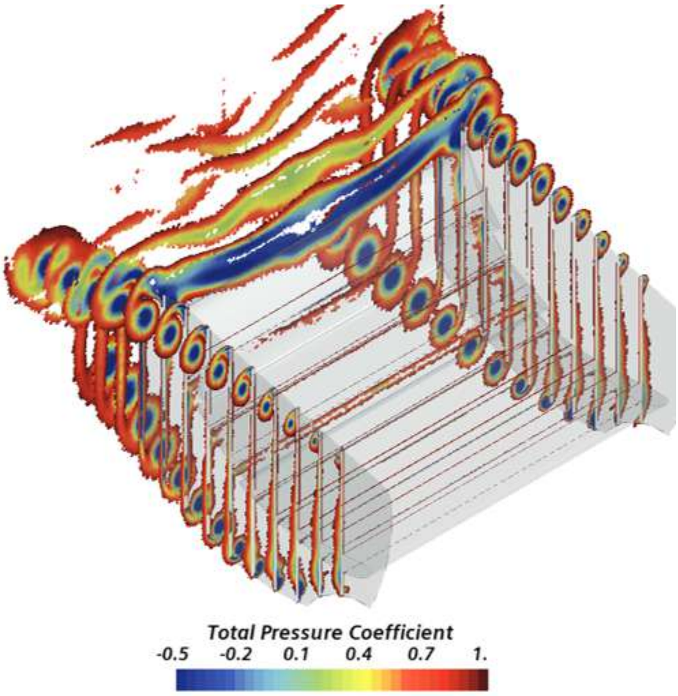

Figure 4.31: Section along the rear wing with total pressure coefficient plot

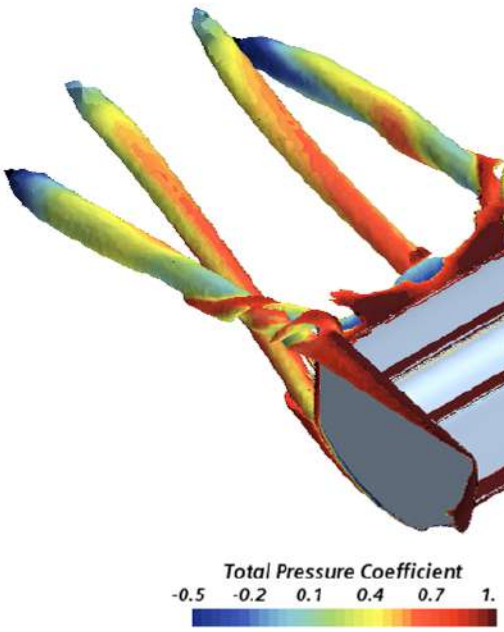

Figure 4.32: Q-criterion iso-surface with the total pressure coefficient representation.

4.6 GA(W)-type Wing in Ground Effect

Using the previously mesh, i.e. applying the same mesh parameters and setup, a preliminary study was done around a similar case to the one presented in [25]. In this paper an experimental wind-tunnel test is done around a tweaked GA(W)-type wing. CFD simulations were done varying the height of the wing in order to evaluate the ground effect on the force around the wing as a function of the height over chord - *h/c* as e. The tweaks done to the airfoil are not available so the simulations are done using the basic airfoil geometry presented in figure 4.33.

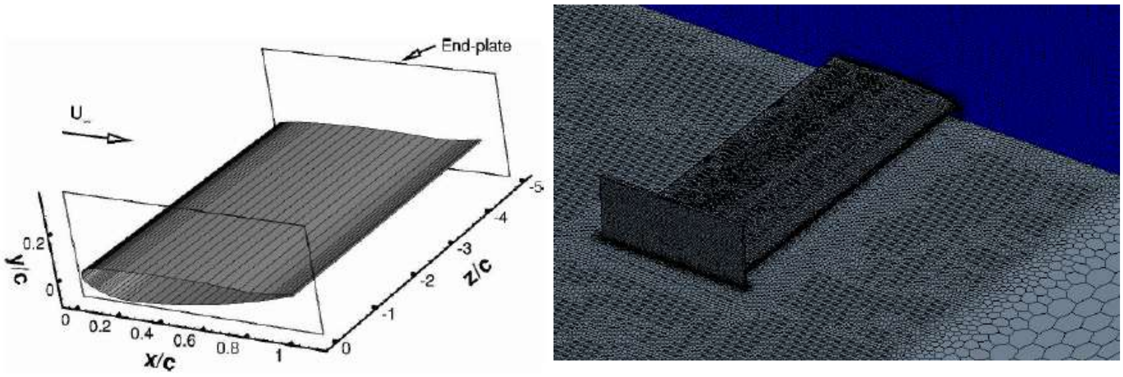

(a) Schematic of the GA(W) type wing and endplates.wing.

(b) Previous mesh parameters applied to the new

Figure 4.33: GA(W) simulations' geometry.

4.6.1 GA(W) Results

From figures 4.34 and 4.36 it is possible to see that in the stream-wise direction the velocity contours have the same behaviour by looking at the recirculation zone at the trailing edge of the wing. On the perpendicular direction it is possible to see that the CFD prediction of the endplate vortex is similar to the experimental results in location and vortex diameter.

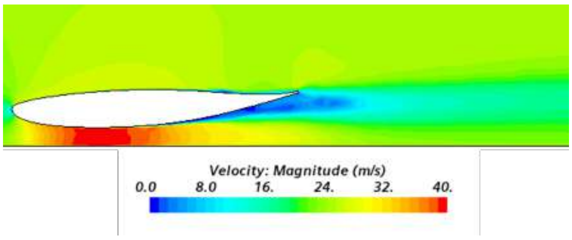

Figure 4.34: CFD velocity contours in the symmetry plane.

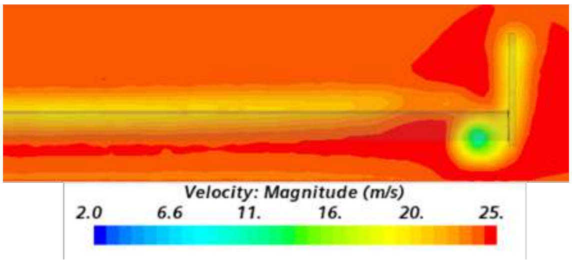

Figure 4.35: CFD velocity contours at $x/c = 1.5$.

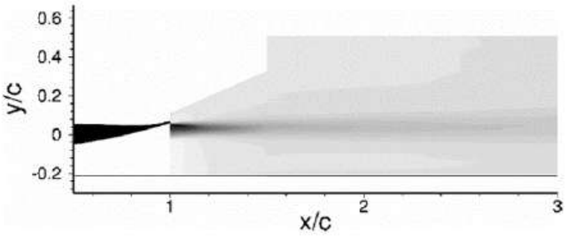

Figure 4.36: Experimental velocity contours in the symmetry plane.

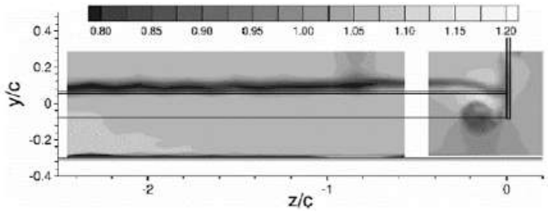

Figure 4.37: Experimental velocity contours at $x/c = 1.5$.

Also the several heights are tested in order to compare how the ground effect impacts the forces on the wing. Lift coefficient values from the executed CFD simulations are exposed against the *fixed-transition* (at 10% chord) experimental results on figure 4.38. Also free transition are given in [25] but only the fixed transition are presented as the latter are recommended for numerical model validation [25]. On the other side in figure 4.39 it is possible to verify that the rate of change of the lift coefficient is closer to the free transition experimental results as the changes in the CFD results are more abrupt in the crossing the stall region. An important phenomenon known as the ground effect is seen in this set of simulation as the lift coefficient drastically changes along with the decreasing height.

As the results are discrete the maximum error seen in the lift coefficient is calculated by extrapolation giving an maximum relative error of about 3.4% which is considered to be acceptable. From these results it is expected that the model can predict the aerodynamics forces acting on the FST10e rear wing and can then be used for an iterative DRS mapping of the flap angles and centers of rotation.

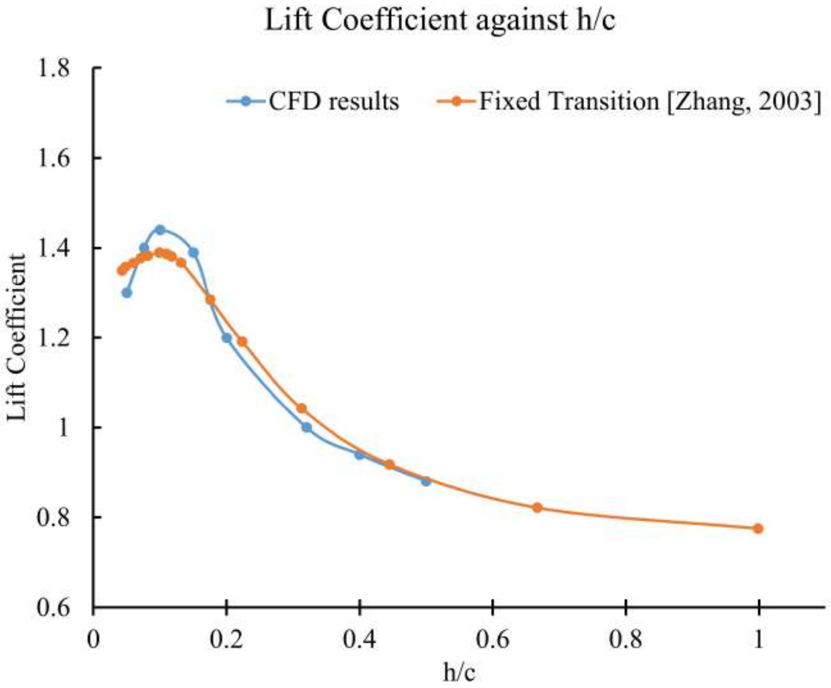

Figure 4.38: Evolution of the lift coefficient versus the height over chord (*h*/*c*).

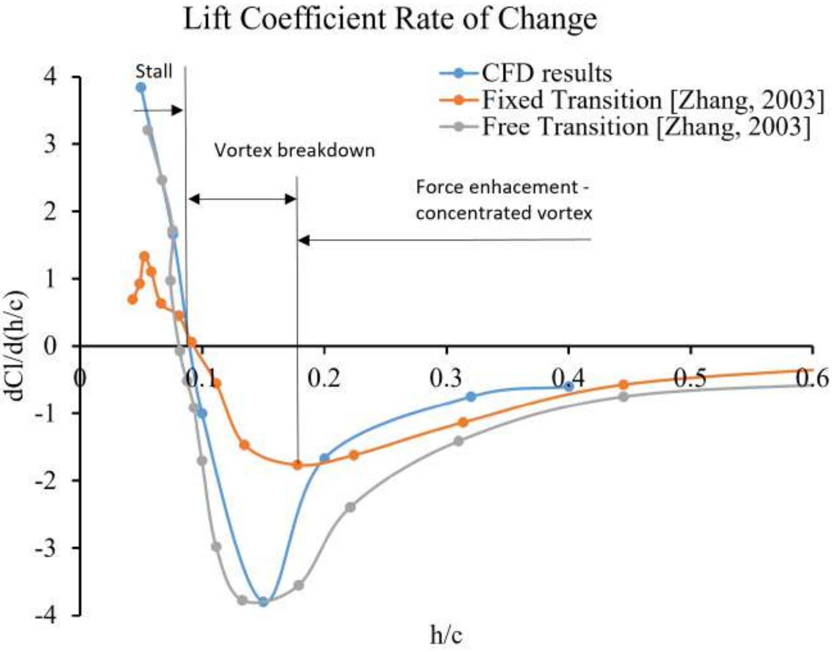

Figure 4.39: Evolution of the lift coefficient rate of change against the *h*/*c*.

5

DRS CONFIGURATION ANALYSIS

The 3D simulations began with mesh assessment studies where analysis of flow around the static wing on the baseline configuration was essential to have a better understanding of the flow behaviour. Different iterative studies are now conducted to assess the best DRS configuration, either for an actively controlled DRS or a more simple discrete system with just opened and closed position of the flaps.

Using *Javascript* macros it was possible to do iterative studies of the rear wing's configuration automatically by changing the geometry and meshing and carrying out all of the simulations with minor intervention in the mean time. The only inputs from the user should be the creation of the *Geometry*, *Simulations*, *Reports* and *Post-Processing* folders and fill the first folder with the respective rear wing Different flaps angles were simulated with an initial centre of rotation and were followed by an assessment of a centre of rotation that optimizes the DRS function.

5.1 Javascript Macros

Different macros were written to automatize the mapping of forces coefficients in order to obtain the best DRS configuration for every possible situation of cornering or straights. This will allow to extract forces for each configuration allowing an instant dependent calculation of the ideal force achieving the best compromise between downforce and drag for each specific cornering/straight situation.

Two different macro groups were elaborated. From the first macro, two studies were conducted. The goal of the first set of simulations was to obtain an overall mapping of the forces between most of the different angles configurations from initial angle of attack of both flaps to around 0 degrees. The second set of macros is similar to the first set but the angle step is refined and the range of angles is approximated to the lower drag configuration found with the first set. Finally the purpose of the the second macro was to analyse the optimum center of rotation for both flaps with a defined angle of attack.

5.1.1 Coefficients Mapping

Regarding the force mapping macro it applies an incremental study of the 1^{st} and 2^{nd} flap angles of attack (α_{flap1} and α_{flap2}) impact. The center of rotation is done around the middle point of the camber line. This middle point is obtained by the projection of the 50% of the chord line from the leading edge. Note that the center of rotation does not coincide with the aerodynamic center of the airfoils. It is expected that the optimum center of rotation lays closer to the trailing edge. The disturb flow from each flap should be further away from each other and have less interaction. For this purpose the center of rotation will be studied in the next stage. The macro used for this purpose is presented in I.1 and it was developed receiving the Initial angles of each flap for the study, the angle increment for each simulation And the and the final flub position. This miacro was applied to two types of mapping.

5.1.1.1 Overall Coefficient Mapping

In the first set of simulations the angles of the rear wing α_{flap1} and α_{flap2} were varied from the baseline configuration of the rear wing (30 and 55) to -4 and -3 respectively with an increment of -2. Therefore the overall mapping will take a total of 435 simulations to be ran.The number of simulations wouldn't be feasible without an automatic iterative set of simulation which justifies the creation of the macro with minor user interaction. Along the simulation the mesh should be regularly evaluated to ensure that the applied parameters create meshes with constant quality. The mesh applied is the one chosen on the previous chapter and should be monitored throughout the simulations

5.1.1.2 Refined Lowest Drag Configurations Mapping

The overall mapping macro was the first one elaborated after which a refined set of simulations was done to find the lowest drag configuration by changing the initial and final angles of attack of each flap with a angle step of 1. This macro focuses on the lowest drag configuration which can be applied into the discrete position DRS where the flaps positions changes only between the opened and closed positions.

5.1.2 Centre of Rotation Optimization

The second macro, in I.2, has the purpose of evaluating how assuming different angles of rotation influences the forces. A cycle couldn't be done due to programming language limitations on *StarCCM+* so each simulation needs to be written as a separate block. For this reason a *MATLAB* script was written in order to create a *txt* file that contained the desired number of blocks by copying a baseline block file and changing it's inputs.

Conclusions are mostly related to how the interaction between flaps influences the forces. For an angle of attack starting-point, all of the center of rotation simulations are done with a 0 angle of attack for both flaps. Then the center of rotation is varied along the camber line through fraction projections of the chord. In the current simulation they were varied by an offset of 20%. For the second flap the range of the centers of rotation is from 0% to 100% making a total of 6 positions and for the first flap they were varied from 20% to 100% making a total of 5 positions. In total there can be 30 configurations with all of the positions mentioned.

5.2 Drag Reduction System results

The two sets of simulations can be combined and repeated iteratively in order to refine to best DRS position regarding flap angles and centers of rotation. In this work only a first iteration will be applied of both types of macro. They were ran independently so at a first instance the optimal angles for minimum drag wasn't yet applied to the center of rotation set of simulation but should be in a second iteration.

For every set of simulations there will be a first mapping analysis through 3D plotting the coefficients against the flap configurations. Then a few specific cases will be taken to elaborate conclusions about the flow behaviour. This way correlating the forces mapping results with the flow behaviour should be possible.

5.2.1 Overall Coefficients Mapping

5.2.1.1 Mapping Results

For the average velocity $of 15 m/s$ the graphics presented in figures 5.1, 5.2 and 5.3 allow a general understanding of the forces distribution along the several configurations of the flaps' angle of attack with respect to the horizontal. In cooperation with the vehicle dynamics department, the previous should allow the development of an optimized control model that moves the flaps accordingly to the vehicle dynamics force needs at every instant. Correlations with the braking or acceleration and velocity instant values should be studied. The main drawback of correlating the CFD results for the previous purposes is that these results only stand for a constant 15 m/s velocity on a straight.

As expected, in a general perspective, the downforce and drag generated on the wing as a total will decrease as the angles of attack decrease.

Figures 5.1 and 5.2 allow to see the behaviour of lift and drag coefficient through the variation of the angle of attack.

The efficiency plot in figure 5.3 suggests that the second flap angle of attack α_{flap2} has the biggest contribution to the efficiency differences as the steepest slope is obtained by varying this angle as it possible to see an 300% increase in efficiency from around the initial angle of attack to close to zero degrees. The higher values of a C_L/C_D ratio are obtained for a lower α_{flap2}. Also for higher values of α_{flap2} it is seen that varying the first flap angle of attack α_{flap1}does not have a major impact in efficiency. The lower values of the α_{flap1} mostly start to matter below $\alpha_{flap2} = 30$ and have the biggest oscillation around $\alpha_{flap2} = 0$ for the range of α_{flap1} values.

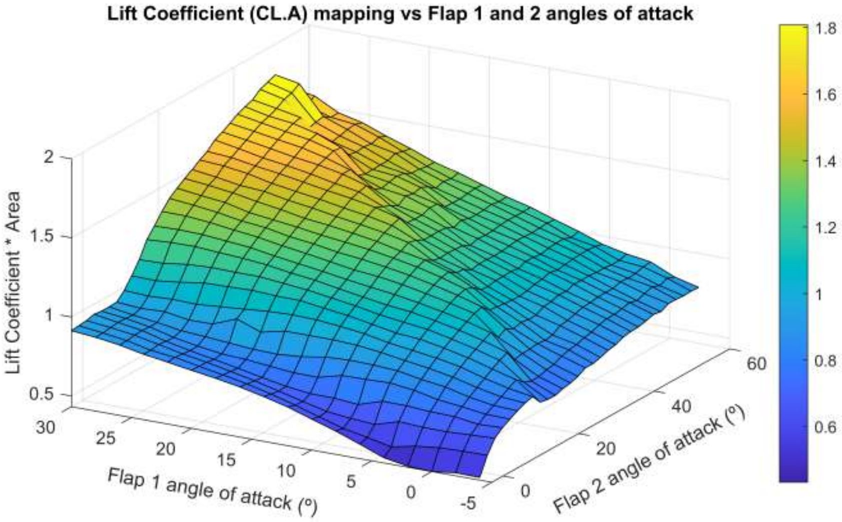

Figure 5.1: 3D plot of the lift coefficient C_L as a function of the angles of attack of the first and second flaps.

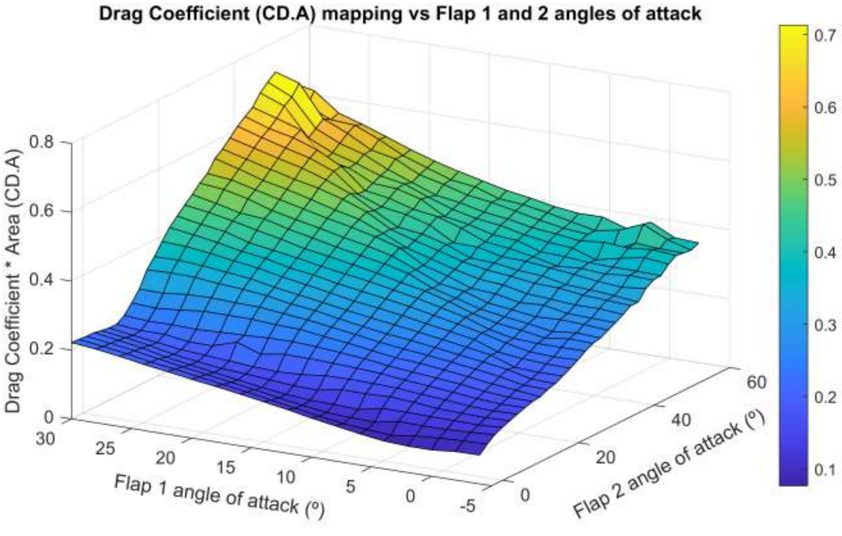

Figure 5.2: 3D plot of the drag coefficient C_D as a function of the angles of attack of the first and second flaps.

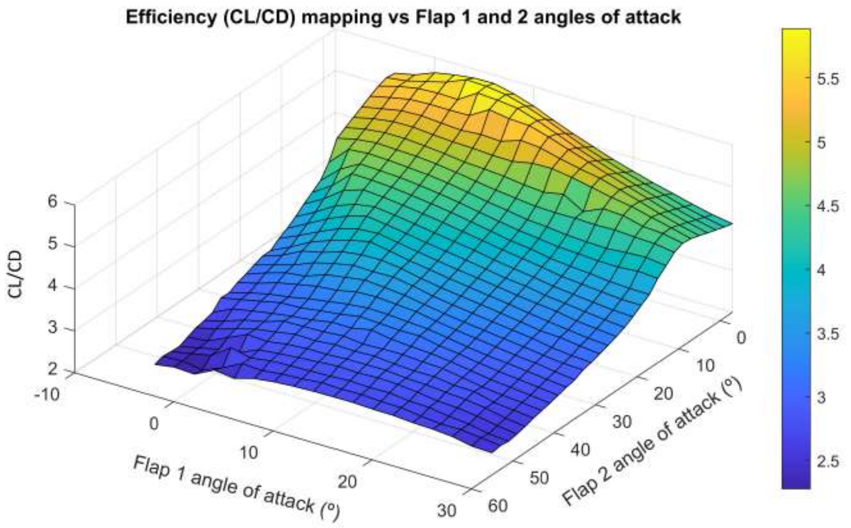

Figure 5.3: 3D plot of the efficiency C_L/C_D as a function of the angles of attack of the first and second flaps.

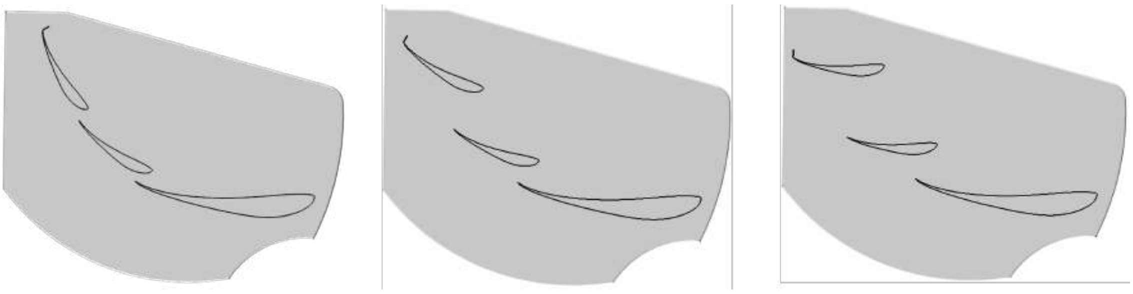

Figure 5.4: Cross section view of the geometry from the baseline configuration (on the left, a 50% rotated flaps configuration (in the middle) and the 0 configuration (on the right).

5.2.1.2 Flow Analysis

Not all of the values are presented for simplicity. Instead, alongside with the previous mapping plot, a few cases where chosen to deepen the flow analysis. At the middle plane of the baseline rear wing (unrotated flaps) it is possible to see the higher velocity and pressure differentials between the pressure and suction regions of the wing. Upwash is seen as expected and decreases intensity as the flaps are rotated. In this report a closer look is done at 2 cases: at the 0 angle of attack for both flaps and an intermediate case where the flaps 50% rotated.

The geometry of the three case can be seen in figures 5.4.

The pressure and velocity contours are then taken and presented in figures 5.5 and 5.6 with the same order from left to right. Comparing with the baseline results the lift and drag decrease up to 28% and 57% respectively while in the 0 configuration already decrease up to approximately 67% and 85%. It is possible to correlate the forces reduction with the decoupling of the multi-element wing effect where pressure drag decreases with the decrease of the pressure difference seen in figure 5.5. Note that the decrease in pressure is coincident with the decrease in flow velocity difference between the pressure and suction side as explained in the lift and drag theory chapter (chapter 2). Through the isolines in the pressure coefficient plot it is possible to see that the intermediate case still presents a coupling effect between the main element and the flap 1 but from that point on each flap works almost independently as the gap between the wing elements get bigger.

5.2.2 Refined Lowest Drag Configurations Mapping

5.2.2.1 Mapping Results

Tests with a smaller angle-step are presented in figures 5.7, 5.8 and 5.9. These results indicated that the lowest drag configuration converges into a configuration where α_{flap1} is 0° and a α_{flap2} is -6°. It must be stressed that the center of rotation for these tests are about the projection of 50% of the chord point into the camber-line. This means that for different centers of rotation the optimum results should be different. The lowest downforce configuration equals the lower drag configuration but the highest efficiency configuration is of a α_{flap1} of 2° and a α_{flap2} of -2°. Results show that tilting the second flap a additional 6 helps reduce the impact of the gurney flap reducing the drag component of the wing element.

The lowest drag configuration allows a drag reduction of up to 85% with respect to the baseline configuration and 15% with respect to the 0 configuration.

5.2.2.2 Flow Analysis

The velocity and pressure contours for the lowest drag configuration ($\alpha_{flap1} = 0$ and $\alpha_{flap2} = -6$) are shown in figures 5.10 and 5.11. It is seen that a lower impact of the gurney flap is seen down-stream after a recirculation region forms on the pressure side when comparing with the 0 configuration presented in the previous overall mapping analysis. The existent gurney flap tilts the lowest drag configuration of the second flap in -6. In figure 5.6 a slight up-wash was seen on the second flap due to the gurney flap which generated some extra lift and therefore more induced drag. With the well developed recirculation region on the top

One can note the reduction in skin friction through figures 5.12 and 5.13 that show the bottom view of half of the baseline rear wing and the lowest drag configuration ($\alpha_{flap1} = 0$ and $\alpha_{flap2} = -6$) respectively, which also indicates that part of the decrease in drag is also due to friction drag. The highly accentuated red regions in figure 5.12 on the bottom of the rear wing in a baseline configuration coincides with the increased up-wash generated but the multi-element wing configuration. Also the reduction in the size of the primary and secondary endplate vortexes contributes to the reduction of drag. The comparison between the baseline and the lowest drag configuration is seen in figure 5.14 were the

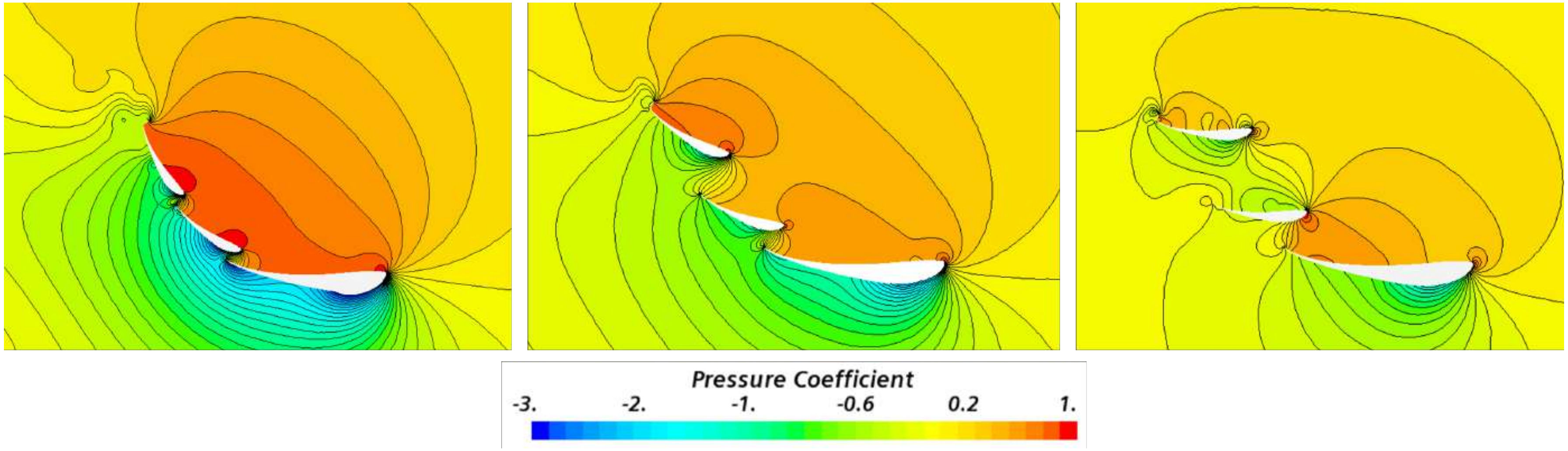

Figure 5.5: Midplane cross section view of the pressure coefficient distribution from the baseline configuration (on the left, a 50% rotated flaps configuration (in the middle) and the 0 configuration (on the right).

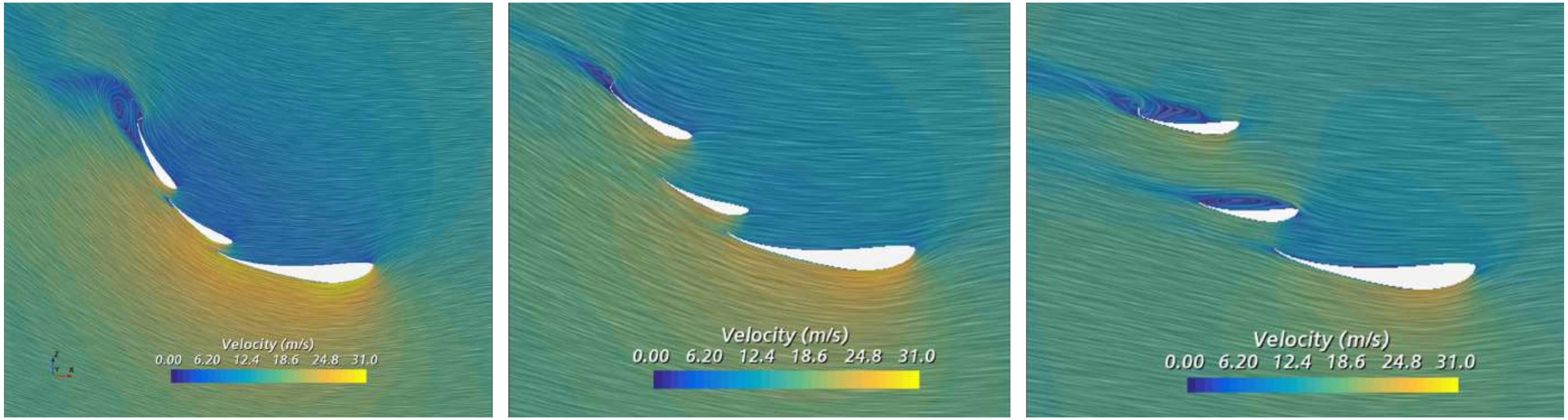

Figure 5.6: Midplane cross section view of the velocity contours from the baseline configuration (on the left, a 50% rotated flaps configuration (in the middle) and the 0 configuration (on the right).

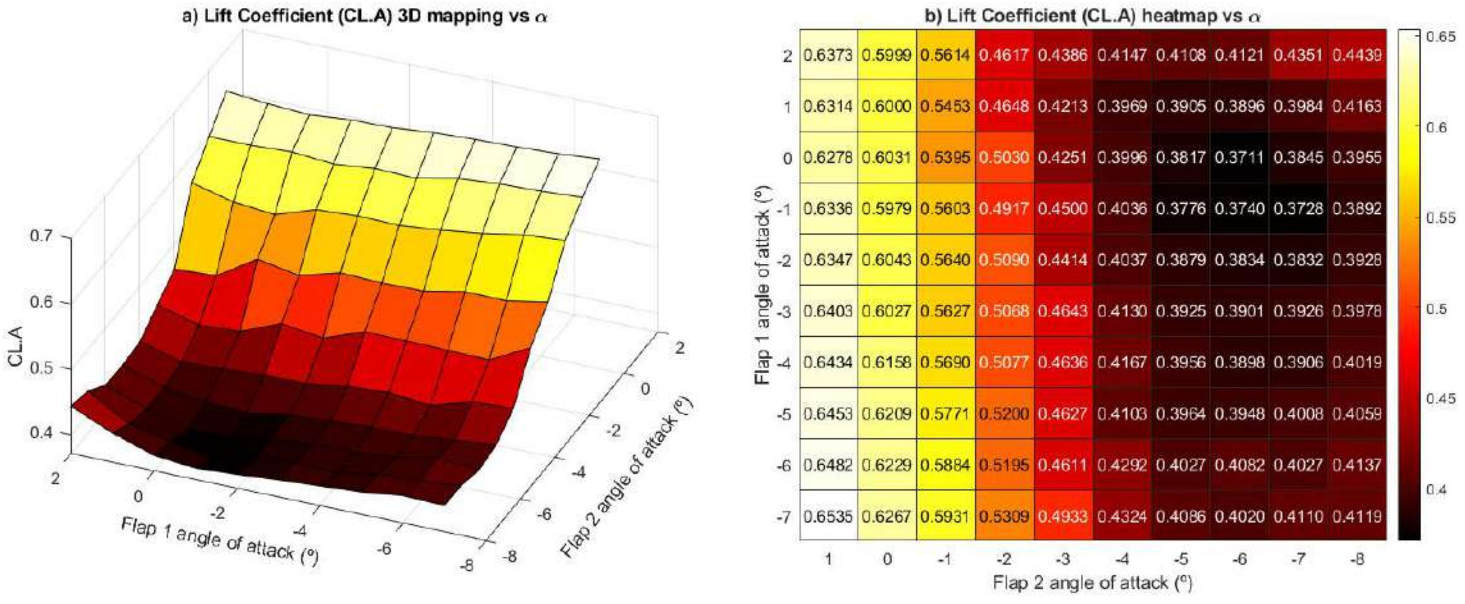

Flap 1 angle of attack (°) \ Flap 2 angle of attack (°)	1	0	-1	-2	-3	-4	-5	-6	-7	-8
2	0.6373	0.5999	0.5614	0.4617	0.4386	0.4147	0.4108	0.4121	0.4351	0.4439
1	0.6314	0.6000	0.5453	0.4648	0.4213	0.3969	0.3905	0.3896	0.3984	0.4163
0	0.6278	0.6031	0.5395	0.5030	0.4251	0.3996	0.3817	0.3711	0.3845	0.3955
-1	0.6336	0.5979	0.5603	0.4917	0.4500	0.4036	0.3776	0.3740	0.3728	0.3892
-2	0.6347	0.6043	0.5640	0.5090	0.4414	0.4037	0.3879	0.3834	0.3832	0.3928
-3	0.6403	0.6027	0.5627	0.5068	0.4643	0.4130	0.3925	0.3901	0.3926	0.3978
-4	0.6434	0.6158	0.5690	0.5077	0.4636	0.4167	0.3956	0.3898	0.3906	0.4019
-5	0.6453	0.6209	0.5771	0.5200	0.4627	0.4103	0.3964	0.3948	0.4008	0.4059
-6	0.6482	0.6229	0.5884	0.5195	0.4611	0.4292	0.4027	0.4082	0.4027	0.4137
-7	0.6535	0.6267	0.5931	0.5309	0.4933	0.4324	0.4086	0.4020	0.4110	0.4119

Figure 5.7: Refined 3D plot of the lift coefficient $C_L.A$ as a function of the angles of attack of the first and second flaps around the lowest C_DA configuration

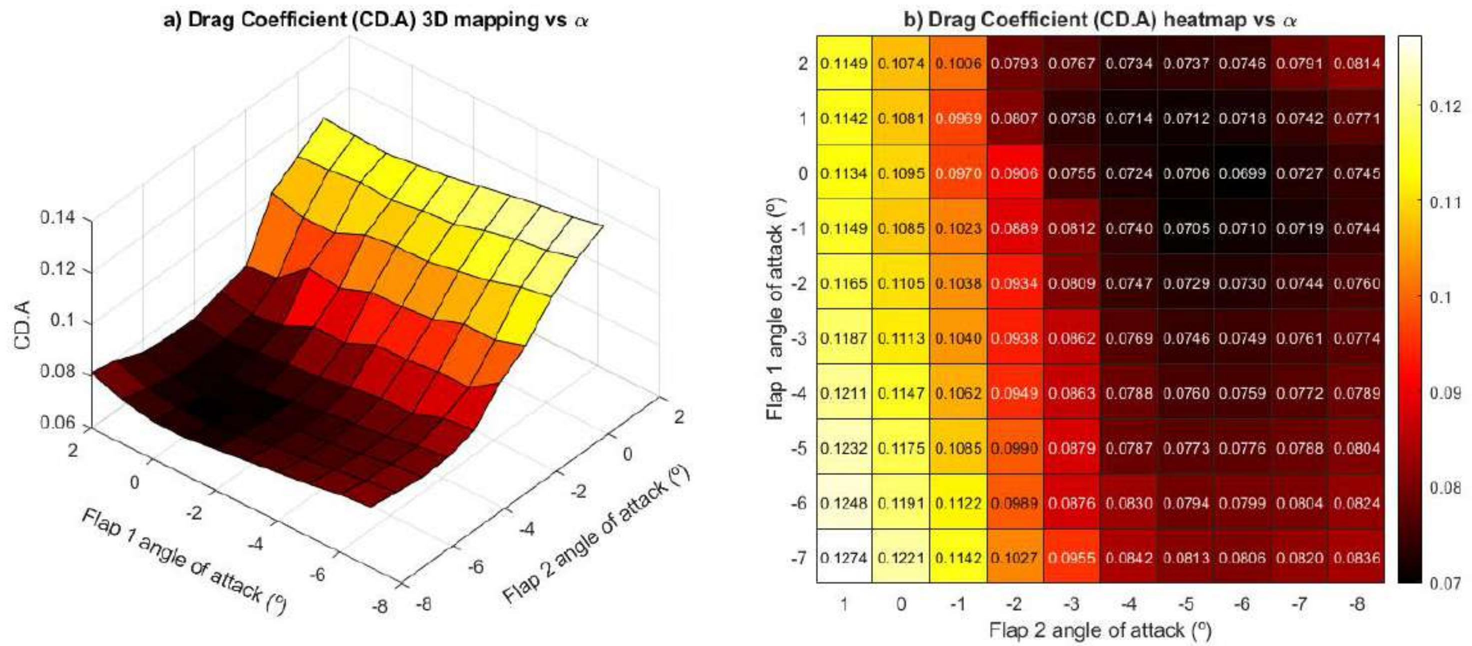

	1	0	-1	-2	-3	-4	-5	-6	-7	-8
2	0.1149	0.1074	0.1006	0.0793	0.0767	0.0734	0.0737	0.0746	0.0791	0.0814
1	0.1142	0.1081	0.0969	0.0807	0.0738	0.0714	0.0712	0.0718	0.0742	0.0771
0	0.1134	0.1095	0.0970	0.0906	0.0755	0.0724	0.0706	0.0699	0.0727	0.0745
-1	0.1149	0.1085	0.1023	0.0889	0.0812	0.0740	0.0705	0.0710	0.0719	0.0744
-2	0.1165	0.1105	0.1038	0.0934	0.0809	0.0747	0.0729	0.0730	0.0744	0.0760
-3	0.1187	0.1113	0.1040	0.0938	0.0862	0.0769	0.0746	0.0749	0.0761	0.0774
-4	0.1211	0.1147	0.1062	0.0949	0.0863	0.0788	0.0760	0.0759	0.0772	0.0789
-5	0.1232	0.1175	0.1085	0.0990	0.0879	0.0787	0.0773	0.0776	0.0788	0.0804
-6	0.1248	0.1191	0.1122	0.0989	0.0876	0.0830	0.0794	0.0799	0.0804	0.0824
-7	0.1274	0.1221	0.1142	0.1027	0.0955	0.0842	0.0813	0.0806	0.0820	0.0836

Figure 5.8: Refined 3D plot of the drag coefficient $C_D.A$ as a function of the angles of attack of the first and second flaps around the lowest C_DA configuration

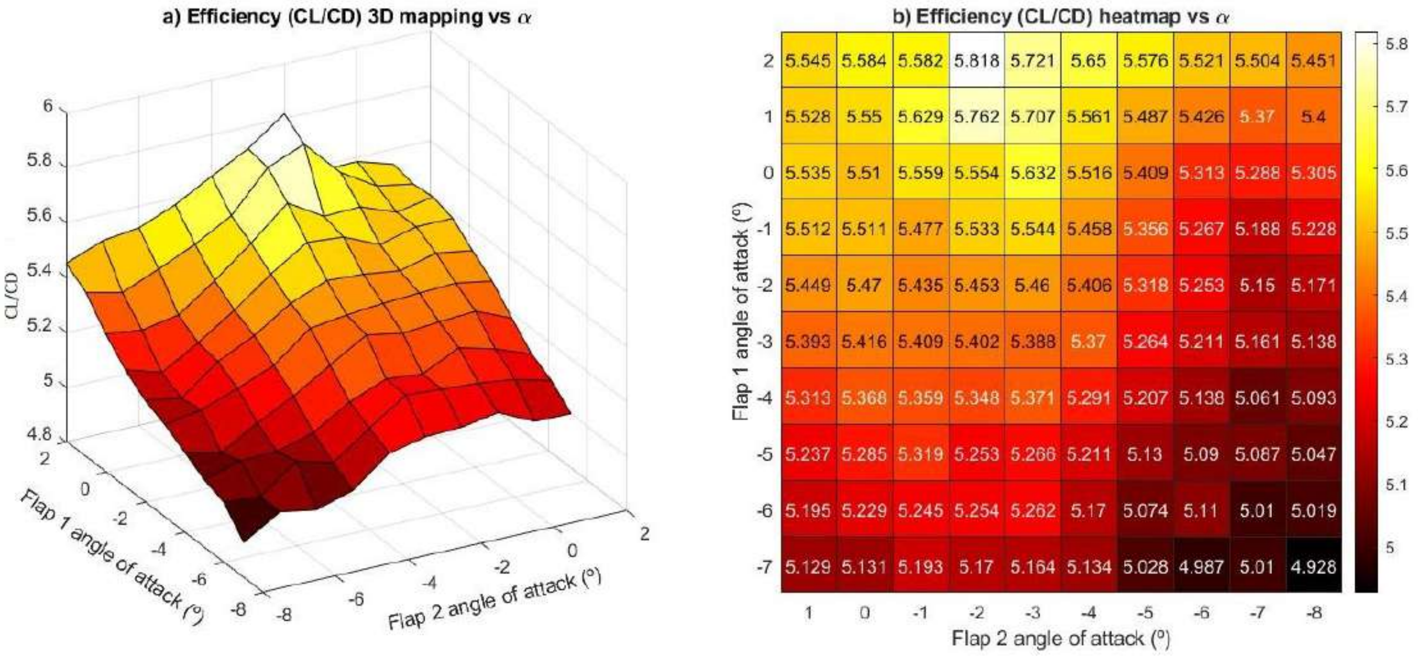
a) Efficiency (CL/CD) 3D mapping vs α

b) Efficiency (CL/CD) heatmap vs α

Flap 1 angle of attack (°) \ Flap 2 angle of attack (°)	1	0	-1	-2	-3	-4	-5	-6	-7	-8
2	5.545	5.584	5.582	5.818	5.721	5.65	5.576	5.521	5.504	5.451
1	5.528	5.55	5.629	5.762	5.707	5.561	5.487	5.426	5.37	5.4
0	5.535	5.51	5.559	5.554	5.632	5.516	5.409	5.313	5.288	5.305
-1	5.512	5.511	5.477	5.533	5.544	5.458	5.356	5.267	5.188	5.228
-2	5.449	5.47	5.435	5.453	5.46	5.406	5.318	5.253	5.15	5.171
-3	5.393	5.416	5.409	5.402	5.388	5.37	5.264	5.211	5.161	5.138
-4	5.313	5.368	5.359	5.348	5.371	5.291	5.207	5.138	5.061	5.093
-5	5.237	5.285	5.319	5.253	5.266	5.211	5.13	5.09	5.087	5.047
-6	5.195	5.229	5.245	5.254	5.262	5.17	5.074	5.11	5.01	5.019
-7	5.129	5.131	5.193	5.17	5.164	5.134	5.028	4.987	5.01	4.928

Figure 5.9: 3D plot of the efficiency C_L/C_D as a function of the angles of attack of the first and second flaps around the lowest C_DA configuration

total pressure coefficient on the endplate vortexes indicates that less flow momentum energy is loss to the endplate vorticity. They are still visible as the airfoils still create lift from the pressure difference on the pressure and suction sides.

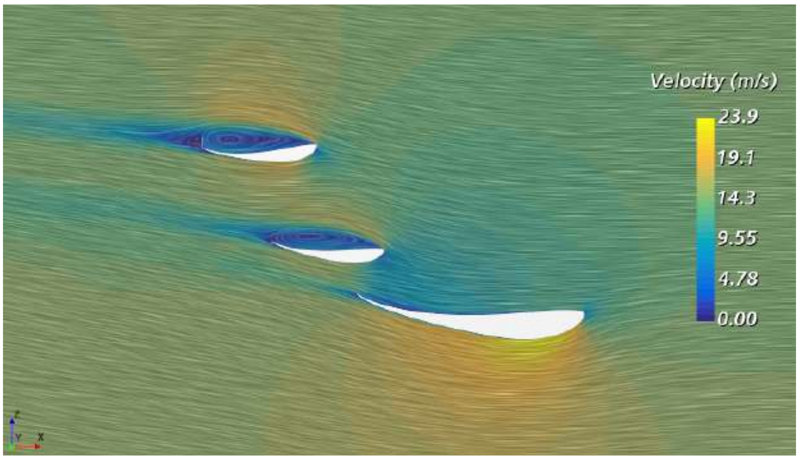

Figure 5.10: Velocity contours in the symmetry plane for $\alpha_{flap1} = 0$ and $\alpha_{flap2} = -6$

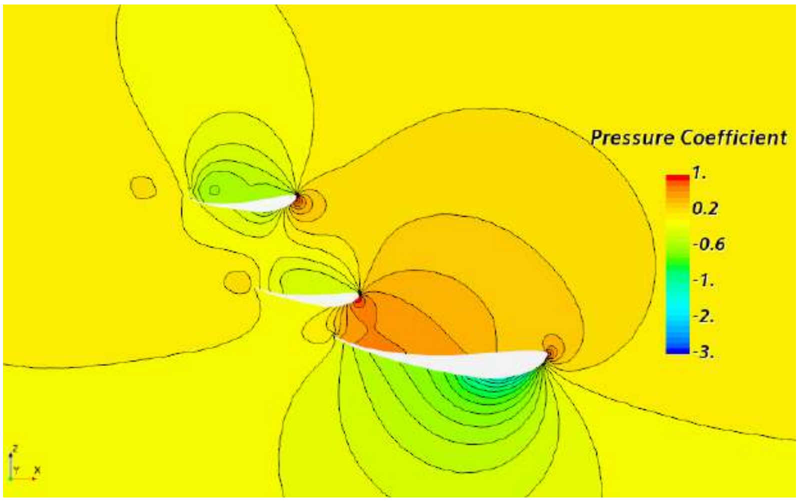

Figure 5.11: Pressure distribution in the symmetry plane for $\alpha_{flap1} = 0$ and $\alpha_{flap2} = -6$.

5.2.3 Centre of Rotation Optimization

When changing the center of rotation the flaps remained at 0 as referenced by the initial 2D study on the $S1223$ airfoil. Furthermore the current study of the optimum center of rotation can be mixed with the lowest drag study to try and understand if the optimum points from the two sets of simulations can be joined into a even better solution.

5.2.3.1 Mapping Results

The mapping results are presented in figures 5.15 to 5.17. The results show that the center of rotation has can achieve an impact of up around 5% of the lift and drag between

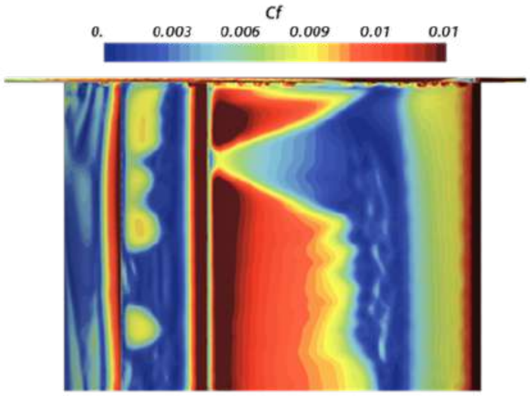

Figure 5.12: Bottom view of Skin friction coefficient distribution on the rear wing for $\alpha_{flap1} = 30$ and $\alpha_{flap2} = 55$

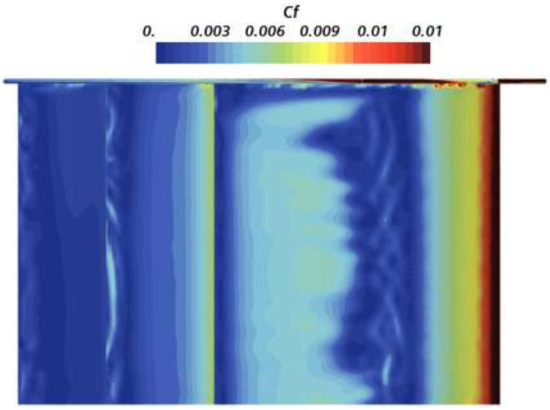

Figure 5.13: Bottom view of Skin friction coefficient distribution on the rear wing for $\alpha_{flap1} = 0$ and $\alpha_{flap2} = -6$

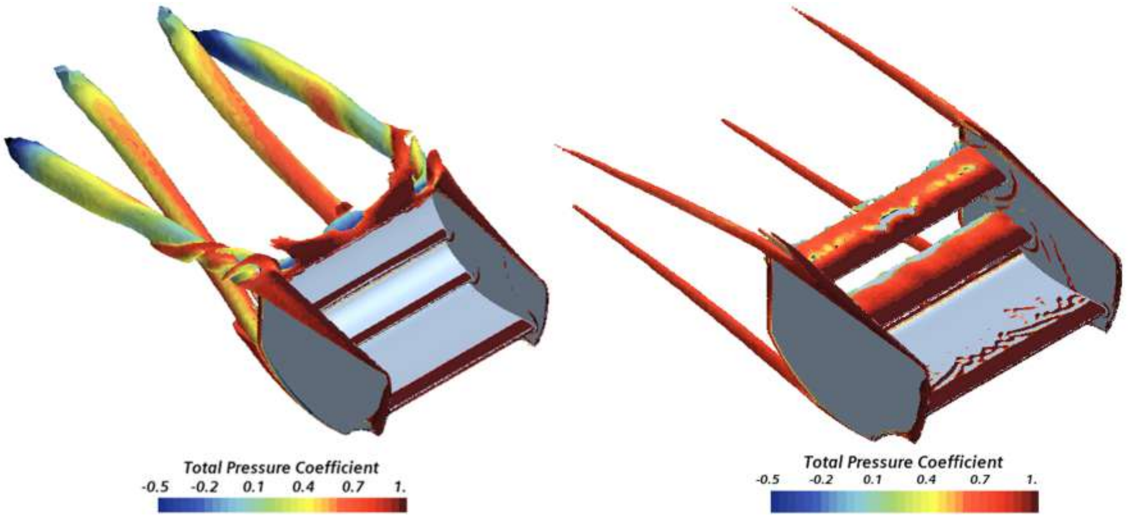

Figure 5.14: Total pressure coefficient representation on q-criterion isosurfaces for the baseline configuration (on the left) and for the lowest drag configuration (on the right).

the highest and lowest values. Reducing 5% comes has an improvement but has very low influence in the overall behaviour of the wing. Further iterations of the process can be done refining the angle step and with different angles other then zero. For the latter option the results from the previous macro simulations can be used as input and repeated.

From the mapping results it can be seen that the values decrease mostly with the distance the center of rotation of the second flap to the trailing edge.

5.2.3.2 Flow Analysis

Three of the most important cases are considered for further analysis of the flow: the highest lift configuration ($COR_{flap1} = 20$ and $COR_{flap2} = 100$), the lowest drag configurations ($COR_{flap1} = 20$ and $COR_{flap2} = 0$) cases and the highest efficiency case ($COR_{flap1} = 100$ and $COR_{flap2} = 0$).

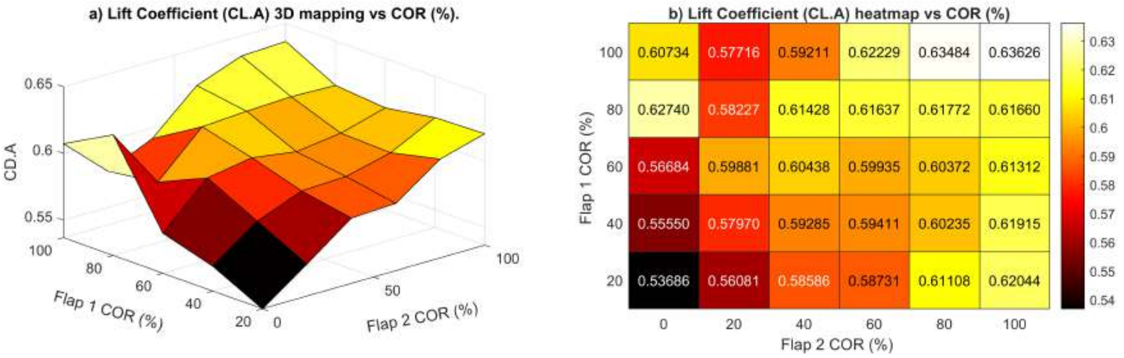

Figure 5.15: 3D mapping of the lift coefficient C_L as a function of the position of the center of rotation along the chord (%).

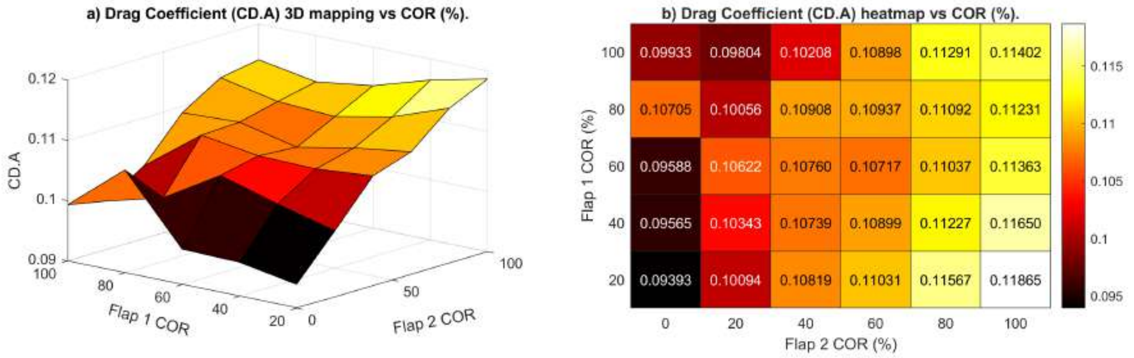

Figure 5.16: 3D mapping of the drag coefficient C_D as a function of the position of the center of rotation along the chord (%).

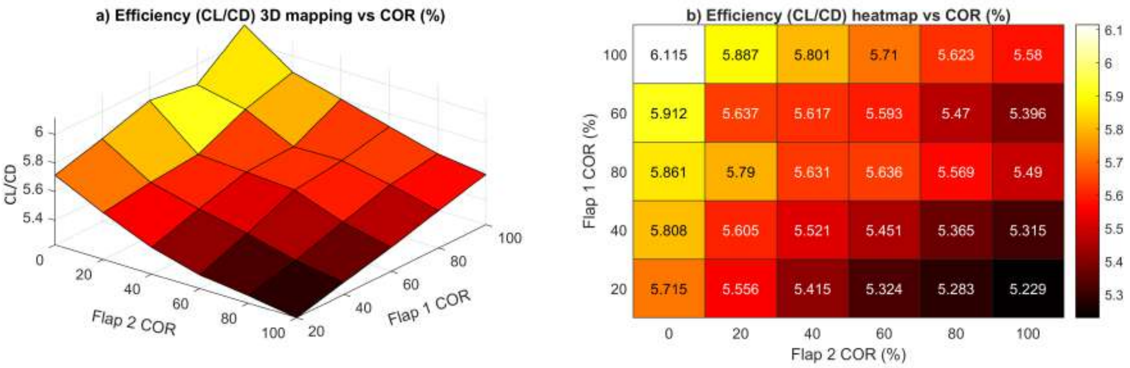

Figure 5.17: 3D mapping of the efficiency C_L/C_D as a function of the position of the center of rotation along the chord (%).

By looking at figures 5.18 it is possible to compare the three different cases. It is seen that the undisturbed flow approaching the second flap in the first case allows for the gurney flap itself to be more efficient enhancing the generated up-wash in the second flap region. This gives rise to extra downforce which reflects into additional drag. On the middle case the flaps are as close as possible to the main element and an interaction between flap 1 and flap 2 seems to create the recirculation on the pressure side of the first flap reducing it's downforce and drag. On the right image a close interaction is seen between the two flaps in such a way that they still produce more lift then the first case with reduced drag penalty on the gurney flap as a lower recirculation region is seen behind it. In a next stage the three configurations are mixed with the lowest drag angles of attack from the previous macro results, namely the $\alpha_{flap1} = 0$ and $\alpha_{flap2} = -6$ configuration.

5.2.3.3 Mixed Set of simulation

A new set of simulations is done in order to apply the best results from each macro's simulations, from the lowest drag configuration and best centers of rotations. Conclusions can be taken from each set of simulation. Table 5.1 shows all of the previous results adding the mixed results at the end. It is seen that the mixed configuration when the lowest drag configuration from each study are combined an even lower drag configuration can be achieved. A first iteration of the mixed simulation can reduce drag coefficient of the best center of rotation configuration in 26%, from 0.094 to 0.069, by only tilting the second flap by 6°.

The current configuration should then be taken again into the first macro doing an iterative process to fin the best configuration. The velocity contours of the lowest drag configuration achieved is presented in figure 5.19. The current solution achieves *CD.A* values which are lower than 94.5 % of the baseline configuration. It seems that the proximity between the two flaps induce an angle in the flow approaching the second flap creating a similar phenomenon to when the second flap is tilted −6 in the subchapter 5.2.2. The gurney flap of the second flap loses downforce generating capabilities and so induced drag is reduced. A first iteration of the best configuration is then achieved concluding on of the main goals of the thesis.

Table 5.1: Results table of the forces values for a few cases of two types of simulation set.

Simulation Type	Angles (°)	CORs (%)	CL.A	Lift Main	Lift Flap 1	Lift Flap 2	CD.A	Drag Main	Drag Flap 1	DragFlap 2
Baseline	30-55	50-50	1.790	162.60	58.32	27.96	0.730	11.56	42.00	46.00
Angles set	16-25	50-50	1.288	109.63	31.42	35.91	0.346	9.26	15.20	22.31
Angles set	0-55	50-50	0.980	93.99	18.42	23.07	0.422	5.88	5.68	45.65
Angles set	30-0	50-50	0.924	112.10	27.91	-13.13	0.218	9.28	19.14	1.15
Angles set	0-0	50-50	0.600	70.36	-8.15	20.56	0.109	6.13	6.13	5.63
Angles set	0-(-6)	50-50	0.371	65.52	-7.47	-7.06	0.070	5.55	2.04	1.43
COR set	0-0	20-0	0.537	69.70	-7.35	11.35	0.094	5.97	2.78	3.51
COR set	0-0	20-100	0.620	72.62	-6.62	19.16	0.119	6.38	3.22	6.06
COR set	0-0	100-0	0.577	70.16	1.85	7.20	0.098	6.01	2.72	4.10
Mixed	0-(-6)	20-0	0.374	64.94	-7.74	-5.70	0.069	5.56	2.23	0.98
Mixed	0-(-6)	20-100	0.421	64.40	-4.68	-1.92	0.070	5.48	1.60	1.93
Mixed	0-(-6)	100-0	0.449	71.05	-5.58	-5.58	0.089	5.92	2.89	2.96

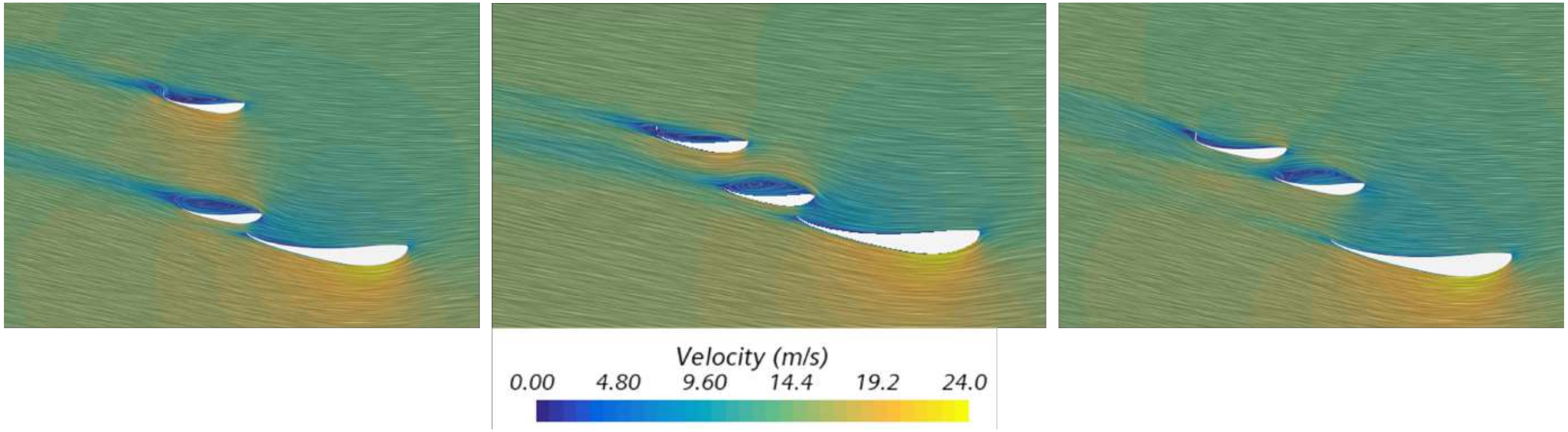

Figure 5.18: Midplane cross -section view of the velocity contours of the cases: the highest $C_L.A$ (COR_{flap1} = 20-COR_{flap2} = 100) on the left; the lowest $C_D.A$ (COR_{flap1} = 20- COR_{flap2} = 0) in the middle; and the highest efficiency case (COR_{flap1} = 100-COR_{flap2} = 0) on the right.

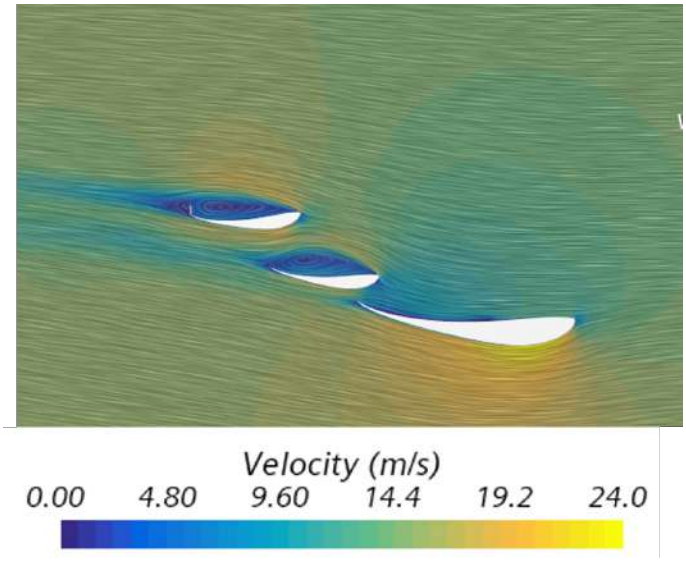

Figure 5.19: Velocity contours at the symmetry plane of the lowest drag configuration. Centers of rotation are: ($COR_{flap1} = 20$ - $COR_{flap2} = 0$); and the angles of the flaps are: ($\alpha_{flap1} = 0$ - $\alpha_{flap2} = -6$)

6

Final Remarks

6.1 Conclusions

Numerical simulation tools were used in order to achieve the best configuration of a typical Drag Reduction System of a 3 element wing where the two most rear-er flaps are rotated. The geometry taken into considerations was the FST 10e rear wing. Javascript macros were developed in order to grant an automatized mapping of the forces by automatically changing the geometry. The forces mapping was plotted against two separated types of study: an flaps angles study and a center of rotation study. The flap angle of attack set of simulations allowed to understand that rotating the second flap by 6° reduces the lifting effect of the gurney flap hence reducing the induced drag. The center of rotation set of simulation allowed to achieve the optimal solution within the range of centers of rotation tested for a 0° angle of attack for both flaps. Combining the results from both set of simulations it was possible to obtain a first ideal solution. Studies conducted showed that the a first iteration of the process can reduce the rear wing's drag up to 94.5%. The best results from each study can work as input for the other study in order to converge to the best DRS solution.

6.2 Considerations For Other Engineering Fields

One should note that the results achieve are very specific for the case being studied. Velocity remains constant and the wing is studied in free stream. Further studies are suggested from a CFD and other departments points of view.

6.2.1 Structures

The results achieve and assumed ideal didn't consider the necessary momentum to be applied to the flaps in order to rotate them. If the necessary mechanical system is too complex or weights too much than the DRS can actually worsen the car performance. Careful assessment and investigation of the available rotation mechanisms should be done in order to find the least complex and lightest. The most common ones are the servo motors and the actuators, the latter being electric for enhanced control over the wing or pneumatic for heavier loads.

Integration of the system should be studied also having in mind that it should occupy the least frontal area possible. If possible integrated in the endplates. Studies around the integration of the system at the midplane of the wing or at the endplates is suggested.

6.2.2 Vehicle Dynamics and Suspension

Continuous measurements from deformation sensors could be used to assess the radial force applied on the car and applied as input into a future integrated control model that makes a continues choice of the optimum flap configuration. Lap simulation should be run for both types of DRS (discrete and continuous) to quantify the real benefits of the introduction of the system in the studied configuration.

The development of an Arduino system to integrate the previous model and control the flaps is suggested.

6.3 Future CFD Work Suggestions

Regarding the future CFD work that could be done around the current dissertation, a few points are highlighted:

- Improve the overall macro;
- Adapt macro for the full car simulation;
- Do cornering simulations evaluating the change in performance of the DRS force mapping;
- Do further research on a less refined mesh that can be used for this purpose with a bigger angle-step. The goal should be to decrease the computational time to allow for more studies iterations.
- Do velocity-sensitivity tests by varying the inlet velocity and verify how the forces coefficients overall mapping is influenced.
- Assess the DRS performance when cornering and how it affects a transient simulations of the closing flaps;
- Elaborate a transient study around of the closing of the flaps. The goal should be to evaluate how long it takes for the efficiency of rear wing to be fully restored once it is back to the baseline configuration. Investigation around the practical application of the Detached Eddy Simulation is recommended.

BIBLIOGRAPHY

[1] J. Katz. "Aerodynamics in motorsports". In: *Proceedings of the Institution of Mechanical Engineers, Part P: Journal of Sports Engineering and Technology* (2019), p. 1754337119893226 (cit. on p. 1).

[2] W. F. Milliken, D. L. Milliken, et al. *Race car vehicle dynamics*. Vol. 400. Society of Automotive Engineers Warrendale, PA, 1995 (cit. on pp. 2, 16, 19–21, 29, 32).

[3] X. Zhang, W. Toet, and J. Zerihan. "Ground effect aerodynamics of race cars". In: (2006) (cit. on pp. 3, 29).

[4] J. Katz. *Race car aerodynamics: designing for speed*. R. Bentley, 1995 (cit. on pp. 4, 16, 21, 22, 25–28).

[5] H. Dahlberg. *Aerodynamic development of Formula Student race car*. 2014 (cit. on p. 4).

[6] F. S. Germany. *Formula student rules 2020*. URL: `https://www.formulastudent.de/fsg/rules`. (accessed: 19.05.2021) (cit. on pp. 6, 7).

[7] L. A. Oliveira and A. G. Lopes. "Mecânica dos fluidos". In: *ETEP–Edições Técnicas e Profissionais, 3ª Edição, Lisboa* (2010) (cit. on pp. 11, 16).

[8] J. Winslow et al. "Basic understanding of airfoil characteristics at low Reynolds numbers (10 4–10 5)". In: *Journal of Aircraft* 55.3 (2018), pp. 1050–1061 (cit. on p. 11).

[9] A. G. Lopes and P. Carvalheira. *On the application of numerical methods for the calculation of the external aerodynamics of a streamlined car body*. Tech. rep. SAE Technical Paper, 2003 (cit. on p. 15).

[10] V. d. Brederode. "Fundamentos de aerodinâmica incompressıvel". In: *Edição do autor* (1997) (cit. on pp. 16, 17, 19, 28, 36).

[11] J. Fürst, P. Straka, and J. Přıhoda. "Modelling of natural and bypass transition in aerodynamics". In: *EPJ Web of Conferences*. Vol. 67. EDP Sciences. 2014, p. 02030 (cit. on p. 17).

[12] H. Schlichting and K. Gersten. *Boundary-layer theory*. Springer, 2016 (cit. on pp. 17, 19–21, 36).

[13] F. White. *Fluid Mechanics*. McGraw-Hill series in mechanical engineering. McGraw Hill, 2011. ISBN: 9780073529349. URL: `https://books.google.de/books?id=egk8SQAACAAJ` (cit. on p. 17).

[14] L. S. Roberts, M. V. Finnis, and K. Knowles. "Forcing boundary-layer transition on a single-element wing in ground effect". In: *Journal of Fluids Engineering* 139.10 (2017) (cit. on p. 17).

[15] S. McBeath. *Competition Car Aerodynamics 3rd Edition*. Veloce Publishing Ltd, 2017 (cit. on pp. 18, 22, 26, 30).

[16] H. K. Versteeg and W. Malalasekera. *An introduction to computational fluid dynamics: the finite volume method*. Pearson education, 2007 (cit. on pp. 18–20, 44, 47, 52, 94).

[17] H. Kudela. *Turbulent flow*. 2010 (cit. on pp. 20, 37).

[18] P. A. Durbin. "Perspectives on the phenomenology and modeling of boundary layer transition". In: *Flow, Turbulence and Combustion* 99.1 (2017), pp. 1–23 (cit. on p. 21).

[19] A. Uranga. "Investigation of transition to turbulence at low Reynolds numbers using Implicit Large Eddy Simulations with a Discontinuous Galerkin method". PhD thesis. University of California, Berkeley, 2010 (cit. on p. 22).

[20] M. Arianezhad. "Numerical study and optimization of a GT car Rear-Wing aerodynamics". MA thesis. Universitat Politècnica de Catalunya, 2015 (cit. on p. 22).

[21] D. Izquierdo Susın. "Foundations, Methodologies and Design of the Formula UC3M Car Aerodynamics". B.S. thesis. 2019 (cit. on p. 26).

[22] T. Rocha. "Numerical and Experimental Study of Wing Tip Endplates of a Formula Student Car". PhD thesis. University de Lisboa, Instituto Superior Técnico, 2020 (cit. on pp. 27, 29).

[23] J. D. Anderson Jr. *Fundamentals of aerodynamics*. Tata McGraw-Hill Education, 2010 (cit. on p. 28).

[24] J. Keogh et al. "The influence of cornering on the vortical wake structures of an inverted wing". In: *Proceedings of the Institution of Mechanical Engineers, Part D: Journal of Automobile Engineering* 229.13 (2015), pp. 1817–1829 (cit. on p. 29).

[25] X. Zhang and J. Zerihan. "Off-surface aerodynamic measurements of a wing in ground effect". In: *Journal of Aircraft* 40.4 (2003), pp. 716–725 (cit. on pp. 29, 68, 69).

[26] V. V. Raul. "Analysis of F-duct drag reduction system in Formula 1". PhD thesis. Wichita State University, 2013 (cit. on p. 30).

[27] S. Wordley et al. "Development of a Drag Reduction System (DRS) for multi-element race car wings". English. In: *Proceedings of the 19th Australasian Fluid Mechanics Conference (AFMC)*. Ed. by H. Chowdhury and F. Alam. Australasian Fluid Mechanics Conference 2014, AFMC 2014 ; Conference date: 08-12-2014 Through 11-12-2014. RMIT University, 2014, pp. 1–4. ISBN: 9780646596952. URL: `http://afms.org.au/19AFMC/` (cit. on pp. 30, 32, 33, 57).

[28] D. Friedman. *Chaparral: Can-Am Andprototype Race Cars*. Motorbooks, 2005 (cit. on p. 30).

[29] A. Barari, F. Diba, and E. Esmailzadeh. "Down force control of the low velocity racing car using active aerodynamic inverse wings". In: *International Design Engineering Technical Conferences and Computers and Information in Engineering Conference*. Vol. 54853. 2011, pp. 739–745 (cit. on p. 32).

[30] J. P. Merkel. "Development of multi-element active aerodynamics for the Formula SAE car". In: (2014) (cit. on pp. 32, 34).

[31] R. W. Fox, A. T. McDonald, and J. W. Mitchell. *Fox and McDonald's introduction to fluid mechanics*. John Wiley & Sons, 2020 (cit. on p. 35).

[32] J. Daily and D. Harleman. *Fluid Dynamics, 1966* (cit. on p. 36).

[33] D. J. Penner. *Aerodynamic Design and Analysis of a Formula SAE Drag Reduction System (DRS)*. Tech. rep. SAE Technical Paper, 2020 (cit. on p. 37).

[34] F. R. Menter. "Two-equation eddy-viscosity turbulence models for engineering applications". In: *AIAA Journal* 32.8 (1994), pp. 1598–1605. ISSN: 00011452. DOI: `10.2514/3.12149` (cit. on pp. 39, 40, 52).

[35] A. Matyushenko, A. Stabnikov, and A. Garbaruk. "Criteria of computational grid generation for turbulence models taking into account laminar-turbulent transition". In: *Journal of Physics: Conference Series*. Vol. 1400. 7. IOP Publishing. 2019, p. 077047 (cit. on p. 42).

[36] F. R. Menter et al. "A One-Equation Local Correlation-Based Transition Model". In: *Flow, Turbulence and Combustion* 95.4 (2015), pp. 583–619. ISSN: 15731987. DOI: `10.1007/s10494-015-9622-4` (cit. on p. 42).

[37] R. B. Langtry and F. R. Menter. "Correlation-based transition modeling for unstructured parallelized computational fluid dynamics codes". In: *AIAA journal* 47.12 (2009), pp. 2894–2906 (cit. on p. 42).

[38] H. Jasak. "Error analysis and estimation for the finite volume method with applications to fluid flows." In: (1996) (cit. on p. 43).

[39] S. P. Software. *Simcenter StarCCM+ ©Documentation*. Version 2020.3, 2021 (cit. on p. 44).

[40] S. Durrer. "Aerodynamics of Race Car Wings: A CFD Study". In: (2016) (cit. on p. 44).

[41] W. L. Oberkampf and T. G. Trucano. “Verification and validation in computational fluid dynamics”. In: *Progress in aerospace sciences* 38.3 (2002), pp. 209–272 (cit. on pp. 47, 48).

[42] F. Stern et al. “Comprehensive approach to verification and validation of CFD simulations—part 1: methodology and procedures”. In: *J. Fluids Eng.* 123.4 (2001), pp. 793–802 (cit. on p. 47).

[43] S. B. Pope. “A perspective on turbulence modeling”. In: *Modeling complex turbulent flows*. Springer, 1999, pp. 53–67 (cit. on p. 48).

[44] L. Eça and M. Hoekstra. “A procedure for the estimation of the numerical uncertainty of CFD calculations based on grid refinement studies”. In: *Journal of computational physics* 262 (2014), pp. 104–130 (cit. on p. 48).

[45] F. S. Pereira et al. “Toward predictive RANS and SRS computations of turbulent external flows of practical interest”. In: *Archives of Computational Methods in Engineering* (2021), pp. 1–77 (cit. on p. 48).

[46] G. B. B. Hübbe et al. “Numerical and experimental anlysis of a high Lifting airfoil at Low reynolds number flows”. In: (2017) (cit. on pp. 49, 52–54).

[47] M. Hepperle. *JavaFoil*. URL: `https://www.mh-aerotools.de/airfoils/javafoil.htm` (visited on 08/19/2021) (cit. on p. 50).

[48] M. S. Selig and J. J. Guglielmo. “High-lift low Reynolds number airfoil design”. In: *Journal of aircraft* 34.1 (1997), pp. 72–79 (cit. on p. 50).

[49] J. H. Ferziger, M. Perić, and R. L. Street. *Computational methods for fluid dynamics*. Vol. 3. Springer, 2002 (cit. on pp. 93, 94).

A

Appendix 1

A.1 Gauss Divergence Theorem

The divergence theorem relates the divergence of a vector field in a enclosed volume with the flux of the field through a closed surface. In fluid dynamics, applying it to a fluid flow, the theorem states that the total volume of all sinks and sources is equal to the net flow across the volume's boundary surfaces.

$$\iiint_V (\nabla \cdot \mathbf{F}) \mathrm{d}V = \oiint_S (\mathbf{F} \cdot \hat{\mathbf{n}}) \mathrm{d}S \tag{A.1}$$

A.2 Integration Approximations

As explained StarCCM+ utilizes a set of surface and volume integrals approximations applying quadrature formulae [49] in order to obtain an algebraic equation for a specific control volume.

A.2.1 Surface Integrals approximation

The left hand-side of the A.2 approximation the net flux through a control volume's surfaces is equally related to the right hand-side, the sum of the integrals over the control volume's faces [49].

$$\int_S f \ \mathrm{d}S = \sum_k \int_{S_k} f \ \mathrm{d}S \tag{A.2}$$

In the previous approximations f represents the convective or diffusive component of the transport equation. The midpoint rule can be applied to the right hand-side, A.3

$$\int_{S_e} f \ \mathrm{d}S = \bar{f}_\mathrm{e} S_\mathrm{e} \approx f_\mathrm{e} S_\mathrm{e} \tag{A.3}$$

to give the final Star CCM+ surface integral the second-order accurate expression A.4 if the value of f at the location e was known.

$$\int_S f \, \mathrm{d}S = \sum_k f_\mathrm{e} S_\mathrm{e} \tag{A.4}$$

As the value of the diffusive or convective fluxes needs to be computed, the values and gradient of a certain quantity ϕ normal to a cell surfaces need to be approximated.

Several interpolation methods need to be applied:

- The **First** and **Second-order Upwind** Differencing Schemes;
- **Central** Differencing Scheme;
- **Hybrid** Differencing Scheme

Detailed exploration of these schemes is out of the scope this thesis. These can be further analysed in the references [16], [49].

A.2.2 Volume Integrals approximation

For the terms in the transport equations that require integration over the control volume the second-order accurate approximation A.5 is applied by the software according to the formulation in [49].

$$Q_\mathrm{P} = \int_\Omega q \, \mathrm{d}\Omega = \bar{q}\Delta\Omega \approx q_\mathrm{P}\Delta\Omega \tag{A.5}$$

I

Annex 1 DRS StarCCM+ Main Macro

Within each of the following *Main* macros there are submacros initiated by "that will not appear due to the team confidentiality. There funtionality is to:

I.1 DRS Angles Macro

The following macro does creates one cycles for each flap where it is possible to define an initial and final angle of attack. The center of rotations is defined at a 50% chord projection on the camber line of each flap.

I.2 Centres of Rotation Angles Macro

```
// STAR-CCM+ macro: MAIN_DRS.java
// Written by STAR-CCM+ 14.04.011
package macro;

import java.util.*;

import star.common.*;
import star.base.neo.*;
import java.io.*;
import star.vis.*;
import star.meshing.*;
import java.io.IOException;
import star.cadmodeler.*;
import star.base.query.*;
import star.base.report.*;
import star.flow.*;

public class MAIN_DRS extends StarMacro {

  public void execute() {
    execute0();
  }
    //..................Change Refinement ratio IF NEEDED----------------------------------------------------------------
 double Ri = 1.4;

   // ------- CHANGE VALUES HERE ---------------------------------------------------------------------------------------

 //flap 1 - ang0 = 30
double start_angle_in_degrees_flap1 = 0;
double angle_increment_in_degrees_flap1 = 2;
double max_angle_in_degrees_flap1 = 36;

//flap 2 - ang0 = 55
double start_angle_in_degrees_flap2 = 0;
double angle_increment_in_degrees_flap2 = 2;
double max_angle_in_degrees_flap2 = 66;
 // ----------------------------------------------------------------------------------------------------------------

  private void execute0() {

  Simulation simulation_0 =
      getActiveSimulation();
  UserFieldFunction userFieldFunction_3 =
      simulation_0.getFieldFunctionManager().createFieldFunction();

    userFieldFunction_3.getTypeOption().setSelected(FieldFunctionTypeOption.Type.SCALAR);
    userFieldFunction_3.setPresentationName("Ri");
    userFieldFunction_3.setFunctionName("Ri");
    userFieldFunction_3.setDefinition(Double.toString(Ri));

new StarScript(getActiveRootObject(), new File(resolvePath("Modules_Macro_DRS\\a_ImportCAD_DRS_v2.java"))).play();
new StarScript(getActiveRootObject(), new File(resolvePath("Modules_Macro_DRS\\c_Input_Domain_Controls.java"))).play();
 new StarScript(getActiveRootObject(), new File(resolvePath("Modules_Macro_DRS\\c2_NewDBsCuts.java"))).play();

new StarScript(getActiveRootObject(), new File(resolvePath("Modules_Macro_DRS\\d_SWrapper_FluidFanRad.java"))).play();
new StarScript(getActiveRootObject(), new File(resolvePath("Modules_Macro_DRS\\e_Models_Regions_Interfaces.java"))).play(
//new StarScript(getActiveRootObject(), new File(resolvePath("Modules_Macro_DRS\\f_AutoMesh.java"))).play();
new StarScript(getActiveRootObject(), new File(resolvePath("Modules_Macro_DRS\\f_AutoMesh2.java"))).play();
 new StarScript(getActiveRootObject(), new File(resolvePath("Modules_Macro_DRS\\g_ReportsMonitorsPlots.java"))).play();

simulation_0.saveState(resolvePath("Simulations\\A_Stage0.sim"));

//____________________

  SimpleAnnotation simpleAnnotation_1 =
      simulation_0.getAnnotationManager().createSimpleAnnotation();
    simpleAnnotation_1.setPresentationName("AOA_Flap1");

  SimpleAnnotation simpleAnnotation_2 =
      simulation_0.getAnnotationManager().createSimpleAnnotation();
    simpleAnnotation_2.setPresentationName("AOA_Flap2");

  //_____________________flap_1_Change_AOA______________________________________________

 for (double i = start_angle_in_degrees_flap1; i <= max_angle_in_degrees_flap1; i = i+angle_increment_in_degrees_flap1) {

  double attack_angle = Math.toRadians(i);

    CadModel cadModel_0 =
      ((CadModel) simulation_0.get(SolidModelManager.class).getObject("3D-CAD Model 1"));
    ScalarQuantityDesignParameter scalarQuantityDesignParameter_0 =
      ((ScalarQuantityDesignParameter) cadModel_0.getDesignParameterManager().getObject("Flap 1 (Ang0 = 30\u00BA)"));
```

```
    scalarQuantityDesignParameter_0.getQuantity().setValue(i);
    Units units_0 =
      ((Units) simulation_0.getUnitsManager().getObject("deg"));
    scalarQuantityDesignParameter_0.getQuantity().setUnits(units_0);

   simpleAnnotation_1.setText(""+i);

//____________________flap_2_Change_AOA__________________________________________

 for (double j = start_angle_in_degrees_flap2; j <= max_angle_in_degrees_flap2; j = j+angle_increment_in_degrees_flap2) {


   ScalarQuantityDesignParameter scalarQuantityDesignParameter_1 =
     ((ScalarQuantityDesignParameter) cadModel_0.getDesignParameterManager().getObject("Flap 2 (ang0 = 55\u00BA)"));
    scalarQuantityDesignParameter_1.getQuantity().setValue(j);
    scalarQuantityDesignParameter_1.getQuantity().setUnits(units_0);

    simpleAnnotation_2.setText(""+j);

  //__________________________________________________________________________________

    MeshPipelineController meshPipelineController_0 =
      simulation_0.get(MeshPipelineController.class);
    meshPipelineController_0.generateVolumeMesh();
    //________________________________________________________________________________

simulation_0.saveState(resolvePath("Simulations\\Flap1="+ i +"_Flap2="+ j +".sim"));

new File(resolvePath("Post_Processing\\Flap1="+ i +"_Flap2="+ j +"")).mkdirs();
new File(resolvePath("Post_Processing\\Flap1="+ i +"_Flap2="+ j +"\\Monitors\\Scenes")).mkdirs();


    LabCoordinateSystem labCoordinateSystem_0 =
      simulation_0.getCoordinateSystemManager().getLabCoordinateSystem();
    CartesianCoordinateSystem cartesianCoordinateSystem_0 =
      labCoordinateSystem_0.getLocalCoordinateSystemManager().createLocalCoordinateSystem(CartesianCoordinateSystem.class
    cartesianCoordinateSystem_0.setBasis0(new DoubleVector(new double[] {1.0, -Math.atan(attack_angle), 0.0}));
    cartesianCoordinateSystem_0.setPresentationName("Axis_F1");

  //______________________________________________________________________________________________________________________

        simulation_0.saveState(resolvePath("Simulations\\Flap1="+ i +"_Flap2="+ j +".sim"));
  new StarScript(getActiveRootObject(), new File(resolvePath("Modules_Macro_DRS\\h_RunSolver.java"))).play();
 simulation_0.saveState(resolvePath("Simulations\\Flap1="+ i +"_Flap2="+ j +".sim"));



  new StarScript(getActiveRootObject(), new File(resolvePath("Modules_Macro_DRS\\i_Cp_CoP.java"))).play();
  new StarScript(getActiveRootObject(), new File(resolvePath("Modules_Macro_DRS\\j_ExportFiles.java"))).play();
  new StarScript(getActiveRootObject(), new File(resolvePath("Modules_Macro_DRS\\j_ExportFilesV2.java"))).play();

        simulation_0.saveState(resolvePath("Simulations\\Flap1="+ i +"_Flap2="+ j +".sim"));


        Solution solution_99 =
      simulation_0.getSolution();
    solution_99.clearSolution(Solution.Clear.History, Solution.Clear.Fields, Solution.Clear.LagrangianDem);
     Scene scene_2 =
      simulation_0.getSceneManager().getScene("CP");
   simulation_0.getSceneManager().deleteScenes(new NeoObjectVector(new Object[] {scene_2}));

////////////////////
    new StarScript(getActiveRootObject(), new File(resolvePath("Modules_Macro_DRS\\NewRESET.java"))).play();

  }

}
  }
}
```

```java
// Simcenter STAR-CCM+ macro: changeCOR.java
// Written by Simcenter STAR-CCM+ 15.06.008
package macro;

import java.util.*;
import star.common.*;
import star.base.neo.*;
import java.io.*;
import star.vis.*;
import star.meshing.*;
import java.io.IOException;
import star.cadmodeler.*;
import star.base.query.*;
import star.base.report.*;
import star.flow.*;
import star.cadmodeler.*;

//import star.base.neo.DoubleArrayVector;
/*____________________________These_are_the__COR__used______________
Flap 1 20-100%
Flap1COR=[-1710.156296,-442.7,862.293048
-1745.014897,-442.7,882.3345182
-1777.218353,-442.7,906.0650606
-1807.291084,-442.7,932.7560427
-1832.32985,-442.7,966.4472037

Flap 2 0-100%
-1812.071931,-442.7,986.1858766
-1843.754519,-442.7,1014.286533
-1866.403771,-442.7,1047.447384
-1885.390372,-442.7,1082.659939
-1901.624125,-442.7,1119.414552
-1909.816742,-442.7,1160.677552
*/

public class COR_SIM_Macro extends StarMacro {

  public void execute() {
   double Ri = 1.4;
    execute0();
  }

  private void execute0() {
    Simulation simulation_0 =
      getActiveSimulation();

         // ------- CHANGE VALUES HERE -----------------------------------------
// These showld be the real values for the angle of attack
   double aoa1 = 0;
   double aoa2 = 0;

  UserFieldFunction userFieldFunction_3 =
      simulation_0.getFieldFunctionManager().createFieldFunction();
userFieldFunction_3.getTypeOption().setSelected(FieldFunctionTypeOption.Type.SCALAR);
userFieldFunction_3.setPresentationName("Ri");
userFieldFunction_3.setFunctionName("Ri");
userFieldFunction_3.setDefinition(Double.toString(Ri));

new StarScript(getActiveRootObject(), new File(resolvePath("Modules_Macro_DRS\\a_ImportCAD_DRS_v2.java"))).play();
new StarScript(getActiveRootObject(), new File(resolvePath("Modules_Macro_DRS\\c_Input_Domain_Controls.java"))).play();
 new StarScript(getActiveRootObject(), new File(resolvePath("Modules_Macro_DRS\\c2_NewDBsCuts.java"))).play();
new StarScript(getActiveRootObject(), new File(resolvePath("Modules_Macro_DRS\\d_SWrapper_FluidFanRad.java"))).play();
new StarScript(getActiveRootObject(), new File(resolvePath("Modules_Macro_DRS\\e_Models_Regions_Interfaces.java"))).play(
//new StarScript(getActiveRootObject(), new File(resolvePath("Modules_Macro_DRS\\f_AutoMesh.java"))).play();
new StarScript(getActiveRootObject(), new File(resolvePath("Modules_Macro_DRS\\f_AutoMesh2.java"))).play();
 new StarScript(getActiveRootObject(), new File(resolvePath("Modules_Macro_DRS\\g_ReportsMonitorsPlots.java"))).play();

simulation_0.saveState(resolvePath("Simulations\\A_Stage0.sim"));

  //____________________Change_of_AOA____________________________________________

double AOA1=30-aoa1;
double AOA2=55-aoa2;
//_________________
  SimpleAnnotation simpleAnnotation_1 =
      simulation_0.getAnnotationManager().createSimpleAnnotation();
    simpleAnnotation_1.setPresentationName("Flap1_COR");

  SimpleAnnotation simpleAnnotation_2 =
      simulation_0.getAnnotationManager().createSimpleAnnotation();
    simpleAnnotation_2.setPresentationName("Flap2_COR");
```

```
  SimpleAnnotation simpleAnnotation_4 =
      simulation_0.getAnnotationManager().createSimpleAnnotation();
    simpleAnnotation_4.setPresentationName("AOA_Flap1");
    simpleAnnotation_4.setText(""+AOA1+"");

  SimpleAnnotation simpleAnnotation_3 =
      simulation_0.getAnnotationManager().createSimpleAnnotation();
    simpleAnnotation_3.setPresentationName("AOA_Flap2");
    simpleAnnotation_3.setText(""+AOA2+"");


//_________________________Beggining of blocks ____________________________

   CadModel cadModel_0 =
      ((CadModel) simulation_0.get(SolidModelManager.class).getObject("3D-CAD Model 1"));
    simulation_0.get(SolidModelManager.class).editCadModel(cadModel_0);
    Units units_0 =
      ((Units) simulation_0.getUnitsManager().getObject("mm"));

//----------------------------------------- Paste blocks after this -----------------------

//////////////////////THIS IS THE ONE BLOCK ONLY///////////////////////////////////////////
////THE REST OF THE BLOCKS MUST BE GENERATED IN THE MATLAB FUNCTION writeBlocks.m //////////
///// PASTE THE OTHER BLOCKS BELOW/////////////////////////////////////////


/////////////////////////////////////////////////////////////////////
////////////////Beginning of block____Flap1_20Flap2_0____///////////////
/////////////////////////////////////////////////////////////////////
    RotateBodyFeature rotateBodyFeature_11 =
      ((RotateBodyFeature) cadModel_0.getFeature("Flap 1 (Ang0=30\u00BA)"));
//////////////////// Flap 1/////////////////////////////////////////////
 rotateBodyFeature_11.getPosition().setCoordinate(units_0, units_0, units_0, new DoubleVector(new double...~
  ~...[] {-1710.1563,-442.7,862.293}));
 simpleAnnotation_1.setText("20");
//////////////////////////////////////////////////////////////
    RotateBodyFeature rotateBodyFeature_1010 =
      ((RotateBodyFeature) cadModel_0.getFeature("Flap 2 (ang0 = 55\u00BA)"));
///////////////////FLAP_2/////////////////////////////////////////////
 rotateBodyFeature_1010.getPosition().setCoordinate(units_0, units_0, units_0, new DoubleVector(new double[]...~
 ...~ {-1812.0719,-442.7,986.1859}));
 simpleAnnotation_2.setText("0");
//////////////////////////////////////////////////////////////
cadModel_0.getFeatureManager().updateModelUpto(rotateBodyFeature_11);
cadModel_0.getFeatureManager().updateModelUpto(rotateBodyFeature_1010);
   /*MeshPipelineController meshPipelineController_0 =
    simulation_0.get(MeshPipelineController.class);
    meshPipelineController_0.generateVolumeMesh();*/
new StarScript(getActiveRootObject(), new File(resolvePath("MAIN_DRS.java"))).play();
simulation_0.saveState(resolvePath("Simulations\\Flap1=20_Flap2=0.sim"));

/////////////////////////////////////////////////////////////////////
////////////////////////End of block_____Flap1_20Flap2_0____//////////
/////////////////////////////////////////////////////////////////////

////....... ADD MORE BLOCKS ....../////


}
```

II

ANNEX 2 MATLAB BLOCK WRITER FUNCTION

The matlab function in the next page writes a *txt* file containing the all of the needed blocks for the angles of attack simulations to be introduced in the COR Macro in the proper section. It should redirect to the *help.txt* which is a sample file from which all of the simulation blocks will be created.

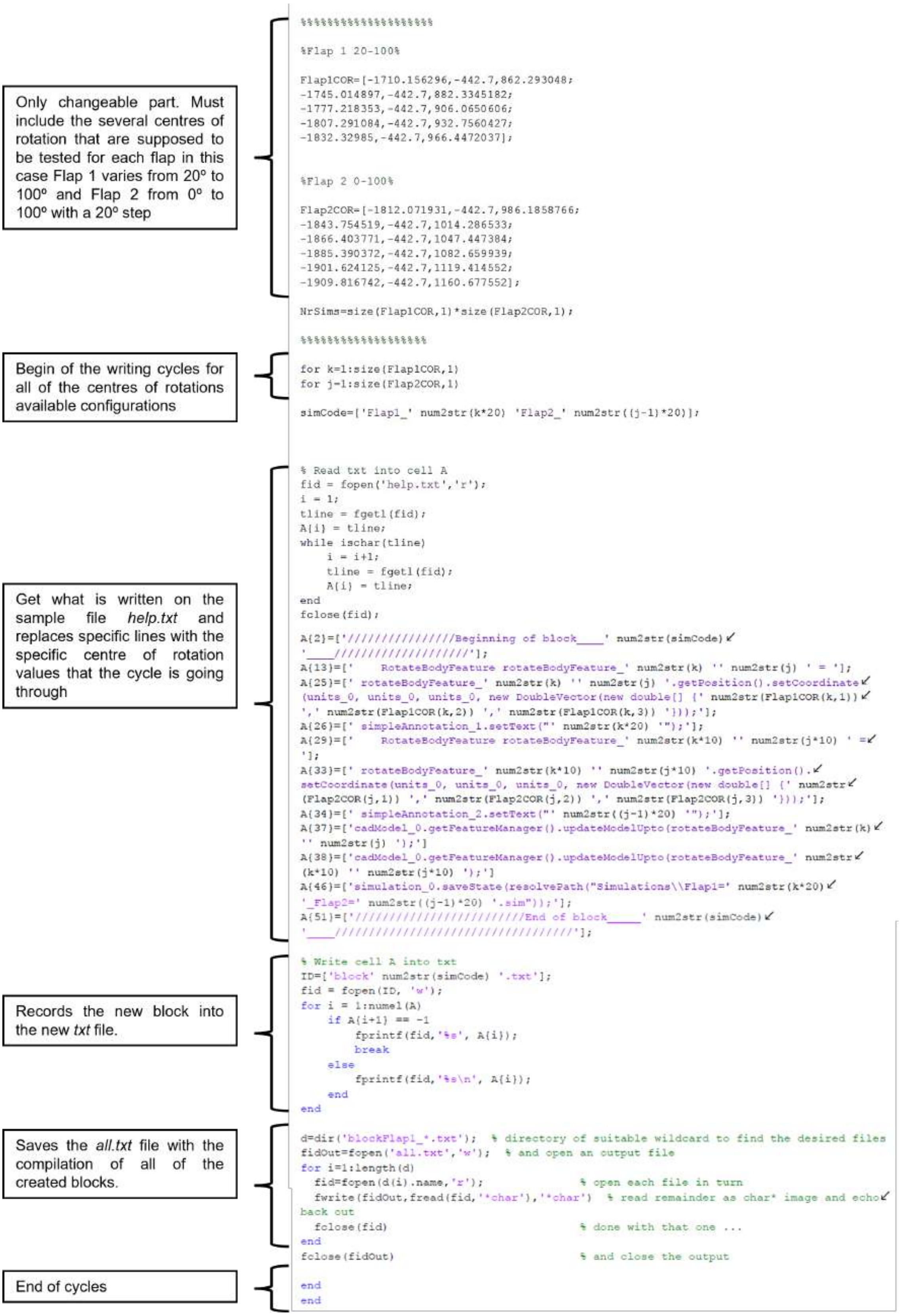

Only changeable part. Must include the several centres of rotation that are supposed to be tested for each flap in this case Flap 1 varies from 20° to 100° and Flap 2 from 0° to 100° with a 20° step

```
%%%%%%%%%%%%%%%%%%%%

%Flap 1 20-100%

Flap1COR=[-1710.156296,-442.7,862.293048;
-1745.014897,-442.7,882.3345182;
-1777.218353,-442.7,906.0650606;
-1807.291084,-442.7,932.7560427;
-1832.32985,-442.7,966.4472037];


%Flap 2 0-100%

Flap2COR=[-1812.071931,-442.7,986.1858766;
-1843.754519,-442.7,1014.286533;
-1866.403771,-442.7,1047.447384;
-1885.390372,-442.7,1082.659939;
-1901.624125,-442.7,1119.414552;
-1909.816742,-442.7,1160.677552];

NrSims=size(Flap1COR,1)*size(Flap2COR,1);

%%%%%%%%%%%%%%%%%%%
```

Begin of the writing cycles for all of the centres of rotations available configurations

```
for k=1:size(Flap1COR,1)
for j=1:size(Flap2COR,1)

simCode=['Flap1_' num2str(k*20) 'Flap2_' num2str((j-1)*20)];
```

Get what is written on the sample file *help.txt* and replaces specific lines with the specific centre of rotation values that the cycle is going through

```
% Read txt into cell A
fid = fopen('help.txt','r');
i = 1;
tline = fgetl(fid);
A{i} = tline;
while ischar(tline)
    i = i+1;
    tline = fgetl(fid);
    A{i} = tline;
end
fclose(fid);

A{2}=['////////////////Beginning of block____' num2str(simCode)↙
'____//////////////////////'];
A{13}=['    RotateBodyFeature rotateBodyFeature_' num2str(k) '' num2str(j) ' = '];
A{25}=[' rotateBodyFeature_' num2str(k) '' num2str(j) '.getPosition().setCoordinate↙
(units_0, units_0, units_0, new DoubleVector(new double[] {' num2str(Flap1COR(k,1))↙
',' num2str(Flap1COR(k,2)) ',' num2str(Flap1COR(k,3)) '}));'];
A{26}=[' simpleAnnotation_1.setText("' num2str(k*20) '");'];
A{29}=['    RotateBodyFeature rotateBodyFeature_' num2str(k*10) '' num2str(j*10) ' =↙
'];
A{33}=[' rotateBodyFeature_' num2str(k*10) '' num2str(j*10) '.getPosition().↙
setCoordinate(units_0, units_0, units_0, new DoubleVector(new double[] {' num2str↙
(Flap2COR(j,1)) ',' num2str(Flap2COR(j,2)) ',' num2str(Flap2COR(j,3)) '}));'];
A{34}=[' simpleAnnotation_2.setText("' num2str((j-1)*20) '");'];
A{37}=['cadModel_0.getFeatureManager().updateModelUpto(rotateBodyFeature_' num2str(k)↙
'' num2str(j) ');']
A{38}=['cadModel_0.getFeatureManager().updateModelUpto(rotateBodyFeature_' num2str↙
(k*10) '' num2str(j*10) ');']
A{46}=['simulation_0.saveState(resolvePath("Simulations\\Flap1=' num2str(k*20)↙
'_Flap2=' num2str((j-1)*20) '.sim"));'];
A{51}=['///////////////////////////End of block_____' num2str(simCode)↙
'____////////////////////////////////////'];
```

Records the new block into the new *txt* file.

```
% Write cell A into txt
ID=['block' num2str(simCode) '.txt'];
fid = fopen(ID, 'w');
for i = 1:numel(A)
    if A{i+1} == -1
        fprintf(fid,'%s', A{i});
        break
    else
        fprintf(fid,'%s\n', A{i});
    end
end
```

Saves the *all.txt* file with the compilation of all of the created blocks.

```
d=dir('blockFlap1_*.txt');  % directory of suitable wildcard to find the desired files
fidOut=fopen('all.txt','w');  % and open an output file
for i=1:length(d)
  fid=fopen(d(i).name,'r');                   % open each file in turn
  fwrite(fidOut,fread(fid,'*char'),'*char')  % read remainder as char* image and echo↙
back out
  fclose(fid)                                 % done with that one ...
end
fclose(fidOut)                                % and close the output
```

End of cycles

```
end
end
```